

WETI c/o Fachhochschule Flensburg

Postal Address:

Kanzleistraße
24943 Flensburg, Germany

91-93

Visitors:

Nordstraße 2
24937 Flensburg, Germany

E-mail: arne.gloe@fh-flensburg.de

Simulation Model Design and Validation of a Gearless Wind Turbine

For Fast Power Control to Enhance Congestion Management

Final Project Report

Arne Gloe

Clemens Jauch

Table of Symbols and Abbreviations	4
List of figures	7
Abstract	11
Zusammenfassung	12
Acknowledgement	16
Introduction	16
Measurement Campaign	18
Wind Measurement	19
Description Measurement System	19
Assessment of Wind Measurement System	21
Measurement System in E30 Wind Turbine	22
Description Overall Measurement System	22
Communication infrastructure	26
CAN bus	27
Measurement System for Electrical Quantities	31
Measurement System for Mechanical Quantities	37
Longitudinal and Lateral Acceleration Measurement in Nacelle	37
Measurement System for Assessing the Blade Dynamics	40
Rotational Speed Measurement	43
Torque Measurement on Shaft	63
Pitch Angle Measurement	66
Development of the Simulation Model	82
Wind Model	82
Wind Turbine Model	89
Aerodynamics of the Rotor	90

Model of the Mechanical Structure of the Rotor and of the Drive Train.....	95
Imbalance Model.....	97
Model of the Tower.....	99
Model of the Generator-Converter-Unit.....	101
Model of the Speed Controller with Actuator	101
Control strategy.....	107
Model of the Grid.....	113
Design of Controller for Enhanced Congestion Management.....	117
Controller Design.....	117
Simulation Results	119
References	123
Appendix	124
Appendix A	124
Appendix B	148

Table of Symbols and Abbreviations

Symbol	Description	Unit
ADC	Analogue-digital-converter	
C_P	aerodynamic power coefficient	-
C_T	aerodynamic thrust coefficient	-
damp_Blades	Damping coefficient of the blades	p.u.
damp_Shaft	Damping coefficient of the shaft	p.u.
E30	Enercon E30 wind turbine	
f_{gen}	Frequency of the generator voltage	Hz
f_{rotation}	Rotational speed of the rotor	Hz
f_{sensor}	Measuring frequency of a sensor	Hz
$f_{\text{zebra stripes}}$	Frequency of the zebra stripes for the RPM measurement	Hz
G	shear modulus	Pa
I_T	torsion constant	m^4
I_r	Rated current transformer	A
J	Mass moment of inertia	$\text{kg} \cdot \text{m}^2$
J_{blades}	Mass moment of inertia of the blades	p.u.
$J_{\text{generator}}$	Mass moment of inertia of the generator	p.u.
J_{hub}	Mass moment of inertia of the hub	p.u.
k_{Blades}	Spring coefficient of the blades	p.u.
K_I	Gain factor of the integral part of the speed controller	
K_P	Gain factor of the proportional part of the speed controller	
k_{Shaft}	Spring coefficient of the main shaft	p.u.
l	length of the shaft	m
Met mast	Metrological mast	
p	pole pairs	-

P_{scl}	Short circuit power losses transformer	kW
R_{cable}	Ohmic resistance of the cable	Ohm
R_{tr}	Ohmic resistance of the transformer	Ohm
SUP	Step-up-converter	
T	Torque	Nm
Tau	Time constant of Eisman controller	s
Tau_max	Maximum time constant of Eisman controller	s
Tau_min	Minimum time constant of Eisman controller	s
TI	Turbulence intensity	-
UAS	University of Applied Science	
US	Ultra-sonic	
$\bar{v}_{wind,10min}$	Mean wind speed in 10-min interval	m/s
V_r	Rated voltage transformer	V
V_R	Voltage drop across transformer resistance	V
V_X	Voltage drop across transformer reactance	V
WETI	Wind Energy Technology Institute	
X_{cable}	Reactance of the cable	Ohm
X_{tr}	Reactance of the transformer	Ohm
z_0	Roughness length	m
Z_{cable}	Impedance of the cable	Ohm
Z_{tr}	Impedance of the transformer	Ohm
α	Angle of the voltage at the terminals to the grid voltage	deg
$\epsilon_{RPM,max}$	maximum error of RPM measurement	RPM
θ	Pitch angle	deg
Θ_t	twist angle of the shaft	rad
λ	Tip speed ratio	-

$\sigma_{v_wind, 10min}$	Standard deviation of wind speed in 10 min interval	m/s
φ_{Rotor}	Rotor position	rad
ω	rotational speed	rad/s
ω_blades	rotational speed of the blades in the simulation	p.u.
ω_gen	rotational speed of the generator in the simulation	p.u.
ω_hub	rotational speed of the hub in the simulation	p.u.

List of figures

Figure 1 Enercon E30 and met mast on Flensburg campus.	17
Figure 2 Schematic view of the installed measurement system.	19
Figure 3: Ultra-sonic anemometer on top of met mast	20
Figure 4: Nacelle anemometer	20
Figure 5: Ultra-sonic anemometer with red North marking at 35 m	21
Figure 6: Histogram of the difference in wind direction measurement between two ultra-sonic anemometers	22
Figure 7: Location of the measurement computer Dewetron 2010 in the wind turbine	23
Figure 8: Overview of the measurement system installed during the project	24
Figure 9: CAN Bus settings in Dewesoft	25
Figure 10: Screenshot of typical view of online measurements on Dewetron	26
Figure 11: Overview of the communication infrastructure including data transfer and time synchronisation	27
Figure 12: Overview of the CAN bus structure and participants	28
Figure 13: Switch cabinet in the nacelle with analogue to CAN bus converter in top-left corner	30
Figure 14: Overview of measurement locations for electrical quantities in the wind turbine	31
Figure 15 Measurement of generator voltage (left) and generator current (right) in the tower bottom	32
Figure 16: Instantaneous values of generator voltage and current of one phase for full load operation (top) and part load operation (bottom)	33
Figure 17: RMS values of generator voltage vs rotational speed (top) and voltage in the dc link vs rotational speed (bottom)	34
Figure 18: Measurement of DC link voltage (left) and DC link current (right) in the tower bottom	34
Figure 19: Instantaneous values of DC link voltage and current for full load operation (top) and part load operation (bottom)	35
Figure 20: Measurement of grid voltage (left) and grid current (right) in the tower bottom	36
Figure 21: Instantaneous values of grid voltage and current of one phase for full load operation (top) and part load operation (bottom)	36
Figure 22: Installed acceleration sensor view from the left side (left) and upper side (right)	37
Figure 23: Plot of longitudinal and lateral acceleration measurements of the nacelle	38
Figure 24: Plot of longitudinal and lateral acceleration measurements of the nacelle with a critical rotational speed	39
Figure 25: Single frame extracted from the video during the validation of the acceleration sensor	40
Figure 26: Single frame extracted from the video for the assessment of the blade dynamics	41
Figure 27: Distance laser sensor for the assessment of the blade dynamics	42
Figure 28: Measured distance between tower and blade and corresponding yaw position	42
Figure 29: Extract of Figure 28 measured distance between tower and one blade (left), and enlarged (right).	43
Figure 30: Terminology of the rotational speed measurement setup	46
Figure 31: Overview of contrast sensor and angle indicator at the rear end of the drive train shaft	48
Figure 32: Detailed view of contrast sensor and angle indicator	49
Figure 33: Overview of measurement system for measuring the rotational speed	50
Figure 34: Rotational speed measurements for eleven revolutions with indicated butt joints	52
Figure 35: Extract of Figure 34 Rotational speed measurement for roughly half a revolution	53
Figure 36: Extract of Figure 35 Example of the allocation of rotational speed measurements to zebra stripes	54

Figure 37: Histogram of the angle of zebra stripe 4 and 5 created from rotational speed measurements in August 2014 with 389,825 revolutions (bin width 0.005); measured rotational speed of the stripe is normalised with the average rotational speed of the revolution during which it was recorded.	55
Figure 38: Angle between consecutive zebra stripes deducted from rotational speed measurements in August 2014 with 389,825 revolutions; Note: value for butt joint (1.129 deg) is above the scale of the y-axis	56
Figure 39: Relative speed of the zebra stripes for August 2014 and December 2014 (top) and the difference of the relative speed between the two months (bottom)	57
Figure 40: Influence of extreme soiling on the rotational speed measurement. Time series of rotational speed measurements before (top) and after (bottom) cleaning the zebra code	58
Figure 41: Comparison of rotational speed measurements before and after the correction of the deterministic error	59
Figure 42: Effect of limited frequency of contrast sensor on the detection of the black stripe	59
Figure 43: Output of the contrast sensor during jitter analysis; output signal vs time (left) and overlay of the three output steps (right)	61
Figure 44: Maximum absolute error of the drive train speed measurement for all stochastic errors	62
Figure 45: Rotational speed and calculated rotor position for several revolutions	63
Figure 46: Torque measurement - strain gauge and telemetry	64
Figure 47: Time series of torque measurement in part load operation	65
Figure 48: Comparison of the measured electrical power of the generator and the mechanical power of the drive train calculated from the measurements of torque and rotational speed	66
Figure 49: Sketch of the principal setup of the pitch angle measurement system.	68
Figure 50: The distance measured by the distance laser sensor is a function of the pitch angle.	69
Figure 51: The angle indicator. Left: 3-D plot. Right: Archimedean spiral	69
Figure 52: Pitch angle sensor: laser sensor for distance measurement and angle indicator	71
Figure 53: Pitch angle sensor: detailed view of laser sensor for distance measurement	71
Figure 54: Measured time series of distance signal of an angle indicator passing the laser sensor	72
Figure 55: Flow chart of the data processing which derives a pitch angle value from the measured distance values.	73
Figure 56: Left: distance measurement and calculated pitch angle. Right: zoom of disturbed distance measurement at angle indicator.	74
Figure 57: Time series of signals during the pitch angle calibration process.	75
Figure 58: Variations of the measured distance to the angle indicator for a constant pitch angle.	75
Figure 59: Relation between averaged measured distances to the angle indicator and pitch angles.	76
Figure 60: Stationary pitch angle measured by the pitch angle sensor. Variations in the signal are the sum of the measurement error and the pitch positioning error.	77
Figure 61: Distance signal and calculated pitch angle of one blade.	78
Figure 62: Measured pitch angle of one blade and the measured rotational speed of the rotor over a period of three days.	79
Figure 63: Extract of Figure 62. Measured pitch angle of one blade and the measured rotational speed of the rotor.	80
Figure 64: Histogram of pitch angle measurements for 17 May 2015, 12:00 to 18 May 2015, 12:00	81
Figure 65: Block diagram of the wind model	82

Figure 66: Weibull distribution of wind speed measurements (10-min averages)	83
Figure 67: Comparison of the turbulence intensity of the three wind measurements	84
Figure 68: Turbulence intensity for easterly wind direction sectors for the measurement at 50 m	85
Figure 69: Spectral analysis of 10-min averaged values of the wind measurement at 50 m	86
Figure 70: Spectral analysis of 10 Hz the wind measurement data at 50 m, 35 m, and 25 m	87
Figure 71: Comparison of the spectral analysis of simulated wind signal and the measured wind signal	88
Figure 72: Block diagram of the simulation model	89
Figure 73: Block diagram of aerodynamic model	90
Figure 74: Comparison of measured and calculated C_p values for a pitch angle of one degree	92
Figure 75: Comparison of measured and calculated C_p values for different pitch angles	92
Figure 76: Surface plot of the power coefficient as a function of tip speed ratio and pitch	93
Figure 77: Plot of longitudinal acceleration and drive train speed during an emergency stop	94
Figure 78: Comparison of measured values for c_T with data for the NREL 5 MW reference turbine	95
Figure 79: Three-mass representation of the drive train	96
Figure 80: Frequency spectrum of measured power and of measured rotational speed	97
Figure 81: Block diagram of the drive train model	97
Figure 82: Tower excitation by mass imbalance	98
Figure 83: Imbalance model	98
Figure 84: Comparison of measured and simulated lateral acceleration of the tower	99
Figure 85: Model of the tower	100
Figure 86: Block diagram of the model of the generator-converter-unit	101
Figure 87: Block diagram of the power demand rate limiter as part of the speed controller	102
Figure 88: Measured grid power during a decrease (left) and an increase (right) of the power set point	102
Figure 89: Difference in measured grid power vs. elapsed time for different steps in the power set point	103
Figure 90: Block diagram of the speed controller	104
Figure 91: Determination of controller parameter: proportional term	104
Figure 92: Determination of controller parameter: integral term	105
Figure 93: Block diagram of the pitch drive model	106
Figure 94: Pitch angle measurement during an emergency stop for all blades (pitch angles above 59 deg have not been measured during this event)	107
Figure 95: Grid-power-vs-speed-characteristic created from instantaneous values	108
Figure 96: Measured values of grid power (top) and rotational speed (bottom) during reduced power set point operation	109
Figure 97: Comparison of fitted power-vs-speed-characteristic for reduced power set points with measured values	110
Figure 98: Comparison of power-vs-speed-curves for grid power (normal operation and reduced power set point) and generator power.	111
Figure 99: Continuous optical pitch angle measurement with a camera on the spinner. Left: camera on spinner. Right: view as seen by the camera	112
Figure 100: Pitch angle and pitch rate versus rotational speed during start-up of the E30.	112
Figure 101: Pitch angle and pitch rate versus rotational speed during a soft braking procedure of the E30.	113
Figure 102: Equivalent circle diagram of the grid.	114

<i>Figure 103: Data sheet of the power transformer of the E30.</i>	115
<i>Figure 104: Campbell diagram of the E30</i>	117
<i>Figure 105: Block diagram of controller to modify the power limitation of the grid operator</i>	118
<i>Figure 106: Power demand signal from congestion management; transformer station Strübbel Oct 2015 [17].</i>	118
<i>Figure 107: Power demand signal for enhanced congestion management.</i>	119
<i>Figure 108: Wind speed and pitch angle during simulation with disabled Eisman controller.</i>	120
<i>Figure 109: Power signals and tower head acceleration during simulation with disabled Eisman controller.</i>	120
<i>Figure 110: Power signals and tower head acceleration during simulation with enabled Eisman controller.</i>	121
<i>Figure 111: Extract of Figure 110 Detailed view of power signals during simulation with enabled Eisman controller.</i>	122

Abstract

This project aimed to model the dynamic behaviour of an Enercon E30 wind turbine in order to design a controller which enables a faster control of the power of the turbine during congestion management. Congestion management has been in the past and will be in the foreseeable future a major cause for energy yield losses for wind turbines in Schleswig-Holstein. The University of Applied Science Flensburg owns an E30 on its campus in Flensburg. This wind turbine is equipped with a comprehensive measurement system during the project. Furthermore, a metrological mast close to the turbine is also refitted with a modern measurement system. Data acquired with these measurement systems is used to find the parameters for the model of the wind turbine and to create realistic time series of the wind. The model is created in a Matlab/Simulink environment which allows a simulation in the time domain. An actual congestion management signal is compressed in time and used as an input to the model. The simulations show that the turbine generally deals well even with very fast changes. This is due to an existing limitation of the rate at which the power demand signal can be changed. However, when enhanced congestion management signals are simulated the tower head accelerations exceed a critical threshold.

A controller for the Eisman signal is proposed. The controller modifies the power demand signal of the grid operator with a PT1 element before it enters the control system of the turbine. The time constant of the PT1 element varies depending on the state of the turbine. Hence, critical tower head accelerations can be avoided, which are caused by fast changing power out. The controller is tested in simulations with an enhanced congestion management signal and for several wind speed signals. The oscillations of the tower head have been dampened significantly. The simulations show promising results. However, the controller must be tested under other circumstances in the future to assess its performance. Furthermore, the effects of enhanced congestion management on the loads of the turbine were not part of this project. These may outweigh any improvement in the energy yield and must therefore be researched as well.

Zusammenfassung

Ziel des Forschungsprojektes "*Untersuchung des dynamischen Verhaltens getriebeloser WEA im Hinblick auf Leistungsbereitstellung im Netz im Minuten- und Sekundenbereich*" ist die Verbesserung des Einspeisemanagements für Windenergieanlagen (WEA). Die Netzbetreiber dürfen Windenergieanlagen abschalten, wenn ansonsten ihr Netz überlastet werden würde. Einspeisemanagement führt in Schleswig-Holstein, besonders an der Westküste, durch die Abschaltung von Windenergieanlagen zu erheblichen Ertragsverlusten, die einen wirtschaftlichen Schaden sowohl für die Betreiber als auch für die Volkswirtschaft führen. Da erwartet wird, dass sich die Situation auch in den nächsten Jahren nicht entspannt, sollte das Einspeisemanagement verbessert werden. Insbesondere wird heute das Einspeisemanagement Signal nur selten geändert – lediglich alle 10 bis 15 Minuten. Schnellere Änderungen können jedoch zu einer Belastung von Windenergieanlagen führen. Daher ist der Ansatz dieses Projektes die Grenzen der Belastbarkeit einer getriebelosen WEA zu untersuchen. Da die Fachhochschule Flensburg auf dem Campus in Flensburg über eine getriebelose Windenergieanlage vom Typ Enercon E30 (E30) und in unmittelbarer Nähe zudem über einen Windmessmast verfügt, soll dieser Anlagentyp beispielhaft untersucht werden. Auch wenn die WEA schon fast 20 Jahre alt ist, verwendet sie schon ein Steuerungssystem das mit modernen Anlagen vergleichbar ist (variable speed, pitch-to-feather).

WEA regeln ihre Drehzahl nach dem gerade herrschenden Windverhältnissen. Das Einspeisemanagement wird durch die Obergrenze für die eingespeiste Leistung einer WEA oder eines Windparks umgesetzt. Diese Obergrenze wird heute nur in sehr großen Zeitscheiben, d.h. alle 10 min bis 15 min geändert. Daher hat diese Regelung kaum Einfluss auf die Dynamik der WEA. Allerdings wird auch nur für einen sehr kurzen Zeitraum der tatsächliche Zustand des Netzes beachtet. Für die meiste Zeit ist man auf eine Prognose des Zustandes und die Auslastung der einzelnen Netzkomponenten angewiesen. Um die Zeitscheiben für das Einspeisemanagement verkleinern zu können, muss der Einfluss des Einspeisemanagements auf die Dynamik der WEA untersucht werden.

Eine moderne WEA besteht zu einem großen Teil aus leichten, schlanken und langen Komponenten. Diese sind anfällig für Schwingungen. Da die einzelnen Komponenten zudem über nicht lineare Zusammenhänge miteinander gekoppelt sind, muss die Dynamik einer WEA mittels eines Simulationsmodells untersucht werden. Für dieses Projekt wurde ein solches Simulationsmodell in Matlab und Simulink erstellt. Dies ermöglicht eine Simulation im Zeitbereich. Die einzelnen Komponenten der WEA werden durch Subsysteme im Simulationsmodell repräsentiert. Für die Modellierung dieser Subsysteme wurden überwiegend Standardmodelle verwendet. Um diese an die untersuchte WEA anzupassen, müssen Parameter ermittelt werden. Da zu Beginn des Projektes nur wenig Informationen zu der Anlage vorlagen

und der Anlagenhersteller keine Informationen heraus gibt, wird für die Ermittlung der notwendigen Parameter wird zudem eine umfangreiche Messkampagne an der Anlage auf dem Campus Flensburg durchgeführt.

Diese Messkampagne wird in Zusammenarbeit DNV-GL Zweigstelle Kaiser-Wilhelm-Koog durchgeführt. Der DNV-GL unterstützte das Wind Energy Technology Institute (WETI) dabei mit Material, Arbeitsstunden und Know-How und hat somit maßgeblich zum Erfolg des Projektes beigetragen. Die wichtigsten Größen, die den Zustand einer getriebelosen WEA beschreiben, können gemessen werden:

- Pitchwinkel
- Drehzahl
- Drehmoment
- Turmkopfbeschleunigung
- Blattdynamik
- Windmessung auf dem Gondeldach (aus der Kundenschnittstelle der Anlage abgegriffen)
- Elektrische Größen des Generator, im Zwischenkreis und auf der Netzseite

Die mechanischen Größen werden in der Gondel der WEA gemessen und über einen CAN Bus zum Messrechner im Turmfuss übertragen. Dort sind neben einem Dewetron 2010 als Messrechner noch die unterbrechungsfreie Spannungsversorgung des Messsystems sowie die Sensoren zur Erfassung der elektrischen Größen installiert.

Zudem wird der Windmessmast mit einem modernen Messsystem mit Ultraschallanemometern ausgestattet, die in 3 Höhen die Messung von Windgeschwindigkeit, Windrichtung und Temperatur erlauben. Zudem werden Messgeber für die Erfassung von Temperatur, Luftfeuchte und Luftdruck sowie ein neuer Datenlogger installiert. Der Großteil des Messequipments verbleibt nach Ende des Projektes in der Anlage und am Windmessmast. Auf Basis dieses Equipments werden verschiedene Laborübungen entwickelt, in denen unter Verwendung von Livedaten den Studenten die Regelung moderner Windenergieanlagen erläutert wird. Diese Übungen tragen erheblich zur Verbesserung der Lehre bei der Ausbildung von Ingenieuren an der Fachhochschule Flensburg bei. Die Fachhochschule Flensburg investiert zudem in den Erhalt und den Ausbau des Messsystems.

Die Messkampagne kann trotz einiger Verzögerungen beim Aufbau und Problemen bei der Zuverlässigkeit einzelner Komponenten erfolgreich abgeschlossen werden. Insbesondere kann die Entwicklung eines nachträglich eingebauten Pitchwinkelsensors sowie einer hochauflösenden Drehzahlmessung als Erfolg angesehen werden. Zudem können neue Erkenntnisse zu den an der Anlage herrschenden Windverhältnissen gewonnen werden. Teile

der in der Messkampagne gewonnen Daten sollen auf der Homepage des WETI zum Download angeboten und so der Allgemeinheit zur Verfügung gestellt werden.

Eine Eigenfrequenzanalyse der Anlage ist ein besonders wichtiger Bestandteil der Messdatenauswertung. Dadurch kann unter anderem die Ursache für häufig an der WEA auftretende Querschwingungen identifiziert werden: Im Teillastbetrieb treten Drehzahlen auf, die sich mit der ersten Eigenfrequenz des Turmes überschneiden. So können Kräfte aus unvermeidbar auftretende Massenunwuchten im Rotor bei entsprechenden Windverhältnissen den Turm im Resonanzspektrum anregen, so dass sich die Querschwingungen im Laufe der Zeit aufschaukeln. Bei anderen Windenergieanlagen wird dies durch ein schnelles Durchfahren kritischer Drehzahlbereiche durch die Steuerung der Anlage verhindert.

Wie bereits oben beschrieben werden überwiegend Standardmodelle für die Simulation verwendet. Daher ist die wesentliche Aufgabe im Projekt die Parametrisierung der Modelle. Im Einzelnen wurden die verschiedenen Subsysteme wie folgt abgebildet:

- Windmodell: Abwandlung eines Modells für die schnelle Simulation von Windverhältnissen im Windpark nach Jauch. Das Modell nutzt Messdaten vom Windmessmast als Eingangsgröße. Das Windmodell simuliert den Wind über der Rotorfläche über einen zeitlich veränderlichen Vektor.
- Aerodynamik: Abbildung der Aerodynamik über c_T und c_P Tabellen in Abhängigkeit von der Schnelllaufzahl und des Pitchwinkels. Die Änderung der aerodynamischen Kräfte in Abhängigkeit der Position der Rotorblätter wird über den zeitlich veränderlichen Windeingangsvektor berücksichtigt.
- Mechanischer Triebstrang: Abbildung als 3-Massen-Modell, die über Drehfedern mit entsprechenden Federkonstanten und Dämpfungskonstanten miteinander verbunden sind. Der mechanische Triebstrang wurde an zwei Stellen aufgetrennt, so dass die Blätter, die Kombination aus Nabe und Bremsscheibe sowie der Läufer des Generators jeweils eine Masse bilden.
- Unwuchtmodell: Abbildung der Massenunwucht über eine Punktmasse, die mit der Rotordrehzahl in einem konstanten Abstand um die Drehachse rotiert.
- Turmmodell: Abbildung als gedämpfter Einmassenschwinger, mit einer Punktmasse und einer festen Einspannung im Fundament. Das Modell kann die erste Eigenfrequenz des Turms abbilden.
- Generator-Umrichter-Einheit: Abbildung über ein generisches Modell, das häufig für Netzsimulationen genutzt wird und die Generator-Umrichter-Einheit über ihr Verhalten abbildet.
- Drehzahlregler mit Aktuator: Abbildung des Drehzahlreglers als PI-Regler und des Stellgliedes über ein PT1 Element mit einer Begrenzung der Verfahr Geschwindigkeit.

Zudem wird hier berücksichtigt, dass die E30 ihren Leistungssollwert nur begrenzt schnell ändert.

- Regelungsstrategie: Abbildung über verschiedene Drehzahl-Leistungs-Charakteristiken für den ungestörten Betrieb und den leistungsreduzierten Betrieb.
- Netz: Abbildung des Netzes als unendlich steife Spannungsquelle, die über die Impedanzen von Kabel und Transformator mit der Anlage verbunden ist.

Für alle Modelle können die Parameter mit ausreichender Genauigkeit ermittelt werden, so dass die Anlage in Simulationen mit aus Messwerten generierten Windverhältnissen ein realistisches Verhalten zeigt.

Bei der Auswertung der Messergebnisse sowie von ersten Simulationen wurde die Turmkopfbeschleunigung als kritische Größe für schnelle Leistungsänderungen identifiziert. Insbesondere wird der Turmkopf zu Schwingungen in Längsrichtung angeregt, wenn das Einspeisemanagement Signal zu schnell geändert wird. Es besteht jedoch auch ohne die Implementierung eines zusätzlichen Reglers noch ein erhebliches Potential zur Verkürzung der Zeitscheiben des Einspeisemanagements. Dies wird ermöglicht durch die in der Anlagensteuerung hinterlegte Begrenzung der Änderungsgeschwindigkeit des Leistungssollwertes. Sehr schnellen Änderungen (Zeitscheiben < 5 s) können jedoch zu kritischen Schwingungen des Turmkopfes führen. Daher wurde ein Regler vorgeschlagen, der das Einspeisemanagement Signal dämpft, wenn die Turmkopfbeschleunigungen zu groß sind. Wenn die Anlage stabil läuft wird das Signal dagegen unverändert durchgelassen. Dies wird über ein PT1-Glied mit veränderlicher Zeitkonstante realisiert, die in Abhängigkeit der Höhe der Turmkopfbeschleunigung eingestellt wird. In ersten Simulationen zeigt der Regler die gewünschten Eigenschaften. Um eine fundierte Beurteilung der Eignung des vorgeschlagen Reglers abgeben zu können, sind jedoch weitere Simulationen notwendig. Zudem ist anzumerken, dass die Nachteile aus einer Erhöhung der Lasten die wirtschaftlichen Vorteile einer zusätzlichen Energieproduktion unter Umständen zu Nichte machen können. Eine Beurteilung der Auswirkung der Regelung auf die Lasten war nicht Teil des Projektes.

Insgesamt kann das Projekt erfolgreich abgeschlossen werden. Die Projektziele werden erreicht und es ist zudem gelungen für die Fachhochschule Flensburg einen dauerhaften Mehrwert durch die erwähnten Laborübungen zu schaffen. Die Autoren danken der Gesellschaft für Energie und Klimaschutz Schleswig-Holstein GmbH (EKSH) für die finanzielle Unterstützung.

Aus dem Projekt sind bis zum heutigen Stand eine wissenschaftliche und mehrere nicht-wissenschaftliche Veröffentlichungen hervor gegangen. Zudem wurde bei mehreren Veranstaltungen über das Projekt berichtet. Die interessierte Öffentlichkeit wurde regelmäßig im Rahmen von Ringvorlesungen über aktuelle Themen aus dem Projekt informiert.

Acknowledgement

This report summarises the results of the research project "*Untersuchung des dynamischen Verhaltens getriebeloser WEA im Hinblick auf Leistungsbereitstellung im Netz im Minuten- und Sekundenbereich*". This project was carried out by the Wind Energy Technology Institute at Flensburg University of Applied Sciences. The authors acknowledge the financial support to the project by the Gesellschaft für Energie und Klimaschutz Schleswig-Holstein GmbH (EKSH), project number 8/12-6.

A major contributor to the success of the project was the Kaiser-Wilhelm-Koog branch of DNV GL AS, who was the formal project partner. Their support with measurement equipment, work force and know-how was essential to the successful installation of the whole measurement system and during the measurement campaign.

The authors also acknowledge the financial support by Flensburg University of Applied Science, which enabled the installation of a more comprehensive measurement system than intended at the start of the project.

DMT GmbH & Co KG in Essen provided an acceleration sensor to the measurement system.

Furthermore the authors acknowledge the contribution of the following persons to this project. Norbert Nussel, Stefan Vetter, Achim Struve, Andrea Haberl, Torben Krakow, Tobias Krause, Lasse Roeßler, David Llano, Sebastian Hippel, Henning Thiesen, Fred Kankelfitz, Sören Behnsen, Leif Poschmann, Patrick Schönherr, Sören Petersen, Mitja Klatt, Philip Janke, Klaus Heiner Techow, Christian Peters, Carl-Wilhelm Nehl. They worked at the Wind Energy Technology Institute as employees (in part time positions), as student assistants or as students who composed their Master theses or their semester assignments. With their work they contributed to the successful completion of the project.

Introduction

Flensburg University of Applied Sciences (UAS Flensburg) owns a wind turbine, which is available for research and teaching purposes, located on Flensburg campus. This wind turbine is an Enercon E30 (E30), which was erected in 1996. Despite its considerable age the E30 is still state of the art in terms of the overall control concept. Therefore, the principle behaviour of the E30 is comparable to modern wind turbines of the multi-megawatt class.

Furthermore, the UAS Flensburg owns a metrological mast (met mast) in 100 m distance from the wind turbine in main wind direction. Figure 1 shows the E30 and the met mast. This combination allows studying the behaviour of a wind turbine directly on the campus.



Figure 1 Enercon E30 and met mast on Flensburg campus.

This project aims to model the dynamic behaviour of the E30 in order to design a controller, which alternates the wind turbine power depending on the state of the electrical grid.

During times with a high production of wind and solar energy the electrical grid in Schleswig-Holstein is often working at its maximum capacity. To prevent grid failures due to overloading, the grid operators are allowed to curtail the power production of wind turbines - the so called congestion management. Congestion management has led to considerable losses of energy production in the past [2], and is expected to remain high in the coming years [3].

The curtailment of the wind turbine power production is done for a long time period (i.e. 10 minute periods) and in large steps (at least 30% of the installed capacity). While the curtailment is justified by the state of the grid, the actual state of the grid is only represented for very short times due to large time steps. Hence, the congestion management may be enhanced by shortening the time periods and reducing the step-size.

However, this approach may lead to critical operation points of the wind turbine as fast changes in the power output can cause oscillations of mechanical components of the wind turbine. This project sought to investigate the potential for improving the congestion management. In a first step a theoretical model of the wind turbine was developed. Its parameters were determined by an extensive measurement campaign, which was a major part of the project. Using the validated model critical time steps for the changes in power output of a gearless wind turbine were identified. Finally, a first draft for a wind turbine controller was developed which prevents critical oscillations induced by congestion management in the most vulnerable mechanical components of the turbine.

Measurement Campaign

An important part of the project is the installation of a comprehensive measurement system in the wind turbine and on the metrological mast on campus. The measurement system in the wind turbine is installed in a combined effort by the Wind Energy Technology Institute (WETI) and DNV-GL. The system is based on a Dewetron 2010 measurement system, which is used for data acquisition, data processing and data storage. A Wilmers NDL 485 research data logger is used for the measurement system at the met mast. Figure 2 shows an overview of the measurement system.

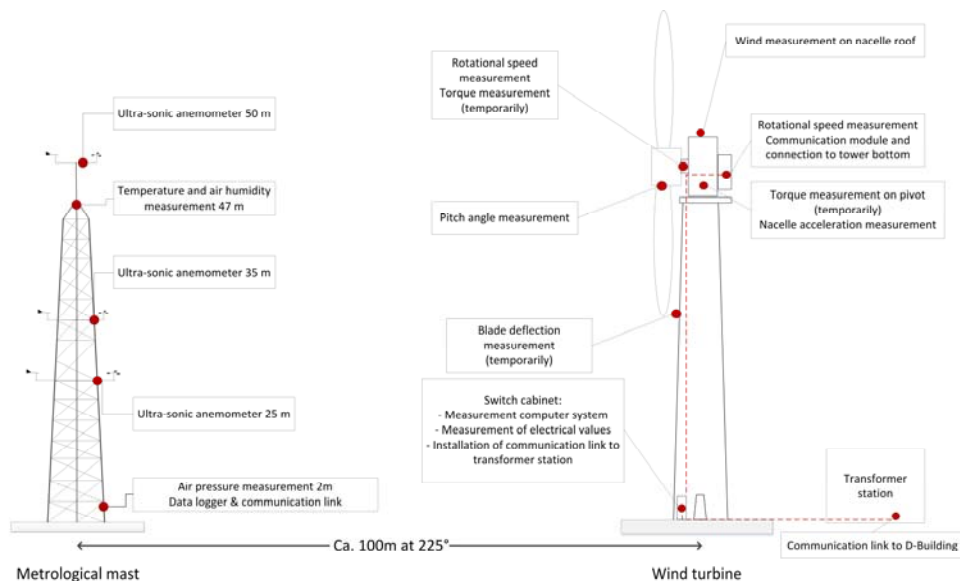


Figure 2 Schematic view of the installed measurement system.

Wind Measurement

Description Measurement System

As mentioned above the UAS Flensburg owns a metrological mast in the vicinity of the investigated wind turbine. At the beginning of the project the installed measurement system on the mast was outdated. Therefore, a new system with three ultra-sonic anemometers at different heights and sensors for the metrological data are installed (see Figure 2). 2 D ultra-sonic anemometers by Thies Clima are used. Its technical specifications are listed in a data sheet in Appendix A. The sensors are installed at 25 m, 35 m (lowest position of the blade tip), and 50 m (hub height, see Figure 3). The three wind speed measurements allow a representation of the vertical wind profile at the site. The Wilmers data logger is capable of acquiring all data with a measurement frequency of 10 Hz. This is a reasonable value to measure the relevant turbulences in the wind. The wind speed sensors are connected to the data logger via a RS 485 bus, which allows an easy installation of additional sensors in future projects. The sensors to measure the air temperature, the air humidity and the air pressure are connected directly to the data logger and are sending analogue signals.

Another wind speed measurement is located on top of the nacelle. The wind speed is measured by the E30 control system with a cup anemometer (see Figure 4). This signal can be implemented into the measurement systems via Enercon's customer interface. The

measurement frequency is limited to 1 Hz due to the measurement with a cup anemometer and the settings of the customer interface.



Figure 3: Ultra-sonic anemometer on top of met mast



Figure 4: Nacelle anemometer

Assessment of Wind Measurement System

For the wind direction measurements the deviation between the North marking on the sensor and true North has to be determined. The ultra-sonic (US) anemometers on 25 m and 35 m are installed on crossbeams of the met mast whose deviation to true North is known. The anemometers are aligned with these cross beams during installation. However, they cannot be aligned perfectly. The best alignment is achieved for the sensor at 35 m (see Figure 5). Hence, this sensor is chosen to calibrate the wind direction measurements for the other sensors. The sensor at 50 m is installed on the top bar of the met mast. The angle between the top bar and true North is unknown. As a first approach the North marking on the US anemometer is therefore estimated with binoculars with a built-in compass. Afterwards measured data are used to find the true angle as described below.



Figure 5: Ultra-sonic anemometer with red North marking at 35 m

In order to determine the angular displacement between the US anemometer at 35 m and the other sensors, the difference in wind direction measurements between the sensors are calculated. As turbulences also contain wind direction changes one would expect differences in wind direction measurement for the different sensors when comparing instantaneous values.

However, the differences in directions should roughly be normally distributed, with a central value of 0 deg difference. Any shift to the left or right are interpreted as deterministic errors due to badly chosen deviation between the North marking on the sensor and true North. Hence, these offsets have to be corrected in the measurement setup.

An evaluation of one month data is used to determine the offsets. Figure 6 shows the histogram for the comparison of wind direction measurements at 35 m and 50 m. The centre of the Gaussian distribution is shifted to the right due to an error in the estimation of the orientation of the top bar. The mean value of the offset is determined to be approximately 3 deg and can be accounted for in the measurement setup. Using the same methodology the offset settings of the US anemometer at 25 m is corrected by 1 deg.

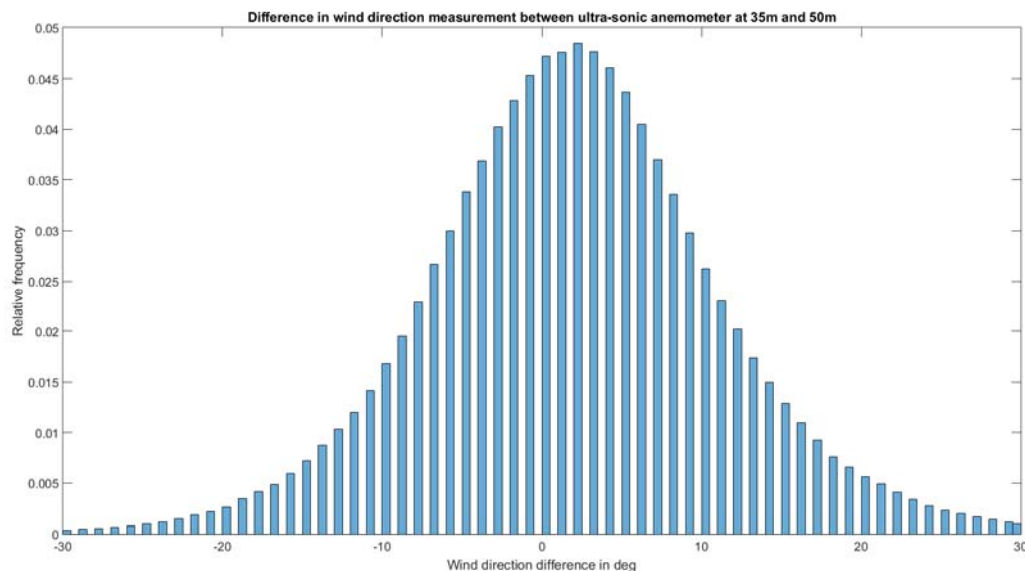


Figure 6: Histogram of the difference in wind direction measurement between two ultra-sonic anemometers

Measurement System in E30 Wind Turbine

Description Overall Measurement System

As stated above a Dewetron 2010 is used as measurement computer (see Appendix A for a data sheet). It is installed in the wind turbine in a Zarges box with a rudimental control of temperature and humidity (see Figure 7).



Figure 7: Location of the measurement computer Dewetron 2010 in the wind turbine

The Dewetron 2010 is capable of simultaneously acquiring data via CAN bus, RS 485, and an analogue-digital-board with seven high voltage input channels (up to 1400 V) and nine low voltage inputs (up to 50 V). All sensors in the wind turbine are connected to the Dewetron. Figure 8 shows an overview of all sensors and how they are connected with the Dewetron. It furthermore shows how the Dewetron is implemented into the UAS Flensburg network.

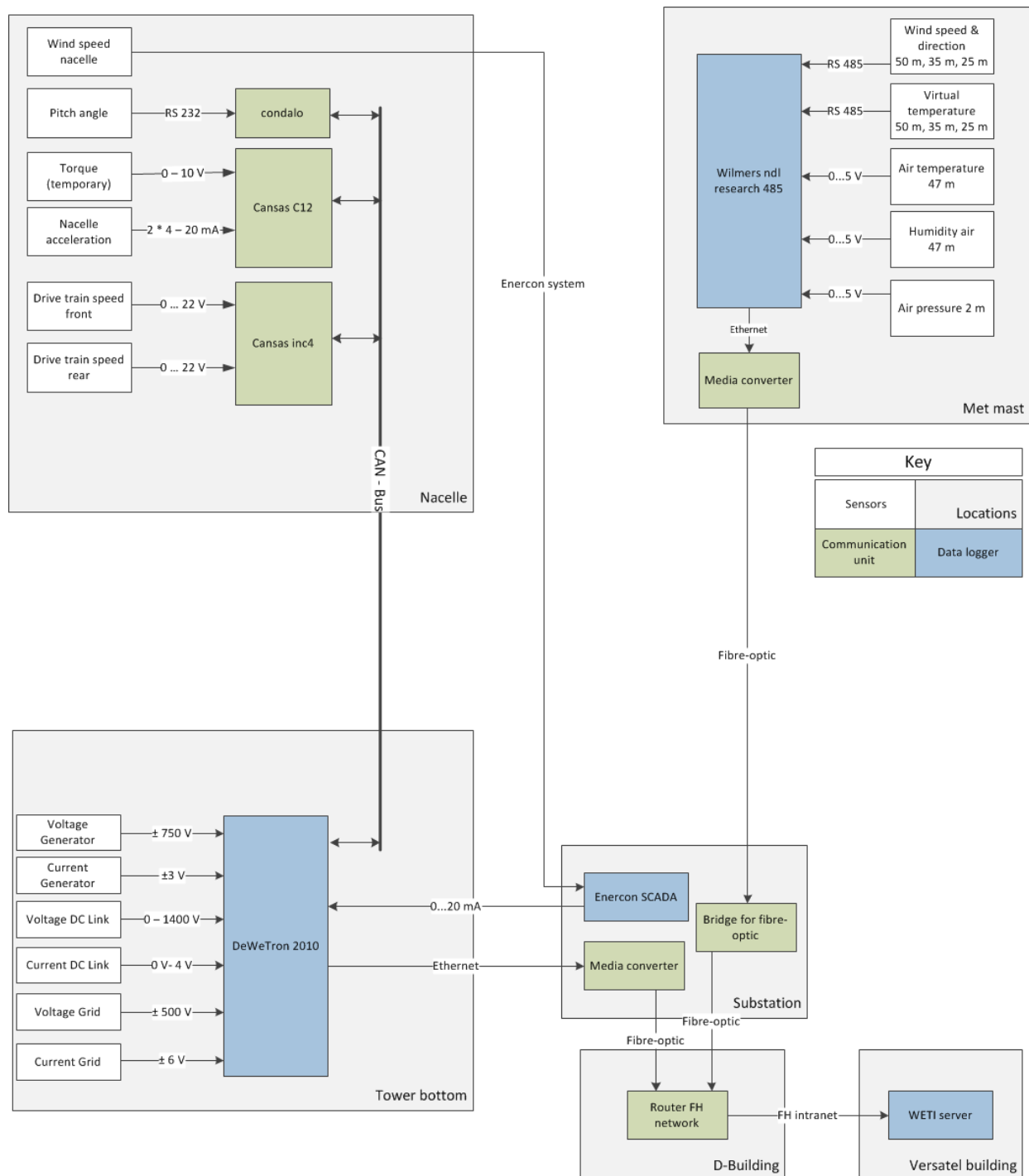


Figure 8: Overview of the measurement system installed during the project

Dewesoft 6.6.7 is running as measurement software on the Dewetron. In the setup interface all input channels (analogue and digital) can be configured. It also includes a wide range of data

processing options from basic mathematical operations to online Fourier transformations and multi-phase power computations. An example for CAN bus setting options is given in Figure 9.

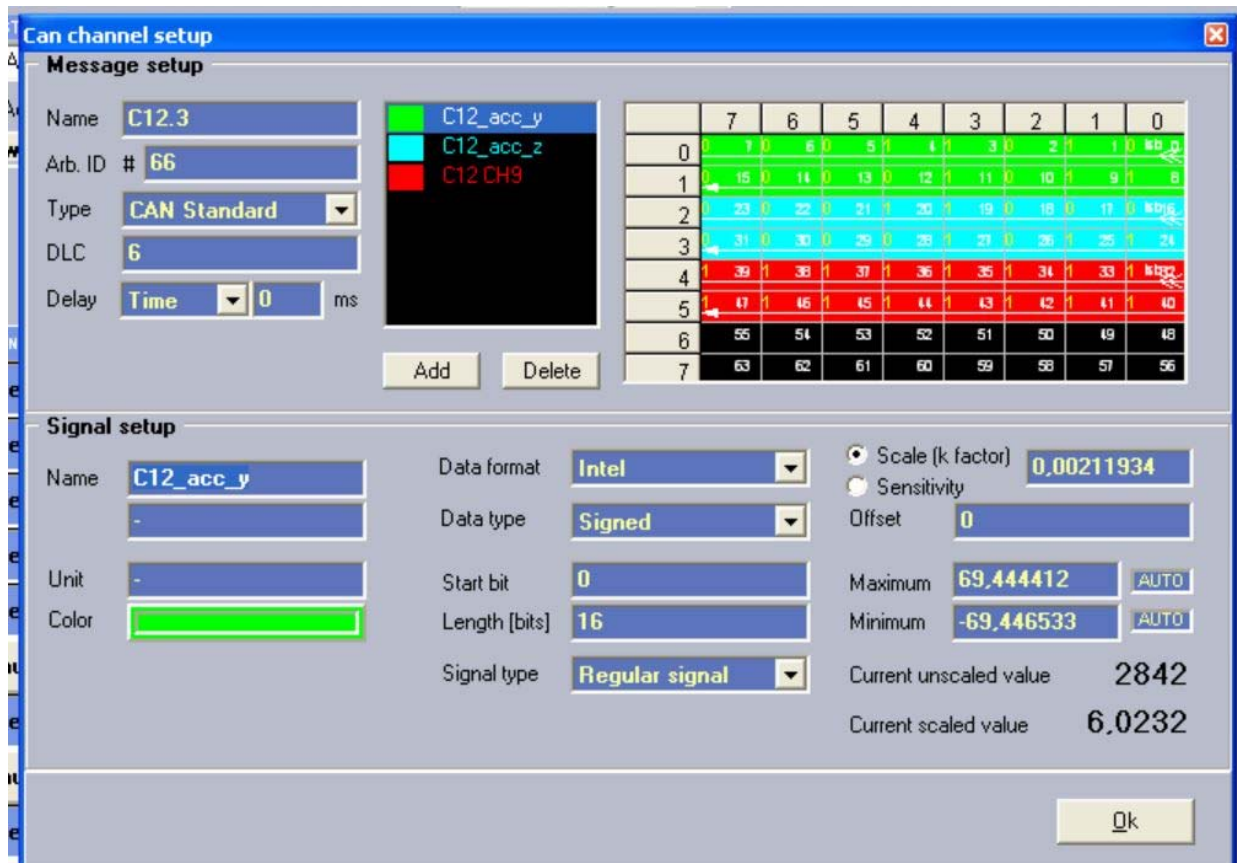


Figure 9: CAN Bus settings in Dewesoft

Furthermore, it allows graphical representations of online measurements in many ways (scopes, plot, digital meters, phasor diagrams, etc.). These features are used during laboratory exercises with students, which are based on the measurement system installed in this project. Figure 10 shows a typical screenshot of Dewesoft graphs during a laboratory exercise.

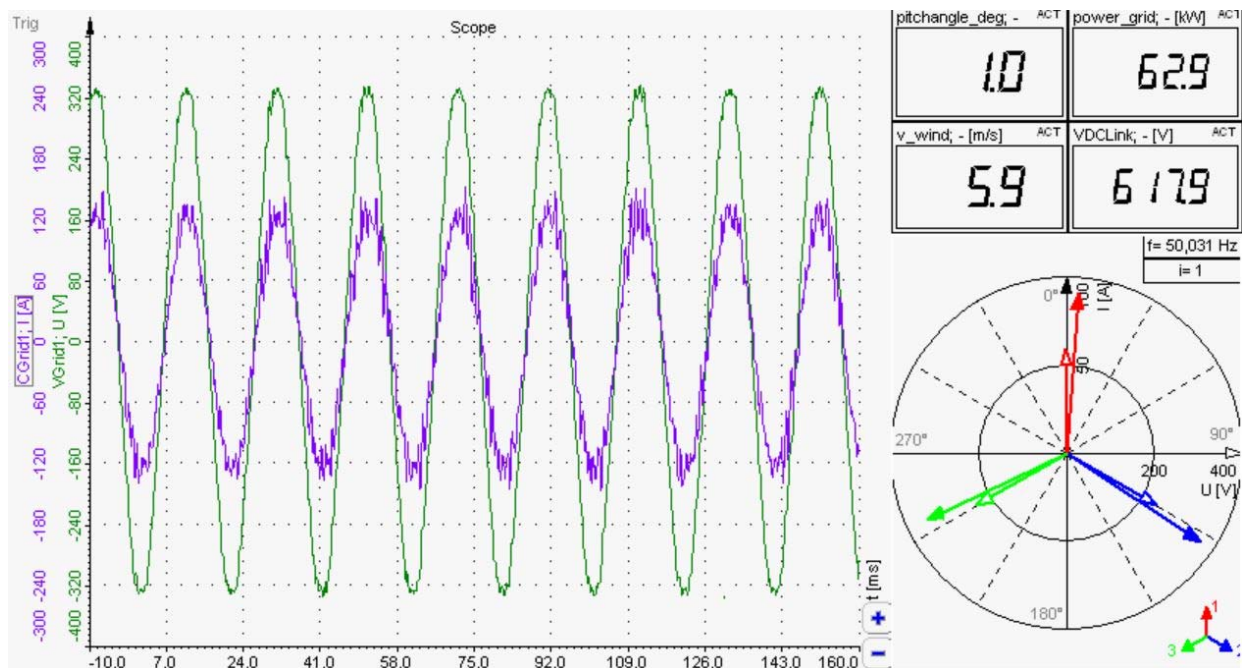


Figure 10: Screenshot of typical view of online measurements on Dewetron

The time stamps of the Dewetron 2010 and the Wilmers NDL 485 research are connected to a time server in the local network to ensure, that the time stamps of all measurements are synchronised.

Communication infrastructure

The measurement system is embedded in the communication infrastructure of the UAS Flensburg (see Figure 11). The met mast and the transformer station are connected to the main buildings of the UAS via fibre-optic cables. The wind turbine and the transformer station are connected via copper cables. This allows an Ethernet connection of all data loggers to the network on campus and in the Versatel building, where the data is stored on the WETI server.

When measuring related data with separate data loggers, the time stamps of the measurements on these data loggers have to be synchronised. This was ensured by synchronising the system time of all loggers with a NTP server. The provided time signal has a precision in the nanoseconds range, which is sufficient for the intended measuring frequencies.

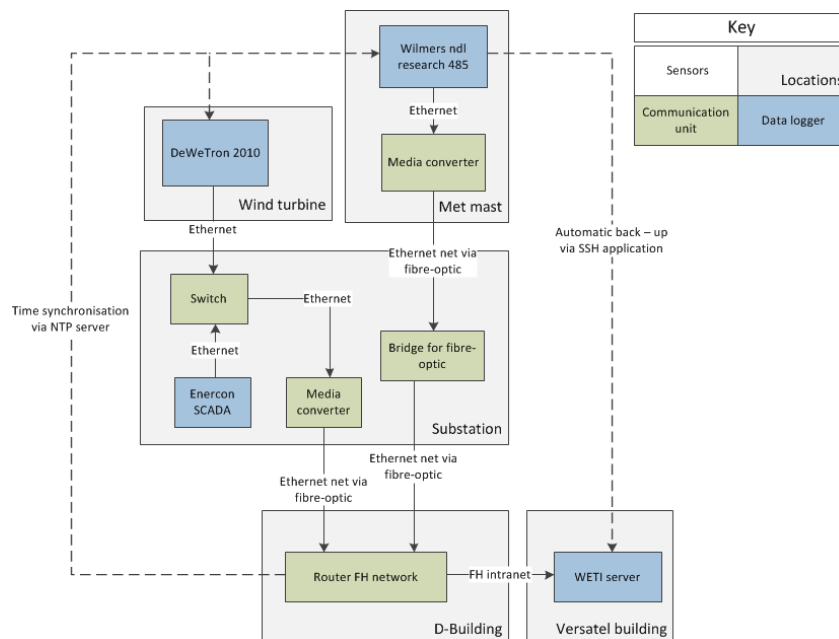


Figure 11: Overview of the communication infrastructure including data transfer and time synchronisation

Furthermore, the Ethernet connection allows accessing the data logger via remote desktop applications and web interfaces. These connections are used for changing setups and manually transferring data to the WETI server. Besides, the Wilmers data logger uses a SSH application for automated back-up of the measured data on the WETI server.

In case of unexpected system crashes the Dewetron 2010 can be restarted by a power strip, which can be controlled remotely via the Ethernet connection as well. The Wilmers data logger can be restarted via the web interface as long as it can be reached via the Ethernet connection.

CAN bus

As all mechanical quantities are measured in the nacelle of the wind turbine (see Figure 8), a communication system is needed to transfer the measured data to the data logger. For this purpose a CAN bus is installed in the turbine. It consists of four major participants as shown in Figure 12 (see Appendix A for data sheets). The Dewetron in the tower bottom is only receiving data. All participants in the nacelle are transmitting data in so called messages. Different messages can be sent with different transfer rates. Hence, the input channels should be allocated carefully to separate messages in order to avoid creating redundant data (e.g. acceleration measurements in message A and torque measurements in message B). Figure 9 shows the CAN bus settings in the Dewesoft for the message, in which the nacelle acceleration measurements are transmitted.

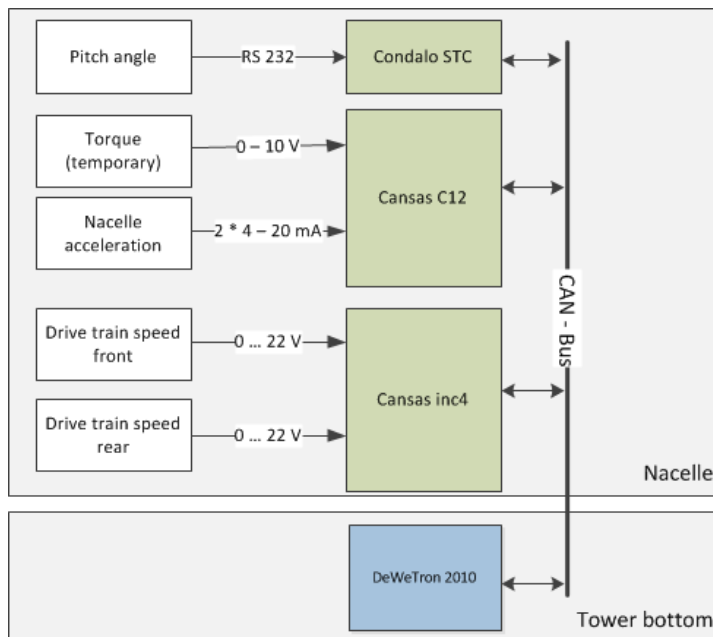


Figure 12: Overview of the CAN bus structure and participants

All CAN bus participants are physically connected to each other by at least a two wire system – CAN high and CAN low [4]. In the E30 a third wire is used to provide a common ground potential for all participants. The modules in the nacelle and the tower bottom are physically connected with a 50 m cable. Hence, the maximum usable baud rate is 500 kbit/s (see Table 1). All participants of a CAN bus must have the same baud rate as otherwise the bus crashes.

Table 1: Relationship between maximum bus length and usable baud rate [4]

Baud rate (kbit/s)	Bus length (m)
1000	30
500	100
250	250

The Condalo module is used to transmit the distance measurement for the pitch angle calculation (see chapter on Pitch Angle Measurement).. It converts the RS 232 signal to a CAN bus signal. The firmware of the module is modified, so it transmits data whenever it receives a new measurement from the laser distance sensor. This results in a transfer rate of 500 Hz. It transfers the measured distance as a five digit number in ASCII format followed by a carriage return. As one byte is used for each character the total data part of the message consists of six bytes.

The Cansas inc4 module is used to calculate the rotational speed of the main shaft from a rectangular voltage signal. This signal is created by an optical sensor (see chapter on Rotational Speed Measurement). The counting frequency of the module is 32 MHz, which allows calculating the frequency of the rectangular signal very precisely. It transmits the calculated data with its maximum transfer rate of 1000 Hz on the bus. The combination of a 16-bit resolution and the needed maximum frequency results in distinguishable frequency steps of 14.9 mHz, which is well sufficient for the needed precision of the rotational speed measurement.

The Cansas C12 module can be used for current and voltage measurements. Current signals are converted into standard voltage signals (± 10 V) by Knick isolation amplifiers. Hence, the C12 itself only measures voltages. The use of isolation amplifiers allows a maximum of flexibility as the input signal of each channel is variable. The C12 can measure and transfer each channel with a maximum rate of 500 Hz. However, as this project focuses on lower frequencies the transfer rate was set to 50 Hz to reduce the load on the bus. This transfer rate allows analysing oscillations with a maximum frequency of 25 Hz (Nyquist-Shannon-theorem [5]).

Using the settings listed above the load of the bus can be calculated. The results are summarised in Table 2. In addition to the data bits, each message consists of an overhead of 47 bits in the standard identifier format. Furthermore, so called stuffing bits are used whenever a certain number of consecutive bits are dominant or recessive. These bits are needed to ensure a reliable transmission. A comprehensive description of the bus protocol can be found in [4]. With the current settings the bit rates of all participants sum up to 208 kbit/s. This is well below the usable baud rate of 500 kbit/s. Hence, a reliable communication is ensured.

Table 2: CAN bus participants and corresponding bit rates

Participant	Measured value	Message ID	No of channels	Data bits per channel	Data bits per message	Max. no of stuffing bits	Bits per message incl overhead	Transfer rate	Bit rate
C12 Voltage	Reserve	100	3	16 bit	48 bit	16 bit	111 bit	50 Hz	6 kBit/s
C12 Current	Acceleration of nacelle	101	3	16 bit	48 bit	16 bit	111 bit	50 Hz	6 kBit/s
C12 Current 2	Reserve	102	3	16 bit	48 bit	16 bit	111 bit	50 Hz	6 kBit/s
C12 Torsion	Torque on shaft	103	3	16 bit	48 bit	16 bit	111 bit	50 Hz	6 kBit/s
inc4	Rotational speed	104	4	16 bit	64 bit	19 bit	130 bit	1000 Hz	130 kBit/s
condalo	Pitch angle	700	6	8 bit	48 bit	16 bit	111 bit	500 Hz	56 kBit/s
Aggregated bit rate for all participants									208 kBit/s

Two switch cabinets are attached to the backside of the generator using magnets. These contain all equipment for the sensor supply in the nacelle and the data transmission between nacelle and

tower bottom. Figure 13 shows the larger of the two switch cabinets. The power supply is provided via a cable from the tower bottom. Thus all measurement equipment in the wind turbine (tower bottom and nacelle) can be backed-up with one uninterrupted power supply in the tower bottom.



Figure 13: Switch cabinet in the nacelle with analogue to CAN bus converter in top-left corner

Measurement System for Electrical Quantities

The electrical part of the drive train of the Enercon E30 consists of an electrically induced synchronous generator and a full scale converter. Hence, it is reasonable it measure the voltage and the current at least in three locations: on the generator side of the inverter, in the DC link, and on the grid side of the inverter (see Figure 14; Appendix A for datasheets). The measurement software of the Dewetron (Dewesoft 6.6.7) is able to compute all needed electrical values from these measurements, namely active and reactive power values as well as generator and grid frequencies.

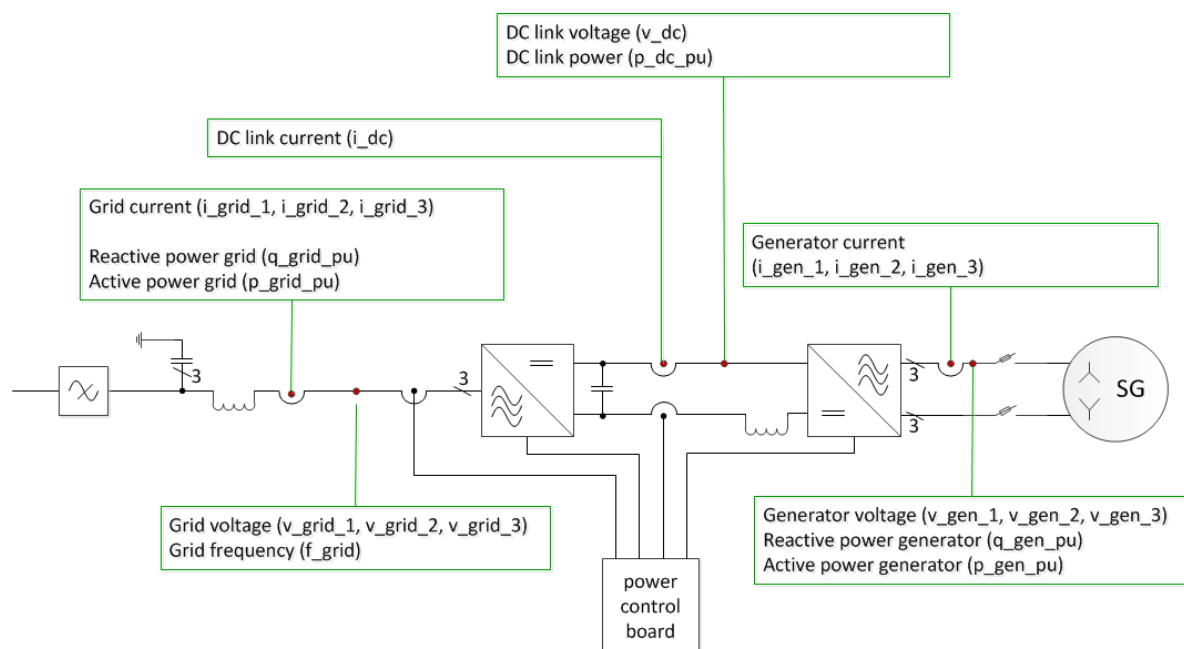


Figure 14: Overview of measurement locations for electrical quantities in the wind turbine

The electrically excited synchronous generator is connected to the inverter with two three-phase systems. Due to limitations of the input terminals of the used measurement system, it is only possible to measure voltages and currents in one of these systems. It is assumed that the voltages and currents are identical in both systems. The generator has 24 pole pairs. Hence, the relevant frequency range for the measurement during power production is 7.2 Hz – 22 Hz (18 RPM – 55 RPM).

The generator voltage is measured directly at the input terminals of the generator side of the inverter (see Figure 15). The Dewetron is able to measure the voltage by means of high voltage analogue-digital-converters (ADC).



Figure 15 Measurement of generator voltage (left) and generator current (right) in the tower bottom

Rogowski coils by Chauvin Arnoux are used to measure the generator current (see Figure 15; Appendix A for the datasheet). They convert the generator current into a ± 3 V voltage signal, which can then be measured with a low-voltage ADC in the Dewetron. Figure 16 shows instantaneous values of the generator voltage and current. It is obvious that voltage and current are far from being sinusoidal. The influence of the generator side inverter is also clearly visible.

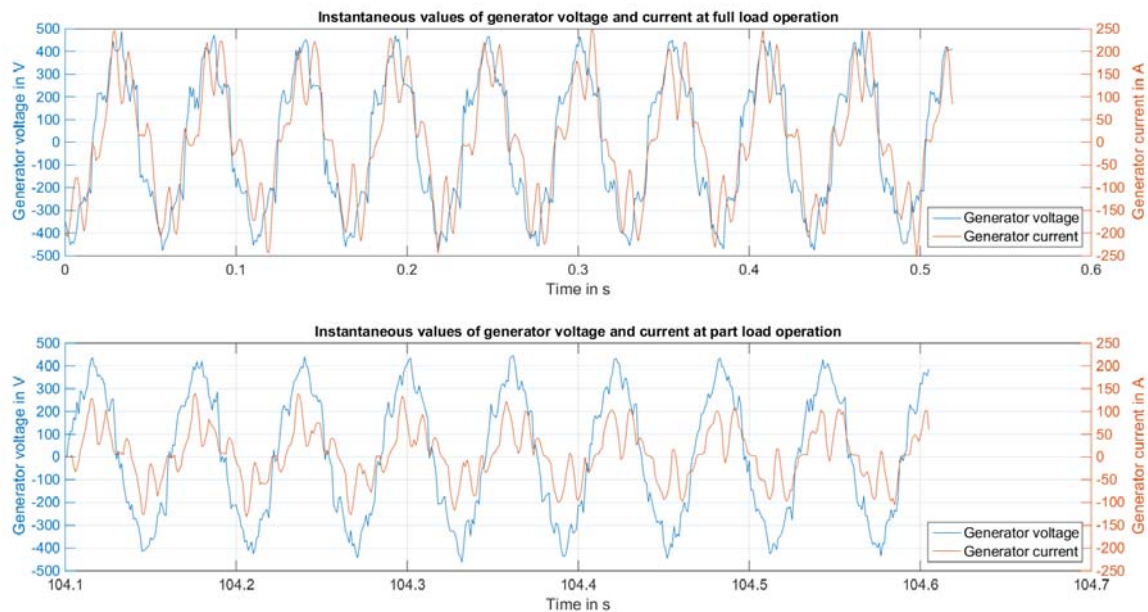


Figure 16: Instantaneous values of generator voltage and current of one phase for full load operation (top) and part load operation (bottom)

The generator voltage is depending on the rotational speed. In the upper range of the rotational speed the voltage only shows a small dependency, while it has a much stronger effect in the lower range (see Figure 17). This is most likely due to the electrical excitation of the generator. The excitation current is kept at its maximum in the lower range and thus cannot be increased to stabilise the voltage of the generator. At higher rotational speeds the induced voltage is sufficient to operate the DC link. With increasing rotational speed the excitation current can gradually be reduced, and thus the change of the generator voltage can be controlled better.

The DC link voltage changes with the rotational speed too (see Figure 17). However, in the lower rotational speed range it is almost constant, while the generator voltage shows a very strong dependency on the rotational speed. Enercon uses a step-up-converter (SUC) in the DC link of the E30, which keeps the DC link voltage at a sufficient level even in the low rotational speed range. The influence of the SUC is visible in the measurements as the DC voltage is measured on the grid side of the step-up-converter.

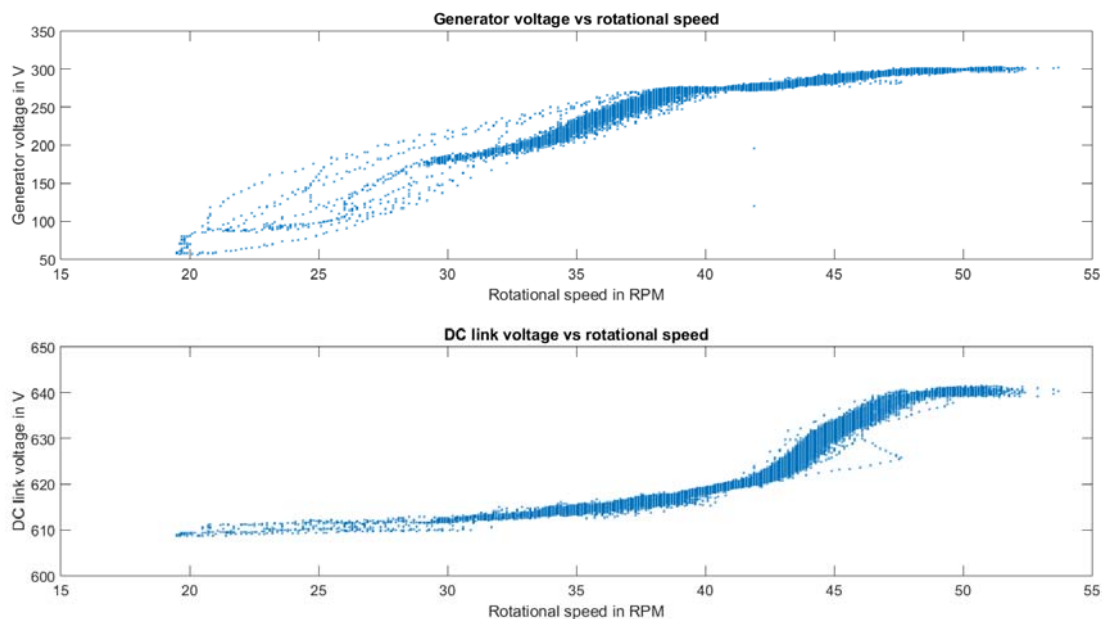


Figure 17: RMS values of generator voltage vs rotational speed (top) and voltage in the dc link vs rotational speed (bottom)

The DC link voltage is measured directly on a control board via a high voltage ADC in the Dewetron (see Figure 18). For the current measurement a LEM hall sensor is used (see Figure 18; Appendix A for the datasheet). It converts the DC current to a 0 – 4 V voltage signal, which is also measured by low-voltage ADC in the Dewetron.

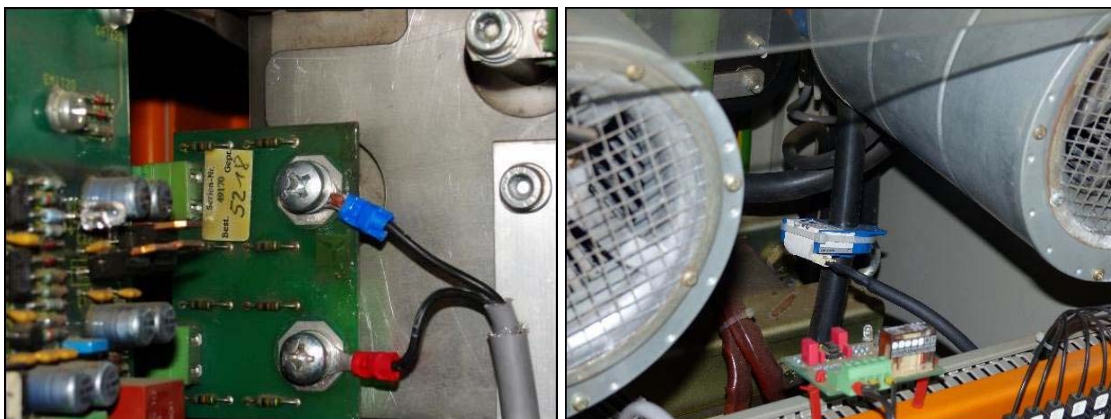


Figure 18: Measurement of DC link voltage (left) and DC link current (right) in the tower bottom

During power production operation the voltage in the DC link changes linearly between 610 V and 640 V with the grid power. The current varies between 0 A and 390 A. As mentioned

above, the DC link voltage is measured on the grid side of the step-up-converter. Due to limited accessibility in the switch cabinet, the DC link current can only be measured on the machine side of the step-up-converter. Hence, the measurements surpass the DC link power, when the step-up-converter is active (grid power below 0.25 p.u.).

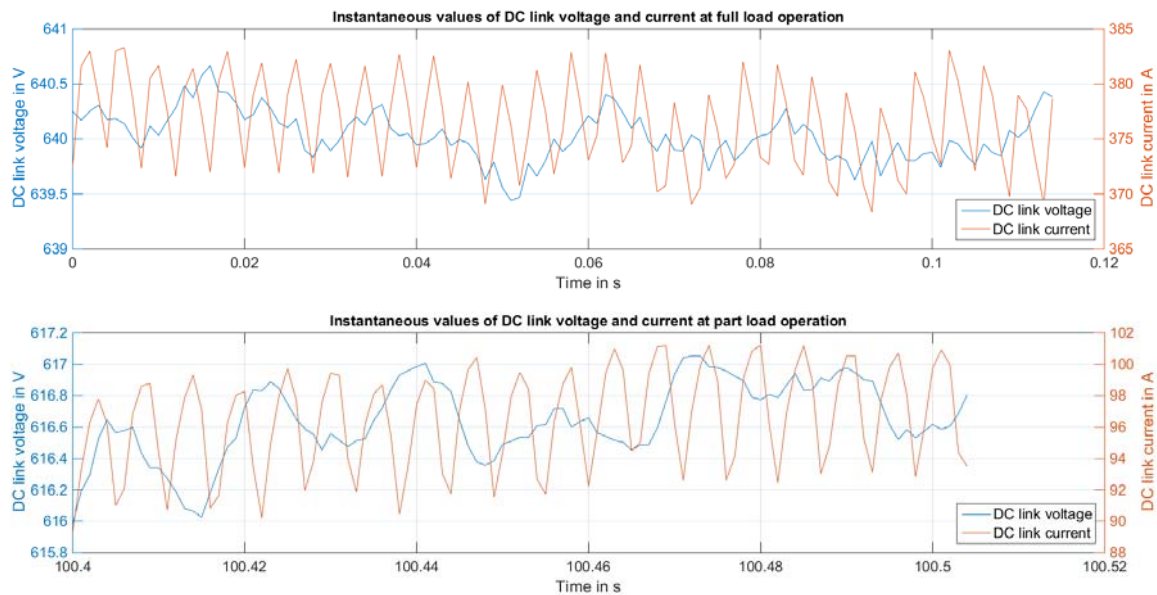


Figure 19: Instantaneous values of DC link voltage and current for full load operation (top) and part load operation (bottom)

The grid side voltage is measured near the main switch directly via a high-voltage ADC in the Dewetron (see Figure 20). The grid current is also measured near the main switch. PEM Rogowski coils (see Appendix A for the datasheet) are used to convert the current into a ± 6 V signal, which is measured by low-voltage ADC.

Figure 21 shows instantaneous values of the grid current and voltage. Although the reactive power set point is constantly at 0 p.u. a phase shift between voltage and current is clearly visible, especially during low power production. Hence, the turbine always exchanges some reactive power with the grid.

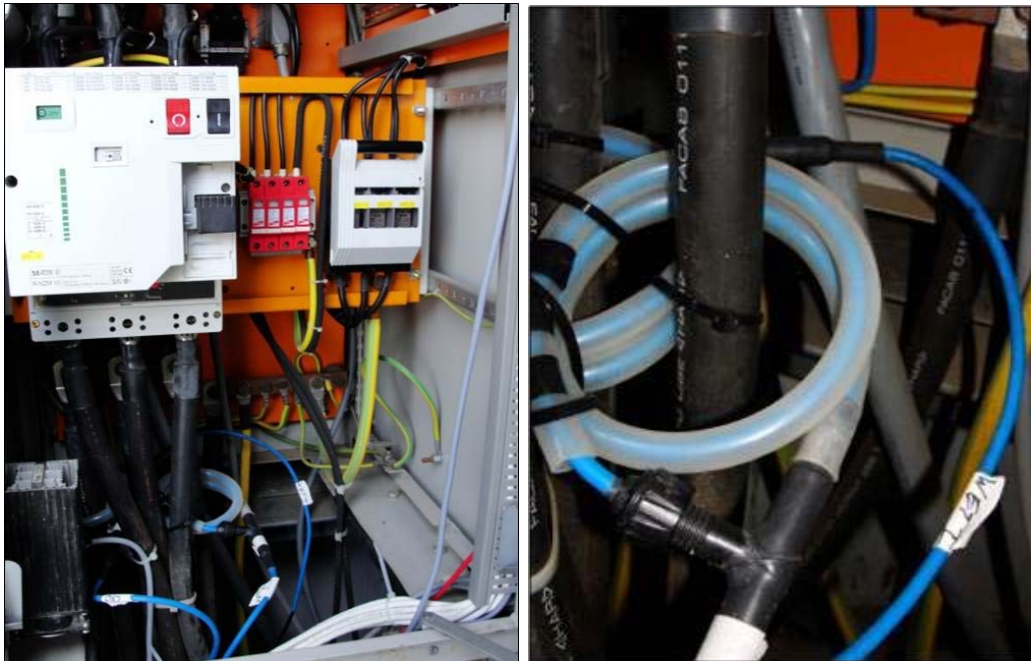


Figure 20: Measurement of grid voltage (left) and grid current (right) in the tower bottom

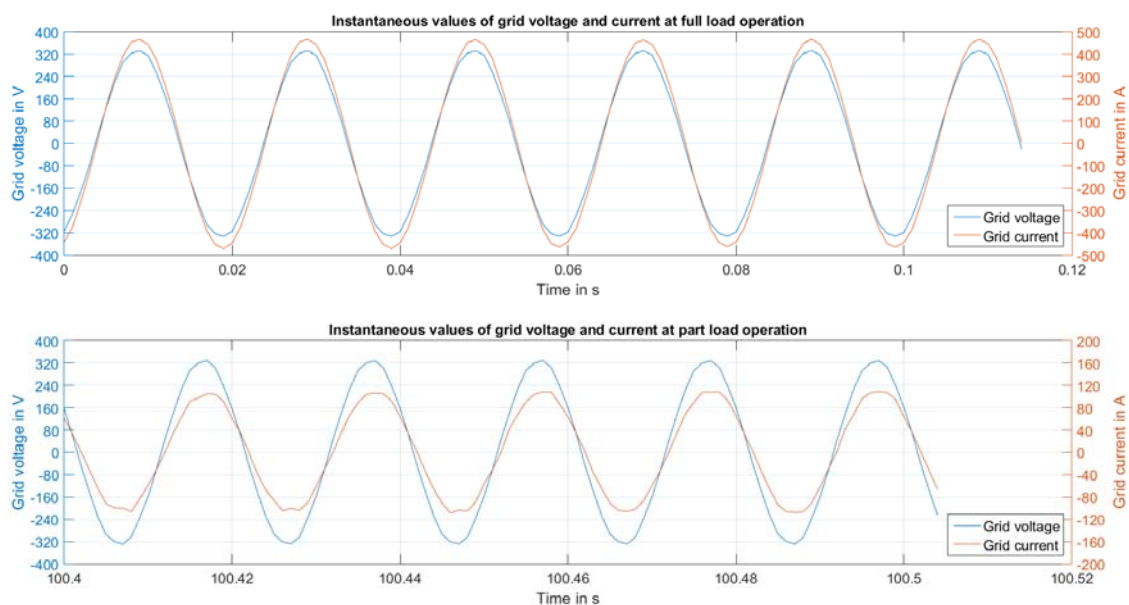


Figure 21: Instantaneous values of grid voltage and current of one phase for full load operation (top) and part load operation (bottom)

Measurement System for Mechanical Quantities

Longitudinal and Lateral Acceleration Measurement in Nacelle

The longitudinal and lateral acceleration of the nacelle is measured with an acceleration sensor by DMT (see Appendix A for the data sheet). The sensor measures the change in capacity of a micro-electro-mechanical system. It was especially designed for the use in wind turbines. Hence, the linear frequency range of 0.04 Hz to 3 Hz is very suitable for the relevant frequency range. The most important frequency for the acceleration is the first Eigenfrequency of the tower, which is roughly 0.46 Hz. The value is known from the documentation of the structural analysis (see Appendix B). The sensor is installed on a mounting plate, which is glued to the back of the main bearing almost directly above the centre of the tower (see Figure 22). The sensor converts the measured acceleration into two 4 – 20 mA signals, which can be measured by the Cansas C12 module and transferred via the CAN bus to the Dewetron.



Figure 22: Installed acceleration sensor view from the left side (left) and upper side (right)

Figure 23 shows the time trace of a typical measurement during the start-up of the turbine. The longitudinal acceleration is usually weaker than the lateral acceleration. This can be explained by the strong aero dynamical damping in longitudinal direction. Furthermore, the tower Eigenfrequency is dominating the frequency spectrum of the lateral acceleration much more than the spectrum of the longitudinal acceleration. The tower is excited in longitudinal direction with the wide band of the frequencies in the wind, which is almost white noise for the frequency range of the sensor. By contrast, the excitation in lateral direction is dominated by a mass imbalance in the rotor, which is seen as a 1p effect by the tower and is close to the first Eigenfrequency of the tower during low power production (grid power ~ 0.1 p.u.).

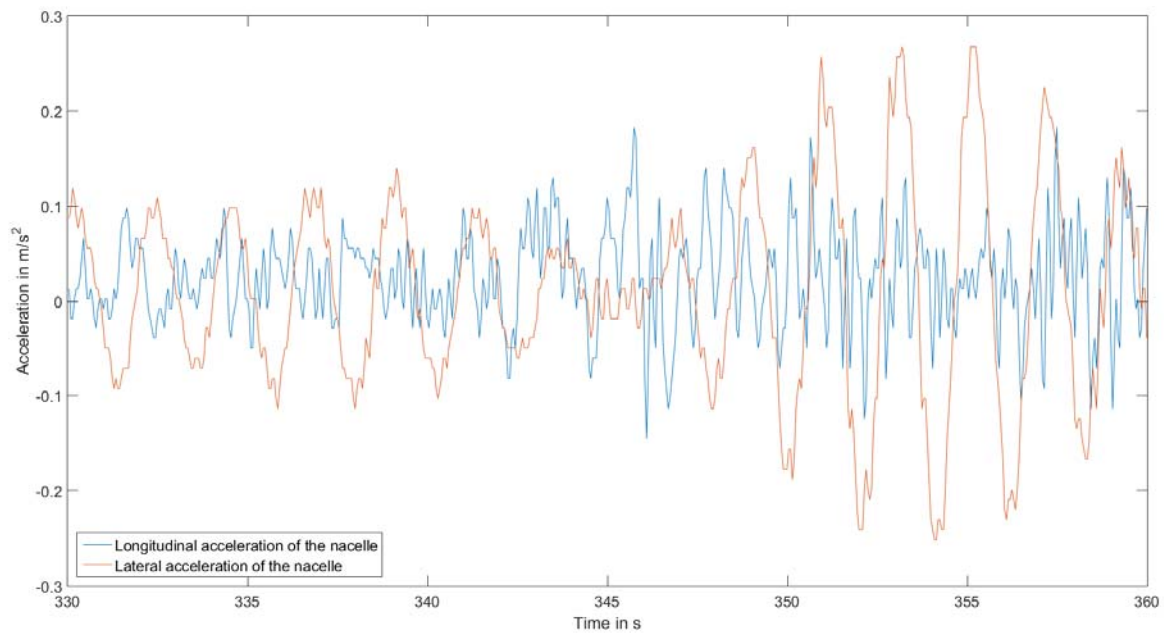


Figure 23: Plot of longitudinal and lateral acceleration measurements of the nacelle

During low wind speeds the rotational speed of the rotor is close to the first Eigenfrequency of the tower. When the wind turbine remains in the critical speed band for a longer period strong lateral oscillations occur. The wind turbine is shut down occasionally, when these oscillations reach a critical threshold. Figure 24 shows a time series of acceleration measurements at the beginning of such an event. The first Eigenfrequency of the tower of 0.46 Hz is clearly visible in both directions. It has to be noted that the lateral acceleration is in the order of one decade larger than the longitudinal acceleration.

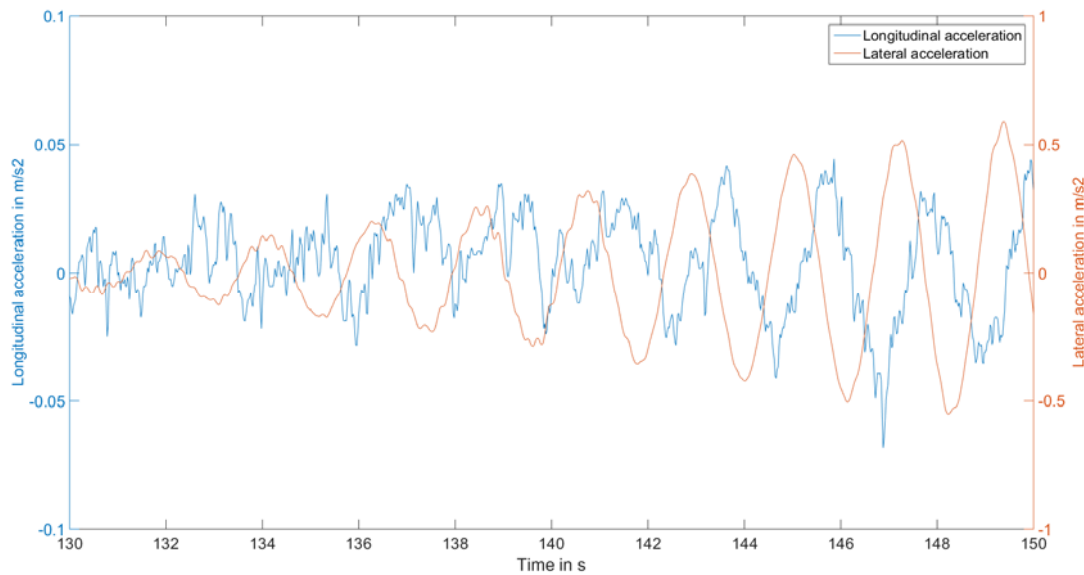


Figure 24: Plot of longitudinal and lateral acceleration measurements of the nacelle with a critical rotational speed

The acceleration sensor was validated with a camera by measuring of the tower oscillations during idle operation. The camera was mounted on the nacelle and films a measuring tape at the bottom. The video shows oscillations in both directions. By overlaying single frames extracted from the video it was possible to measure the amplitude of the oscillation (see Figure 25). These measurements of the deflection of the tower head were compared with the amplitude of the deflection calculated from the acceleration measurements. Both measurements were synchronised by the beginning of a yawing process. This is obviously visible in the video. In the measurement system it can be recognised by power consumption of the yaw motors, which is visible in the grid power measurement. Both measurements of the deflection of the tower head showed a good agreement with a deviation of less than 2.5 %.



Figure 25: Single frame extracted from the video during the validation of the acceleration sensor

Measurement System for Assessing the Blade Dynamics

The rotor blades are the softest part of the mechanical drive train of the E30. Hence, their dynamics have to be analysed in order to determine the Eigenfrequencies. The analysis focuses on the first Eigenfrequencies in flap-wise and edge-wise direction. The relevant range (1 – 3 Hz) is known from a previous project at the UAS Flensburg [6].

The blade dynamics are assessed with two measurement systems:

1. A camera mounted on the spinner of the rotor filmed the blade tip while the wind turbine was running.
2. A laser distance sensor is installed at the tower of the E30. It measures the distance of the blade tip to the tower, while the blade is passing the sensor.

The camera measurements are performed with a GoPro Hero 3 (see Appendix A for the datasheet). The camera allows recording the blade oscillations with 50 frames per second. Hence, the Eigenfrequencies of the blade can be determined with a sufficient accuracy to confirm the measurements from the previous project [6]. Figure 26 shows a single frame of such a video clip. The results are 1.65 Hz for the first flap-wise and 2.65 Hz for the first edge-wise Eigenfrequency.



Figure 26: Single frame extracted from the video for the assessment of the blade dynamics

Furthermore, the video shows the bending of the blade and its dynamics over the whole revolution of the rotor. The measurements at the met mast show a high roughness length and a very distinct vertical wind profile. This causes a strong change of the bending over one revolution, which is visible in the video.

A second measurement of the blade dynamics is performed with a distance laser sensor by micro-epsilon (see Appendix A for a data sheet). The sensor is installed on the outside of the tower by DNV-GL (see Figure 27). As the sensor is installed in a fixed position, it only measures the distance to the blade within in certain range of the yaw angle. Figure 28 shows a time series of such measurement. It shows how the measured distance is affected by the yaw angle. As the nacelle is yawing the distance between the blade and the tower is decreasing. Hence, the yaw angle must be considered when analysing the data. The data is recorded while the turbine was running in part load operation at about 30 RPM.



Figure 27: Distance laser sensor for the assessment of the blade dynamics

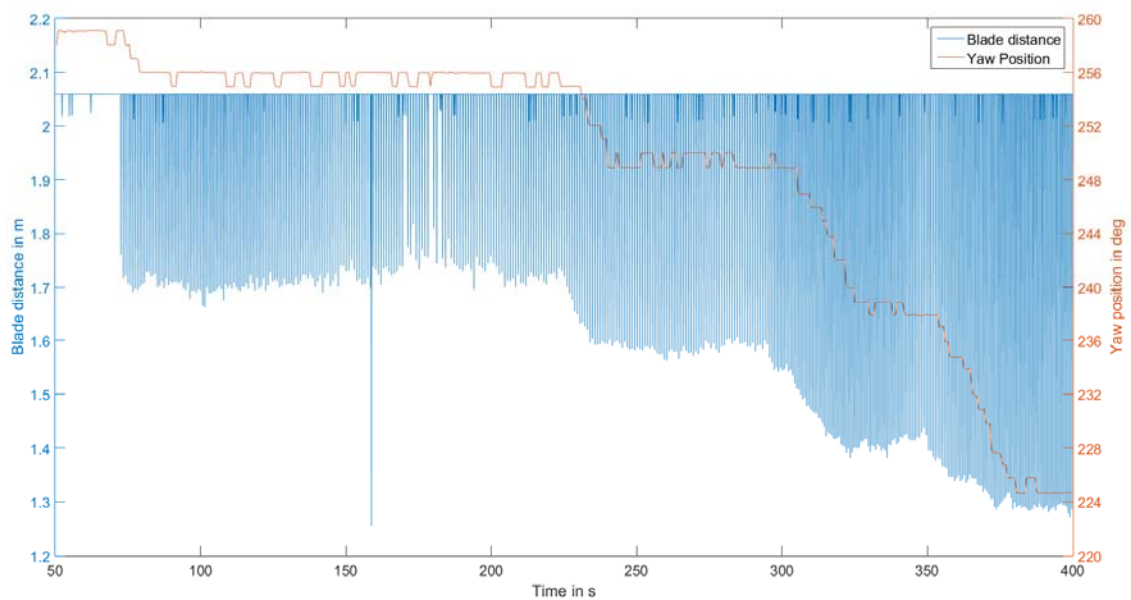


Figure 28: Measured distance between tower and blade and corresponding yaw position

The used distance laser sensor was chosen by DNV GL after an extensive market survey. The sensor did not fulfil all intended requirements as the linearity of the measurements was not high enough for the needed measurement frequency. Figure 29 shows a detailed measurement for one blade passage. As shown in the right side of the figure the measured distance varies during the passage of the blade. The shown variations are smaller than the expected error of the distance measurement. Therefore, it is not certain whether these oscillations show the real behaviour of the blade or are caused by the limited accuracy of the measurement. Hence, the recorded data could not be used for the intended purpose of assessing the blade dynamics. However, the sensor performance was sufficient to measure the distance between the blade tip and the tower (often referred to as tip-tower-clearance) with a sufficient accuracy, when a number of measurements are averaged.

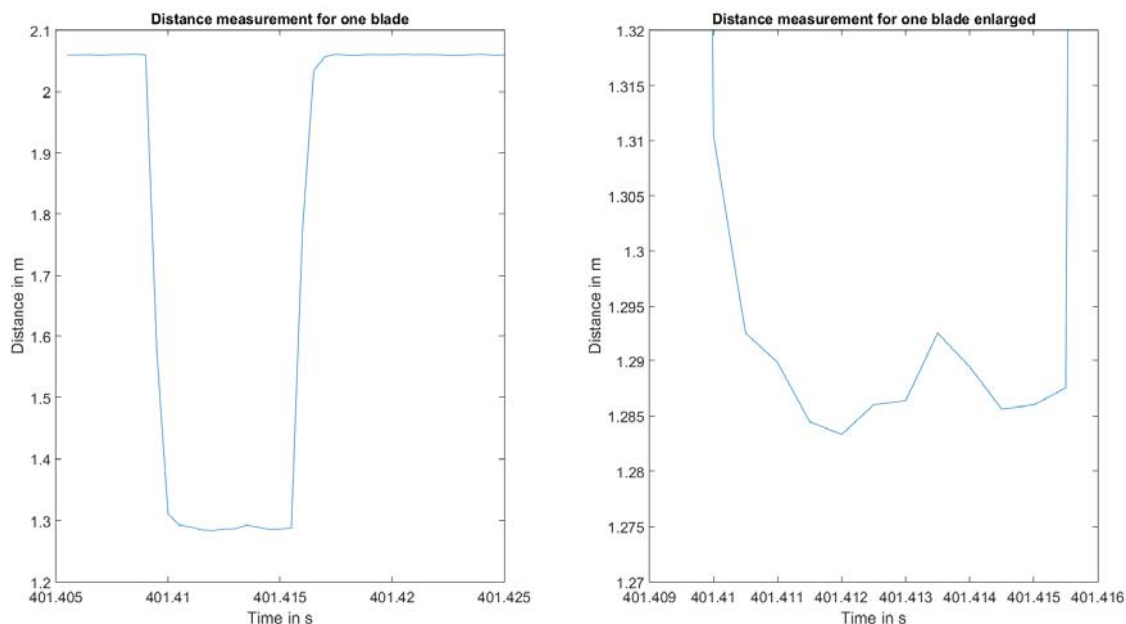


Figure 29: Extract of Figure 28 measured distance between tower and one blade (left), and enlarged (right).

Rotational Speed Measurement

An accurate measurement of the rotational speed is crucial for the control system of a modern (variable speed) wind turbine and can be considered being a basic, simple measurement task. It is often done by combining an inductive sensor and already existing angle indicators (e.g. drillings in the brake disc). This relatively slow measurement with just a few pulses per revolution is sufficient for controlling the rotational speed of the wind turbine.

The rotational speed measurement designed in this project has a different focus. The idea is to replace the measurement of the drive train torque by one or two rotational speed measurements with a high resolution. The drive train torque is usually measured by means of strain gauges, which are installed directly on the main shaft (also see chapter Torque Measurement on Shaft). Furthermore, a customised telemetry is needed to induce a voltage in the measurement equipment on the shaft and to transfer the signals. This makes the measurement complicated, vulnerable to disturbances and expansive. An accurate installation of the measurement also requires a high level of know-how.

If the rotational speed measurement shall successfully replace the torque measurement it has to fulfil the following tasks:

1. Measuring the twist of the main shaft, which is an indicator for the torque that acts on the shaft (see Equation 1).
2. Measuring the dynamics of the affecting torque (see Equation 2).

The twist of the shaft can be calculated by using Equation 1.

$$\theta_t = \frac{T \cdot l}{I_T \cdot G} \quad \text{Equation 1}$$

With

- θ_t : twist angle of the shaft (rad)
- T : torque (Nm)
- l : length of the shaft (m)
- I_T : torsion constant (m⁴)
- G : shear modulus (Pa)

The change of the rotational speed ω is connected to torque τ and the mass moment of inertia J by the well-known Equation 2.

$$\Sigma T = J \cdot \frac{\delta \omega}{\delta t} \quad \text{Equation 2}$$

Task one requires an accurate measurement of the position of the shaft on both ends of the drive train. The two positions are measured simultaneously at the beginning and at the end of a measurement interval and the difference is calculated. A change in the difference means, that the shaft has been twisted during the time interval. When it remains constant, the shaft has either not been twisted or positive and negative twists cancel out. This task is not achieved during the project. The current measurement setup with the data transmission via CAN bus does not allow to compute the time differences of the two rotational speed measurements accurately enough to measure a bending below 0.005 rad (at rated speed). It is planned to alter the

measurement setup in order to increase the accuracy significantly. This should allow measuring the twist of the shaft multiple times during one revolution with a sufficient accuracy.

The second task requires only a sensor at one end of the drive train. Several sensing measurement principles are compared and evaluated based on the following criteria:

1. Price: The cost of the chosen measurement system should be within a reasonable price range, which is around 500 € for the combination of a sensor and an angle indicator.
2. Installation process: Every conceivable system is only good if it is viable on the wind turbine. Hence, the possibility of errors during the installation process should be minimised. Furthermore, it should account for limitations of the desired measuring point.
3. Robustness: As the system is placed on a wind turbine, it must be as robust as possible. This means that it may not be easily affected. Problems may for example occur when parts of the system are unintentionally relocated by service technicians. Another problem may be soiling of parts of the measurement system.
4. Implementation into existing measurement system: The chosen system must be integrated into the existing measurement system in the wind turbine. Hence, the sensor must be connectable to the CAN bus.
5. Precision: Besides other limitations (e.g. the resolution of the CAN bus) the applied system strongly influences the achievable precision of the measurement system. The precision is measured by the maximum error of the measurement system. The error must be lower than the expected amplitude of oscillations to be measured. Hence, the maximum error of the chosen system should exceed ± 0.5 RPM ($\sim 1\%$ of maximum speed during normal operation) over the operation range of the drive train speed.
6. Frequency: The band of the measurement frequency is determined by the number of pulses, which can be measured during one revolution. The measurement frequency defines the maximum of the Eigenfrequency, which can be measured. In theory this relationship is described by the Nyquist–Shannon sampling theorem [5] (see Equation 3). However, to allow a clear identification of the oscillation a ratio of 1:10 between the measured frequency and the measurement frequency is desirable [5]. Hence, the chosen system should allow a measurement frequency in the order of 100 Hz over the operation range of the drive train speed. This criterion is in conflict with criterion five as an increase in the number of pulses typically means a decrease of the precision.

Due to restrictions in the choice of the measuring point, the sensor has to measure the drive train speed contactless. Reasonable measuring principles are identified in the literature and assessed. From all assessed principles optical and inductive system are most promising and are analysed in detail following the criteria mentioned above.

Both systems are using some kind of angle indicator, which is permanently installed on the main shaft, and a sensor which is converting the signal from the angle indicator into an electrical signal. The frequency of this signal is finally measured by an inc4 CAN bus module with a counting frequency of 33 MHz on its input side (see Figure 12 and Appendix A for the data sheet).

Figure 30 gives an overview of important terms, which are used in this chapter. It shows a zebra code as an example for an angle indicator with eight increments per revolution. The eight black and white stripes (zebra stripes) are creating eight pulses per revolution for the rotational speed measurement.

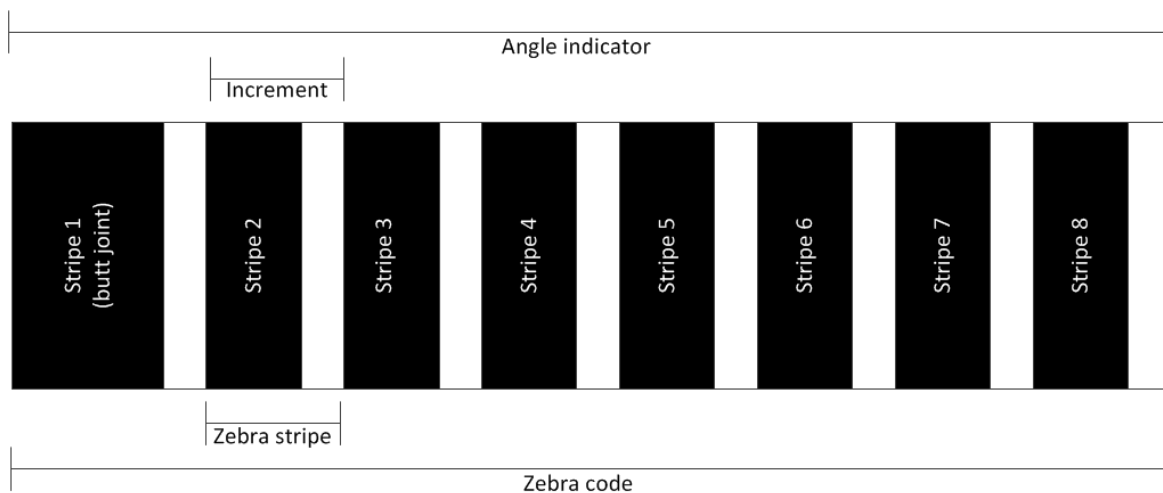


Figure 30: Terminology of the rotational speed measurement setup

A market survey of useable sensors shows, that both system can fulfil criteria one and four. The precision of the measurement system (criterion five) is mainly driven by the switching frequency of the used sensor and the number of increments per revolution. For a first approach any errors from the frequency calculation in the inc4 module can be neglected as its counting frequency is in the order of three decades larger than the switching frequency of assed sensors (see below). There are inductive as well as optical sensors on the market, which fulfil the requirements for the switching frequency (~ 50 kHz). Hence, both systems can fulfil the precision criteria. A detailed analysis of precision of the optical system is done below in the section on uncertainty analysis.

The measurement frequency of the system (criterion six) is determined by the number of increments of the angle indicator per revolution and the desired range of the drive train speed. As stated above, the relationship between the measurement frequency and the maximum

frequency, which should be detected, is described by the Nyquist–Shannon sampling theorem [5] (see Equation 3).

$$f_{\text{measurement}} \geq 2 \cdot f_{\text{detected,max}} \quad \text{Equation 3}$$

However, a higher ratio of 1:10 between the measured frequency and the measurement frequency is desirable [5]. During normal operation the rotational speed of the E30 varies between 18 RPM and 55 RPM (rated speed is 50 RPM). To achieve the desired measurement frequency (100 Hz) about 330 increments of the angle indicator are needed for one revolution. The maximum width of an increment can be calculated by dividing the circumference of the main shaft (1445 mm \pm 1 mm; measured with a tape measure) by the number of needed increments. Hence, each increment can about 4 mm wide. It proves to be very difficult to design such an angle indicator for the inductive system especially considering that the recommended metal/gap ratio is usually 1:2. Thus the metal bars can only be about 1.3 mm wide. There are little inductive sensors which can detect such small increments. Furthermore, these sensors have a very small operating range. Hence, they are very vulnerable to oscillations and have to be placed very close to the shaft. This is very critical with respect to safety issues. For an optical system a zebra code consisting of black and white stripes is chosen, which can be printed with a high precision on a self-gluing foil. The needed width of roughly 4 mm of one zebra stripe (i.e. the combination of one black and one white stripe) is easily achievable. Furthermore, standard contrast sensors have a light spot with a diameter of \sim 0.5 mm and can therefore detect the angle indicator without problems. Their scanning range is also high enough to allow a safe installation on the wind turbine.

As mentioned above the zebra code is self-gluing. Hence, the installation process (criterion two) is very simple. The major challenge is to install two consecutive codes parallel to each other. This proves to be problematic. Consequences for the precision of the measurement are addressed in the section on uncertainty analysis (see below). One major advantage of the zebra code is that the exact circumference of the shaft does not have to be known in advance. The installation of metal angle indicators would be much more complicated: especially ensuring a constant spacing of the indicators and handling the joint of the indicators after a full revolution.

The robustness of the system (criterion three) is the only advantage of an inductive system over an optical one. Optical systems are likely to be affected by soiling while inductive systems are almost completely unaffected by environmental disturbances. Nevertheless, an optical system is chosen. The advantages during the installation process and for the design of the angle indicators outweigh the need for regular maintenance.

The installed system consists of a contrast sensor (Leuze KRTM 20, see Appendix A for the data sheet) and a zebra code used as an angle indicator. An overview of the system, which is located at the rear end of the drive train shaft, is given in Figure 31. Besides, the used Leuze

sensor (red) the figure shows an outdated sensor (orange). A detailed view of the sensor and the zebra code is shown in Figure 32.



Figure 31: Overview of contrast sensor and angle indicator at the rear end of the drive train shaft

The zebra code consists of 361 combinations of black and white stripes. Each black stripe is 3 mm wide while each white stripe is 1 mm wide. The last black stripe overlaps with the first black one. Hence, one of the black stripes is roughly 3.5 mm wide. This so called butt joint is visible as a temporary decrease of the measured frequency (so called spike; discussed in the uncertainty analysis below). While this is problematic for the rotational speed assessment, it allows to determine the rotational speed and also the position of the drive train shaft with one sensor (see below).



Figure 32: Detailed view of contrast sensor and angle indicator

The electrical output of the sensor switches between 0 V (non-conducting) and ~ 22 V (conducting) depending on the optical input. The sensor is conducting whenever its light spot (with a diameter of 0.5 mm) is completely covering a black stripe. The output is a rectangular signal. In order to increase the reliability of detecting a black stripe the zebra code was designed asymmetrical (3 mm black and 1 mm white). The frequency calculation in the inc4 uses the rising edges of the rectangular signal. Therefore, it calculates the rotational speed by measuring the time between the detection of two consecutive black stripes and transmits the calculated signal via CAN bus to the measurement computer (see Figure 8). Figure 33 shows an overview of the installed measurement system.

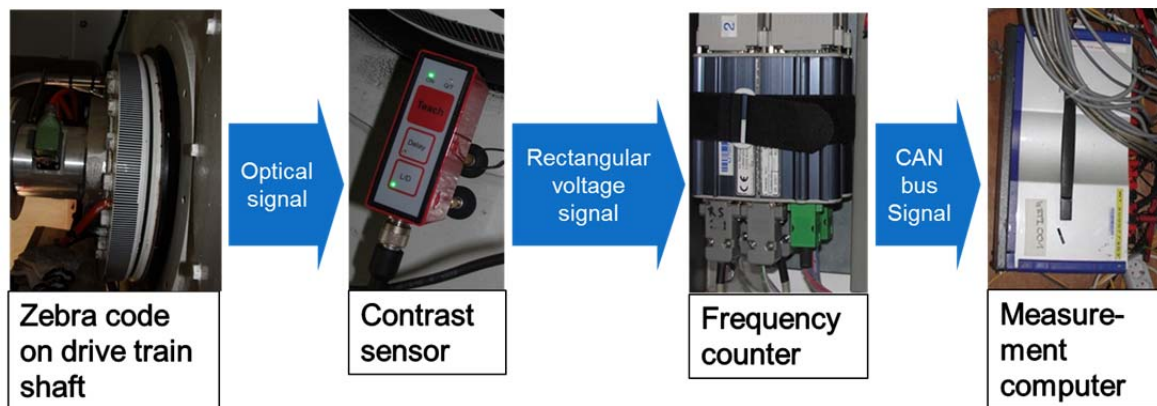


Figure 33: Overview of measurement system for measuring the rotational speed

In order to access the precision of the installed measurement system an uncertainty analysis is performed. Therefore, all influences on the rotational speed determination have to be identified. They are classified in deterministic and stochastic errors. Possible errors are identified following the determination of the rotational speed in Figure 33 from the zebra code to the measurement computer and are listed below:

1. The angle of the drive train shaft which is covered by the zebra stripes is not constant. While the overlay of the last and the first black stripe obviously results in an incorrect measurement, differences between other stripes have to be analysed in detail. These differences might occur due to imperfectly manufactured code, an imperfect installation of the code, and an imperfectly round drive train shaft. However, once the zebra code is installed, the angle between two individual stripes should remain constant. Therefore, it is assumed that this error is deterministic and can be corrected. Furthermore, this error is affected by soiling. Dirt patches might make a white stripe completely undetectable. This seems unlikely due to the sensor settings (complete light spot must detect a dark stripe to switch). More problematic is the accumulation of dirt at the edge of a black stripe. This might trigger a premature detection of the black stripe and hence lead to a false speed measurement. This error is analysed in detail below.
2. The beginning of a black stripe is detected imperfectly due to the limited measurement frequency of the contrast sensor. This is a stochastic error. Its magnitude is estimated below.
3. The output of the contrast sensor does not change instantaneously but after a short delay and with small oscillations directly before and after the output step (so called jitter). This is also a stochastic error. Its magnitude is also estimated below.
4. The time of the rising edge of rectangular voltage signal is detected with a delay by the frequency counter. However, due to the very precise time resolution of the inc4 (33 ns)

this stochastic error can almost be neglected. It increases with increasing rotational speed and reaches its maximum of $6 \cdot 10^{-4}$ RPM at 55 RPM.

5. A final error is due to the limited resolution of the CAN bus signal. Depending on the upper limit of the measurable speed and the data field length in the CAN bus message the resolution of the transmitted signal is limited. The inc4 allows a resolution of 14.9 mHz for the frequency measurement between two stripes. This results in a stochastic error of with a maximum magnitude of $2.3 \cdot 10^{-4}$ RPM. This error is constant over the whole speed range.

The influence of the drive train geometry and imperfections in the angle indicators on deterministic error is described in the literature [7]. The authors measured the rotational speed of a motor bike valve train on a test bench. In order to correct the deterministic error from the imperfections of the angle indicators, they calibrated the measurement while the shaft was decelerated with a constant rate. This method is not possible in this project as the wind speed and therefore also the rotational speed is constantly changing and not known well enough to calibrate the system. However, the rotational speed signal of the E30 shows clearly periodic patterns, which are repeated with every revolution. This is a clear indicator for a deterministic error in the measurements. Figure 34 shows a typical measurement of the rotational speed with 361 pulses per revolution (one per zebra stripe). The beginning of each revolution is easily detectable by the 10% decrease in rotational speed at the butt joint (downward spike). Also illustrated in Figure 34 is the average rotational speed over one revolution, calculated from the time stamps of the butt joints. Figure 34 also shows the need to address the difference in angles between consecutive zebra stripes in order to achieve the needed precision of the measurement system.

For the determination of the angle between the zebra stripes data sets of the rotational speed measurement between the 16th of August 2014 and the 10th of December 2014 are analysed. The identification of the angles i.e. the deterministic part of measurement error is problematic as the deterministic error cannot be separated from the stochastic error for single measurements. However, all stochastic errors have an expected error of 0 RPM and in the long term a certain distribution function (explained in detail below). By analysing a huge number of revolutions it should therefore be possible to determine the angle between consecutive zebra stripes and remove the deterministic error from the measurement. The angles are determined in seven steps:

1. Particular revolutions are identified in the time series of the rotational speed measurement signal by using the decrease in the rotational speed at the butt joint.
2. The time steps of the speed measurements at the butt joint are used to calculate the average rotational speed for each revolution. As only one pulse is used per revolution, the average speed can be calculated very accurately.

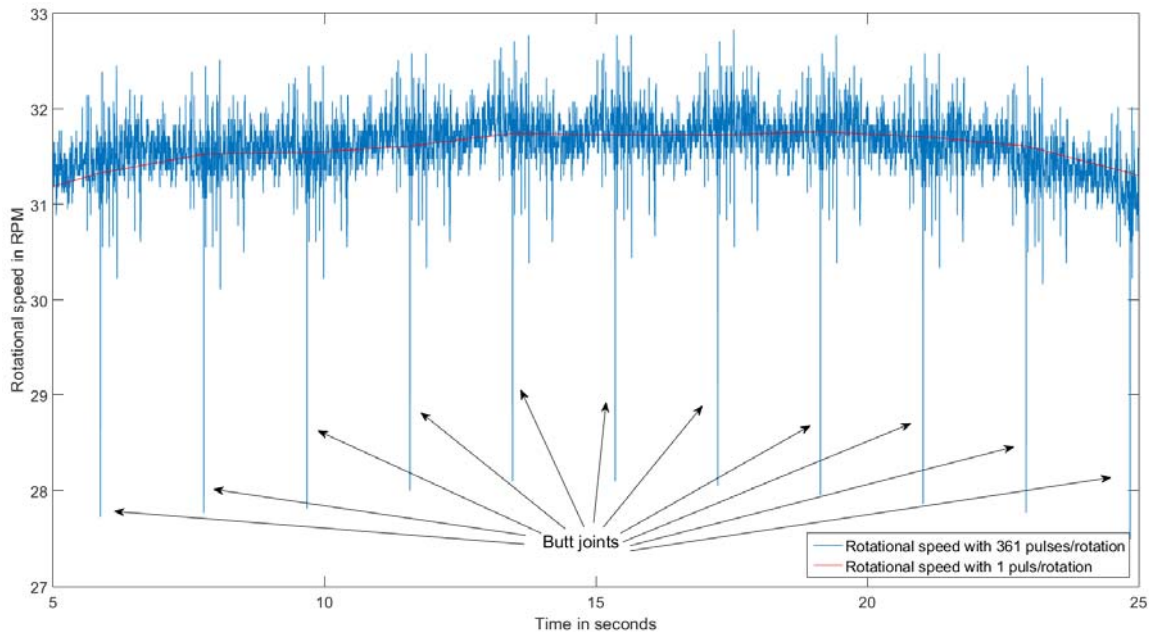


Figure 34: Rotational speed measurements for eleven revolutions with indicated butt joints

3. The start of each zebra stripe has to be identified in the measurements. The inc4 always transmits its measurement data with a constant frequency of 1 kHz via the CAN bus to the Dewetron. Between two measurements it uses a sample and hold function. Hence, the rotational speed signal in the Dewetron is a step function (see Figure 35). Depending on the rotational speed and therefore the frequency of the zebra stripes each measurement is transmitted between three times (at 55 RPM) and ten times (at 18 RPM). Usually, there are slight variations in the rotational speed measurements of two consecutive zebra stripes. This allows an easy identification of a new zebra stripe. Furthermore, an algorithm to detect a new stripe was developed for the rare event of two identical consecutive measurements. In combination with the easy identification of the butt joint it is possible to distinguish measurements from different zebra stripes from one another.

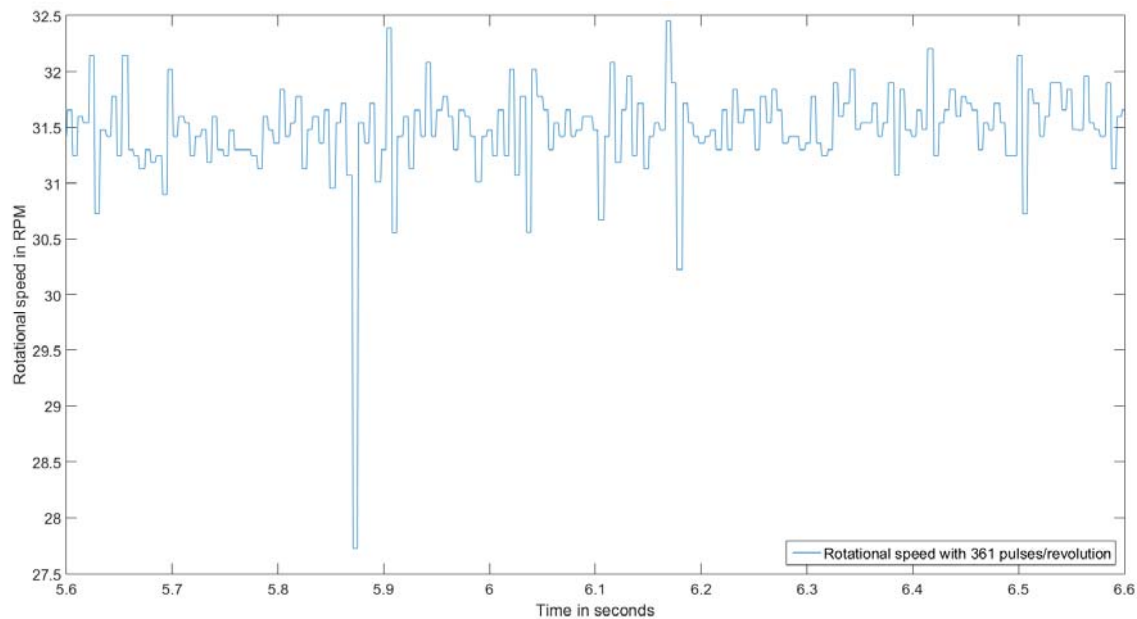


Figure 35: Extract of Figure 34 Rotational speed measurement for roughly half a revolution

4. Each measurement can be allocated to a distinct zebra stripe (see Figure 36) and a distinct revolution. The sample and hold function of the inc4 creates redundant measurements from one zebra stripe (see above). These are discarded. Hence, at the end of step 4 a matrix of rotational speed measurements is created with the revolutions as rows and the zebra stripes as columns.

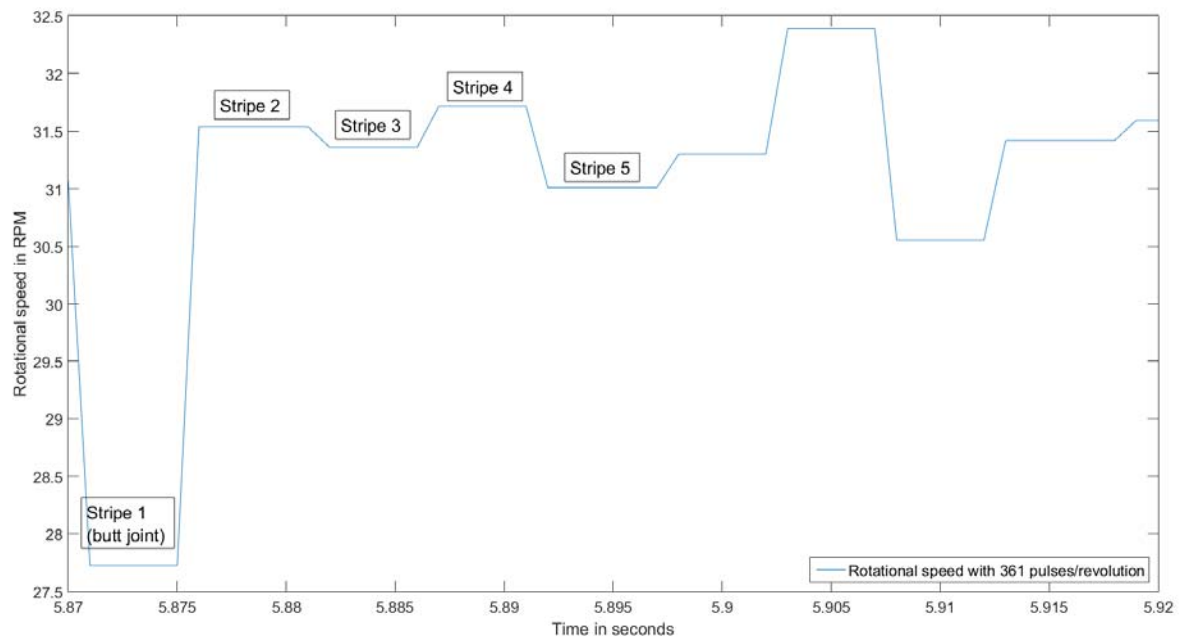


Figure 36: Extract of Figure 35 Example of the allocation of rotational speed measurements to zebra stripes

- Each of the measurements in this matrix is divided by the average speed of its related revolution (calculated in step 2). This implies that the rotational speed is constant for each rotation. While this approach is problematic during start and stop procedures it only has a small effect during normal operation, as deceleration and acceleration should occur equally frequent. The result of this step is a relative speed of each measurement in relation to the average speed of the corresponding revolution. Hence, values from different revolutions become comparable. Figure 37 shows a histogram of the computed values of the relative speed for zebra stripe 4 and 5 (see Figure 36). The histogram shows that the speed measurements of the stripe 4 slightly overestimate the rotational speed, while the measurements of the stripe 5 slightly underestimate it.

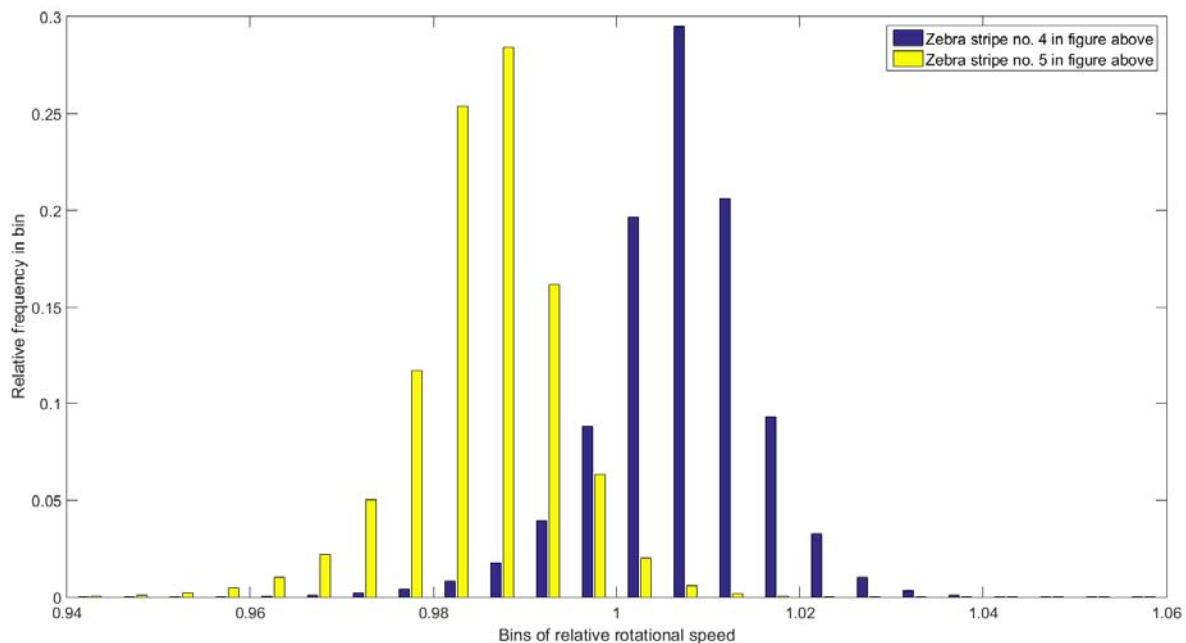


Figure 37: Histogram of the angle of zebra stripe 4 and 5 created from rotational speed measurements in August 2014 with 389,825 revolutions (bin width 0.005); measured rotational speed of the stripe is normalised with the average rotational speed of the revolution during which it was recorded.

6. For each zebra stripe the mean value of the relative speed over all analysed revolutions is computed. Due to the high number of analysed revolutions this average value is a measure for the deterministic error. The effects of the stochastic errors and of acceleration as well as deceleration are causing the Gaussian like shape of the density function in Figure 37. The average relative speed values of each stripe are later used to correct the measurements in the post-processing.
7. In theory each stripe of the zebra code should cover 4 mm of the total circumference of 1444.5 mm which corresponds with 0.997 deg of the drive train shaft. The stripe at the butt joint is slightly wider and hence should cover 1.121 deg. These values are divided by the average relative speed values calculated above. The resulting angles are shown in Figure 38.

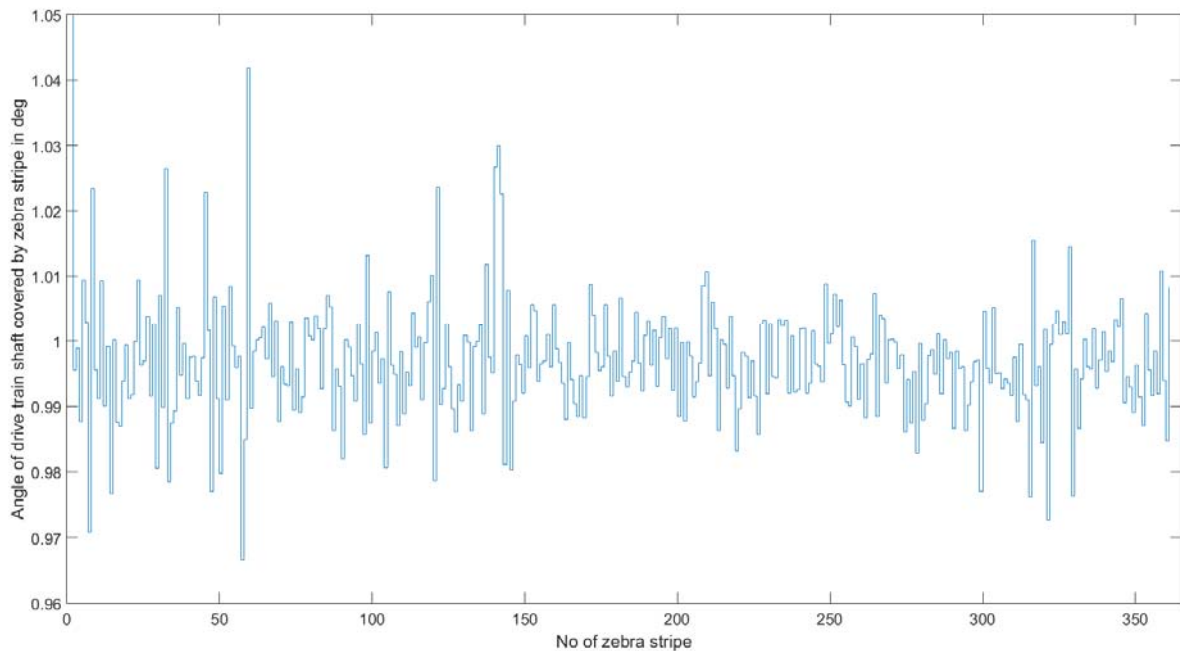


Figure 38: Angle between consecutive zebra stripes deduced from rotational speed measurements in August 2014 with 389,825 revolutions; Note: value for butt joint (1.129 deg) is above the scale of the y-axis

The affection of the measurement system by soiling is studied with the same data set. The zebra code was not cleaned during the analysed period. The black stripes of the zebra code are slightly higher than the wide stripes. Therefore, two effects are expected:

1. An accumulation of dirt on the leading edge of a black stripe (in direction of the rotation). This leads to an increase in relative speed for the preceding zebra stripe and a decrease in speed for the affected stripe.
2. An accumulation of dirt on the trailing edge of a black stripe (in direction of the rotation). This does not affect the measurement as only the time between two leading edges of two consecutive black stripes is measured.

In order to show the influence of soiling on the measurements the relative speed of each zebra stripe was calculated separately for each month in the analysed period. The values for August 2014 and December 2014 as well as the difference between the two months are shown in Figure 39. The maximum difference over the four months is about 1.5 %. The equivalent change of the width of a zebra stripe is 0.06 mm. From Figure 39 it is also obvious that the beginning and the end of the zebra code are stronger affected than other parts. This might be caused by a single event, when the drive train shaft was standing in a certain position when it was the zebra code was getting dirty e.g. during a maintenance event.

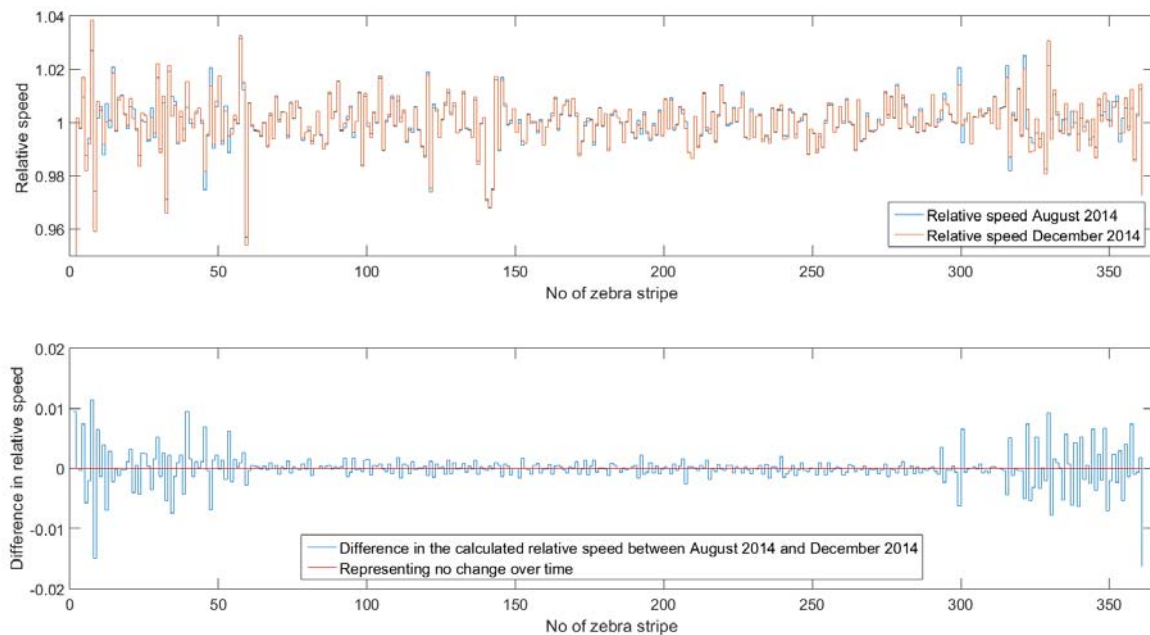


Figure 39: Relative speed of the zebra stripes for August 2014 and December 2014 (top) and the difference of the relative speed between the two months (bottom)

A maintenance event in June 2015 during which the main shaft was greased is an extreme example of such a singular event. The zebra code had to be cleaned afterwards. Figure 40 shows two time series of measurements at comparable rotational speeds. Both graphs show almost two revolutions. The top one was recorded before cleaning the code, the bottom one after cleaning the code. The soiling caused high variation in the measured rotational speed. Furthermore, two new spikes were induced in the measurement, which means that two zebra stripes were not identified at all. It has to be noted that the first zebra stripe after the butt joint was pasted over with a black stripe before the measurements. Hence, the downward spike at the butt joint is more distinct and therefore easier detectable in the measurements.

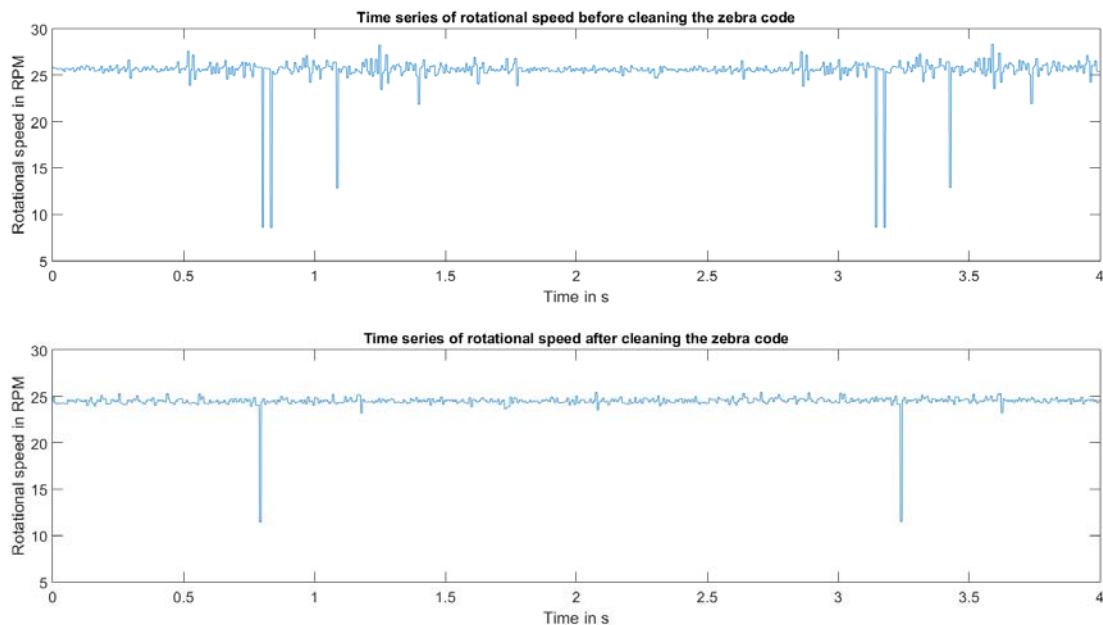


Figure 40: Influence of extreme soiling on the rotational speed measurement. Time series of rotational speed measurements before (top) and after (bottom) cleaning the zebra code

The results show the need for a regular cleaning of the code. Furthermore, it is advisable to check the speed measurements regularly and compute new correction factors if needed.

The high sensitivity of the measurement setup is mainly due to the low width of the zebra stripes. Wider stripes (which would result in a lower measurement frequency) would be a lot less affected by soiling.

Figure 41 shows a comparison of the rotational speed measurement before and after removing the deterministic error. The variations in the speed measurements have clearly been reduced and are within the allowed limits of the precision criterion. An estimation of the stochastic error which is caused by the limited frequency of the contrast sensor is given in the next section.

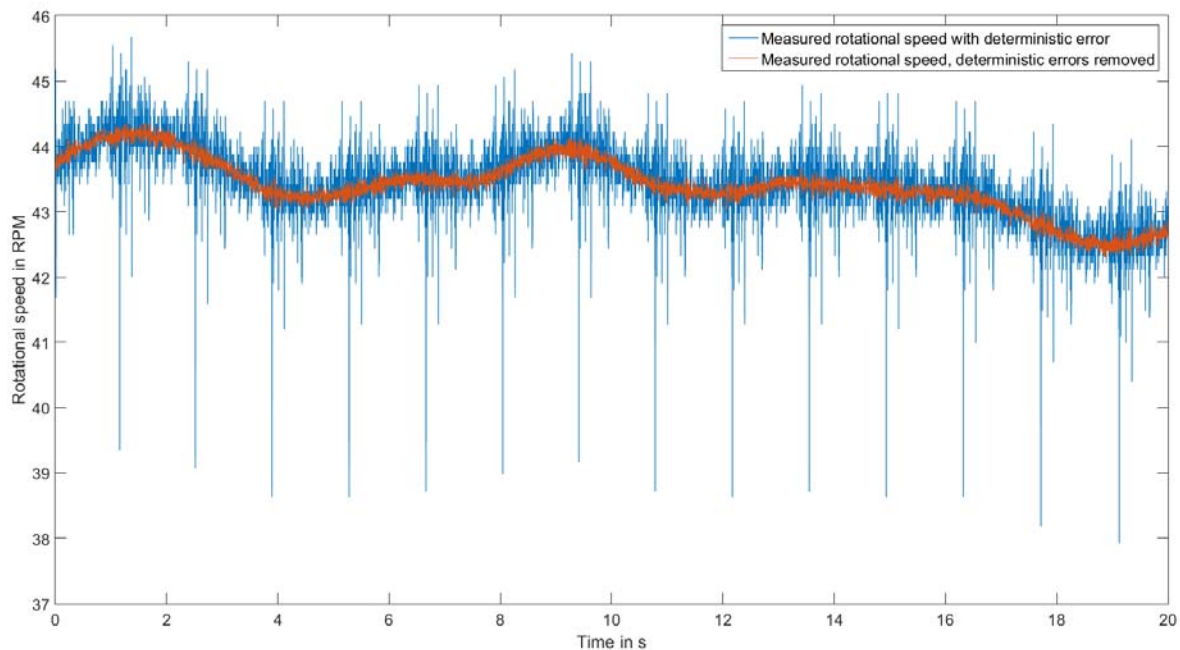


Figure 41: Comparison of rotational speed measurements before and after the correction of the deterministic error

The major stochastic error of the measurement system is caused by the contrast sensor. Due to the high number of pulses per rotation and therefore the small width of the zebra stripes a very fast sensor is needed. Nevertheless, the leading edge of the black stripe is never detected instantaneously. Figure 42 shows the effect of the limited sensor frequency (highly exaggerated as the sensor frequency is highly understated). The sensor can only detect the zebra stripes at the times marked with the red vertical lines. Hence, the output of the sensor changes with a time delay (Δt in Figure 42).

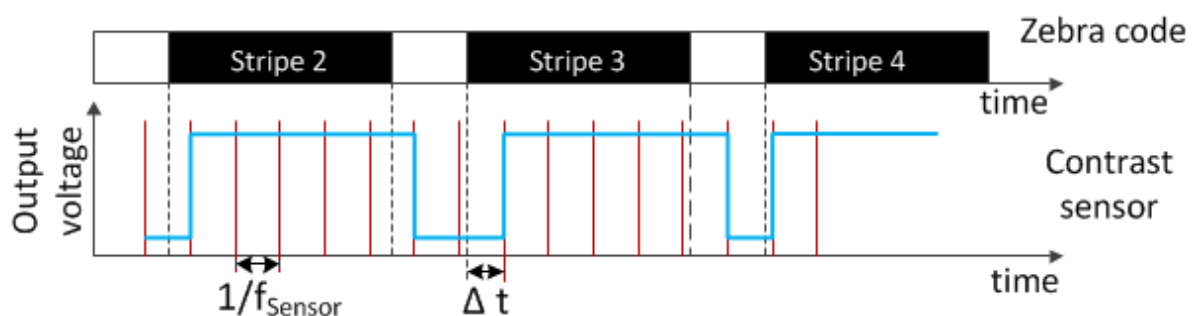


Figure 42: Effect of limited frequency of contrast sensor on the detection of the black stripe

The maximum time delay remains constant with the rotational speed. However, at higher rotational speed a larger part of the black stripe can pass the sensor during this time. Due to the delayed detection the angle between the leading edges of two consecutive zebra stripes is not constant any more. In Figure 42 the detected angle between stripes 2 and 3 is larger than the one between stripes 3 and 4. Hence, the rotational speed would be underestimated in the first measurement and overestimated in the second one. The time delay of the detection is assumed to be uniformly distributed between 0 and the maximum time delay and independent for consecutive stripes. The detected angle depends on two consecutive measurements. The resulting error of the rotational speed measurement can be described with a triangular distribution. The expected error is 0 RPM. The absolute value of the minimum and maximum error is equal and can be computed with Equation 4. The calculated value for the relevant rotational speed range is shown as the blue area in Figure 44.

$$|\varepsilon_{RPM,max}| = \frac{f_{zebra\ stripes} \cdot f_{rotation} \cdot 60}{f_{sensor}} \quad \text{Equation 4}$$

Jitter would have an effect on the precision of the measurement system, if the output of the sensor changed its output in a different way for consecutive voltage steps (e.g. a different time delay). To determine the effect of the jitter, several switching events of the sensor output are recorded with the maximum available measurement frequency of 100 kHz and are afterwards analysed (see left side of Figure 43). The signals of the three steps are overlaid by matching the oscillations before the voltage step (see right side of Figure 43).

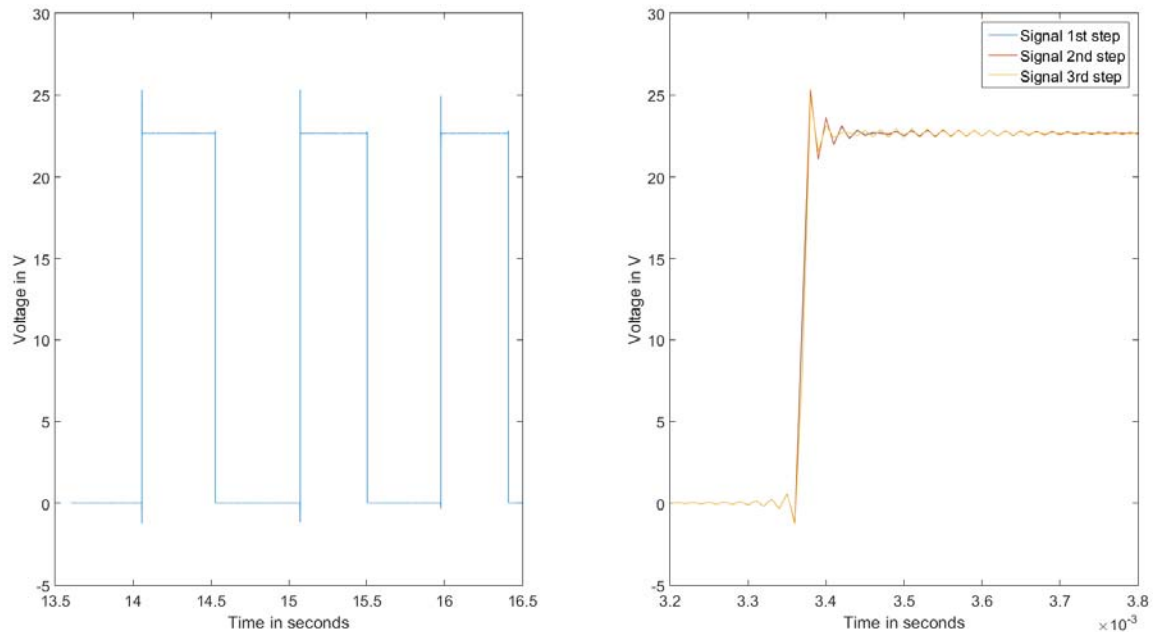


Figure 43: Output of the contrast sensor during jitter analysis; output signal vs time (left) and overlay of the three output steps (right)

While the oscillations of the signal show a different behaviour after the voltage step, the output signals rise almost simultaneously and very fast during all recorded steps (within $2 \cdot 10^{-5}$ s). Smaller differences, which might be measurable with a higher measuring frequency, are of minor importance for the precision of the rotational speed sensor (relative error below 0.05 % over the whole speed range). Furthermore, the inc4 only detects whether its input signal is at a high or a low voltage level. The threshold between high and low voltage is set to 12 V. Hence, only the rise time of the output signal to 12 V is important. Any oscillations after the output step can be neglected. It can be concluded that the jitter of the output signal of the contrast sensor can be determined sufficiently with the available measurement equipment. However, following a conservative approach the red area in Figure 44 shows a worst case scenario for the Jitter error, which most likely exaggerates the error.

The influence of all stochastic errors on the maximum absolute error is shown in Figure 44. It is obvious that the measurement error is largely dominated by the error resulting from the maximum switching frequency of the sensor. The error is below the limits set in the design criteria. The measurements agree well with the estimations of the error. An example is shown in Figure 41.

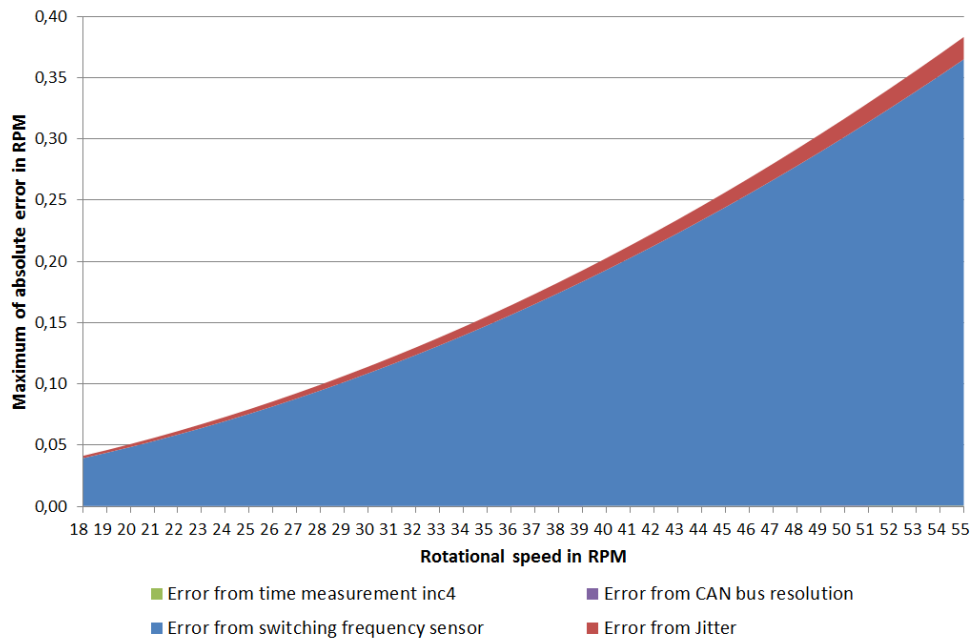


Figure 44: Maximum absolute error of the drive train speed measurement for all stochastic errors

The rotational speed was validated with a rotational speed measurement computed from the frequency of the generator voltage. As the E30 uses a synchronous generator the rotational speed ω can be calculated from the frequency of the generator voltage f_{gen} with the number of pole pairs p using Equation 5:

$$\omega = \frac{2 \cdot \pi \cdot f_{gen}}{p} \quad \text{Equation 5}$$

The calculated speed was compared to the average speed of one rotation. Both speed measurements showed a very good agreement with a difference of less than one percent. It is concluded that the designed rotational speed measurement is valid.

The rotational speed measurement can also be used to calculate the rotor position, which has to be known to measure the pitch angle at the different blades (see Pitch Angle Measurement). As the butt joint causes a spike in the rotational speed measurement the rotor position is known precisely once per revolution. For the time between two spikes the position can be calculated by integrating the rotational speed measurement. The spikes can be used to calibrate the calculation of the rotor position one time per revolution. Hence, errors caused by the numerical integration and incorrect rotational speed measurements can be removed. Figure 45 shows the calculated rotor position for approximately 16 revolutions. The calculation has to use uncorrected rotational speed as the spike is needed for the calibration (the downward spike is covered by the step in the rotor position in Figure 45). The last value before the step of the position to 0 deg

can be regarded as a measure for the accuracy of the method. It should be close to but below 360 deg. For this rotational speed range its value is $359.8 \text{ deg} \pm 0.1 \text{ deg}$ which is a good value regarding that the shaft moves about 0.25 deg during one timestep of the position calculation. Hence, the calculated position is sufficient for the intended purpose in the pitch angle measurement.

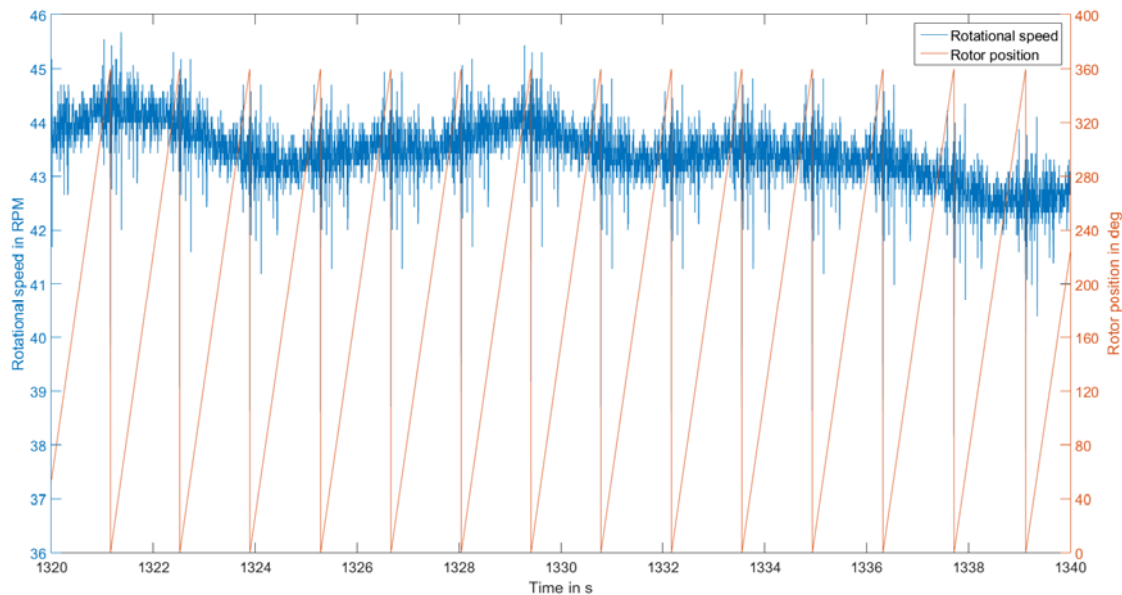


Figure 45: Rotational speed and calculated rotor position for several revolutions

Torque Measurement on Shaft

The torque measurement is intended to validate the rotational speed measurement. This is only partly possible due to certain effects described in this chapter.

The torque measurement consists of strain gauges, a telemetry and signal amplifiers. Due to the small size of the E30 the torque measurement has to be installed on the spinner side of the main bearing close to the brake disc (see Figure 46). One strain gauge and the telemetry are shown in Figure 46. The torque is measured by variation of the length of the strain gauges. This variation in length is mainly caused by the torsion. However, due to the position of the measurement the length of the strain gauges is also influenced by bending forces, which result from gravitational forces acting on the hub and the blades. As the strain gauges are rotating with the main shaft, the measurement setup causes a periodic superposition of the bending and the torsion. The bending forces are oscillating with the frequency of the rotational speed and are hence visible as a 1p effect in the torque measurements.

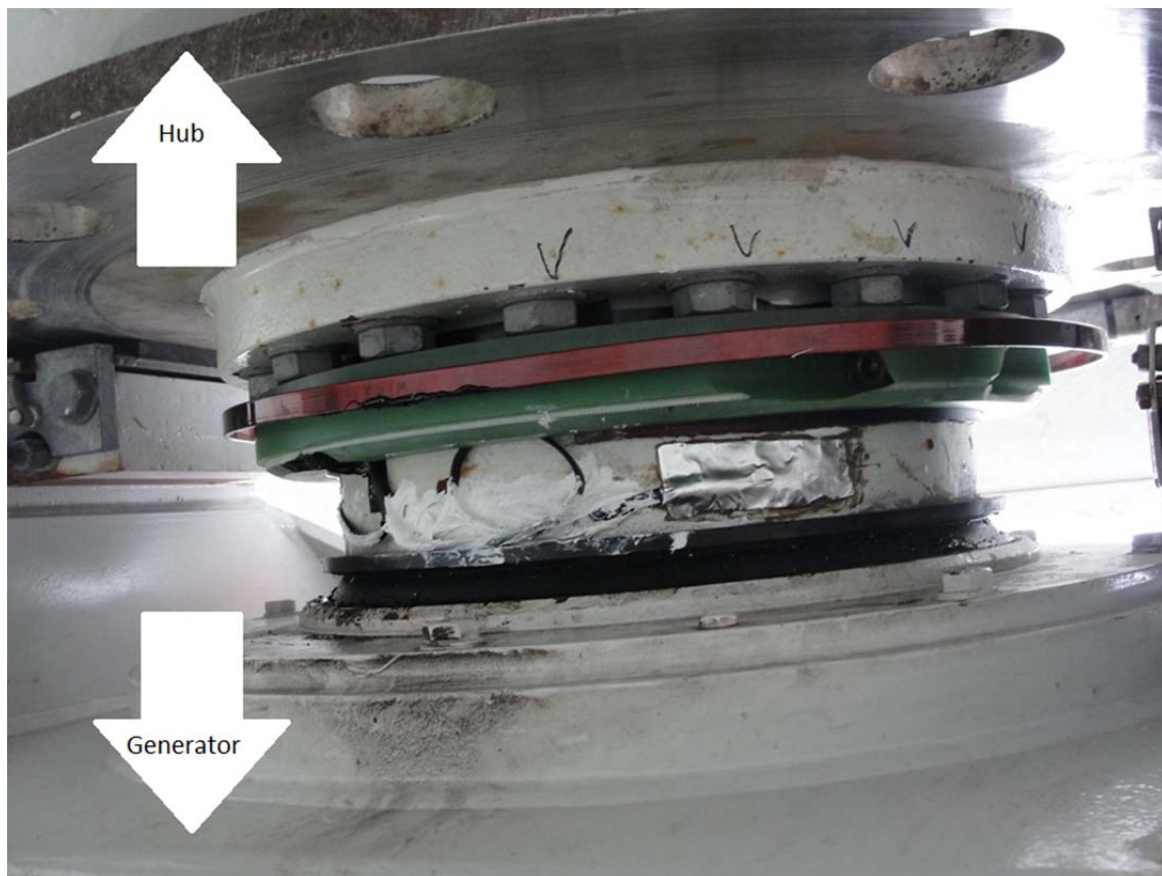


Figure 46: Torque measurement - strain gauge and telemetry

The E30 shows a strong tendency to lateral oscillations, especially for critical rotational speeds (see chapter on Longitudinal and Lateral Acceleration Measurement in Nacelle). The oscillations are caused by a mass imbalance of the rotor. The centrifugal force resulting from the mass imbalance is also visible as a 1p effect in the measurements. Hence, there are two forces with the same frequency superimposed in the torque measurement. Depending on the phase shift between the forces, the superposition might result in frequencies in the measurement, which do not exist in the real torque. A time series showing the strong 1p effect is shown in Figure 47.

The main shaft torque can be calculated from the measurements by referring the angle calculated with Equation 1 to the circumference. Three parameters are needed for the calculation:

- l : length of the shaft
- J_T : torsion constant
- G : shear modulus

The length of the shaft is measured on the turbine. The torsion constant depends on the geometry of the main shaft. It is estimated from a combination of measurement, pictures and drawings of the turbine. The shear modulus is a material constant. The calculated values are validated by calculating the power from the torque measurement and the rotational speed and comparing it with the generator power. Both measurements show a good agreement in the long term mean (see Figure 48). However, the 1p-effect of the gravitational forces is clearly visible in the instantaneous values of the calculated power.

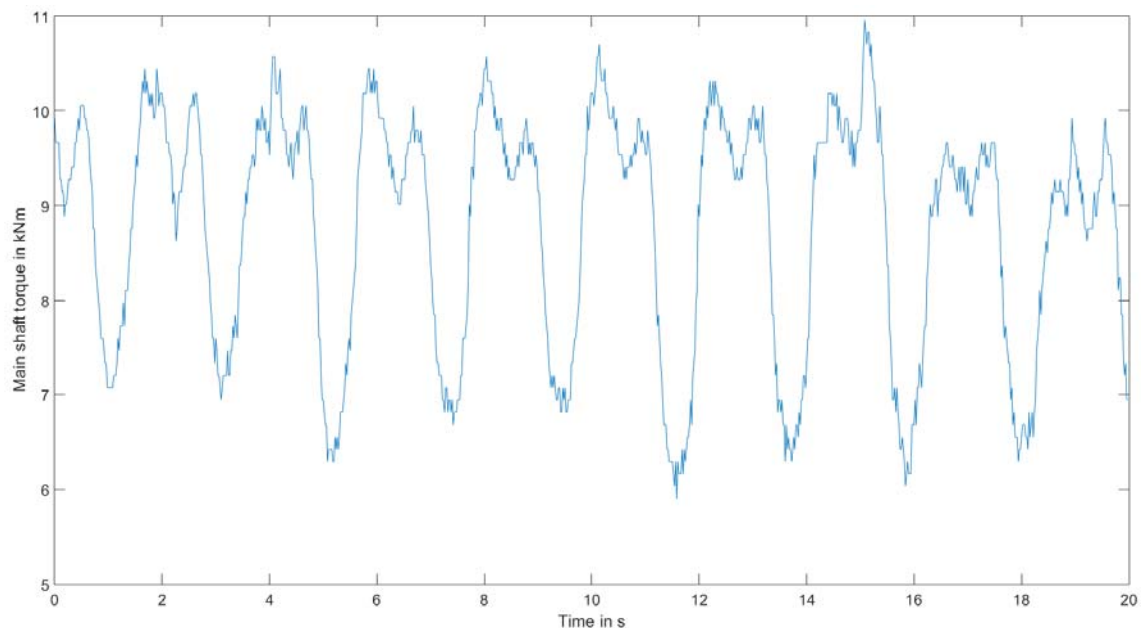


Figure 47: Time series of torque measurement in part load operation

The described shortcomings of the setup are affecting the analysis of torque measurements in the frequency domain. This analysis is needed to evaluate whether it can be replaced by a rotational speed measurement as described in the chapter above. The shortcomings cause disturbances at relatively low frequencies (below 1 Hz). Hence, it should be possible to compare the higher frequencies, which are also more relevant for the evaluation of most of the Eigenfrequencies of the drive train.

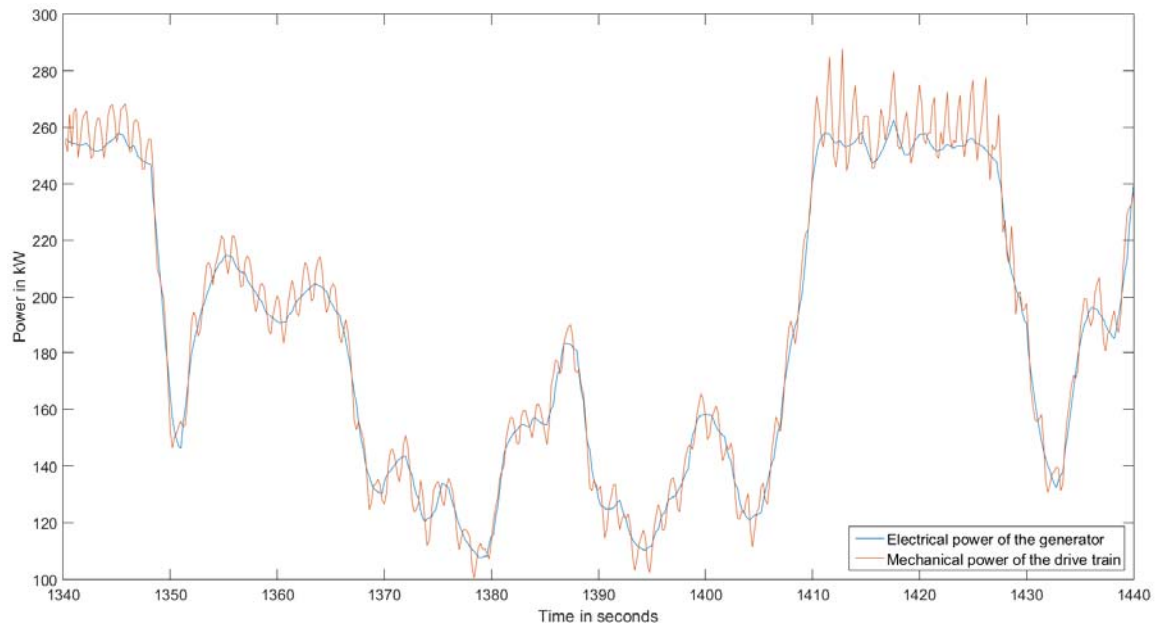


Figure 48: Comparison of the measured electrical power of the generator and the mechanical power of the drive train calculated from the measurements of torque and rotational speed

Pitch Angle Measurement

The pitch angle of the rotor blades are an essential bit of information that is needed for several purposes in this project. Since the pitch angle is a signal which is not relevant for monitoring the long term operation of a wind turbine e.g. by the owner of a wind turbine, it is not made available by the Enercon SCADA system. Hence, measuring the pitch angle was part of this project.

The obvious solution for such a measurement task might be to use the signals that origin from the pitch angle sensors which are already installed in the wind turbine. However, tapping the pitch angle signal of the wind turbine control system is not advisable, as the pitch control is highly safety critical for the wind turbine. Hence, such interference is to be avoided, and the pitch angle has to be measured with an add-on measurement system that under no condition causes disturbance for the wind turbine control system.

Since the rotor of a wind turbine is permanently rotating during operation, there are two main problems that need to be solved when attempting to measure the pitch angle with a sensor that is located in the hub: i) there needs to be a power supply that keeps the sensor running; ii) the measured signal needs to be routed from the spinning rotor to the stationary nacelle.

It is favourable to avoid a system that on the one hand interferes with the control system of the wind turbine and that on the other hand needs a complex infrastructure like its own battery or power generator and wireless signal routing. All these problems can be circumvented if a sensory system is installed at the nacelle, and if this sensory system measures the pitch angle of the blades from a distance.

The concept, the derivation and the design of the pitch angle measurement system that is developed in this project has been published in detail [8]. Hence, in this report the system is described and its components are introduced only very briefly. Operational experiences with this system are also summarised.

The pitch angle measurement concept that has been found to be most suitable as an add-on measurement system is a system that derives the pitch angle of a rotor blade from a measured distance. This measurement system has three main components: an angle indicator, a distance laser sensor and a data processing unit. These components, as well as their arrangement in a wind turbine, are shown in Figure 49. Photographs of some of these components are shown in the following figures. The angle indicator is attached to the root of the rotor blade, see Figure 52. The distance laser sensor (Figure 52 and Figure 53) is installed on the front end of the nacelle, just behind the rotor, such that it measures the distance to the angle indicator whenever a blade passes by. The data processing unit is located in a switch cabinet of the measurement system in the nacelle (Figure 13). Its task is to process the data from the distance laser sensor and to derive the pitch angle value from the measured distance value.

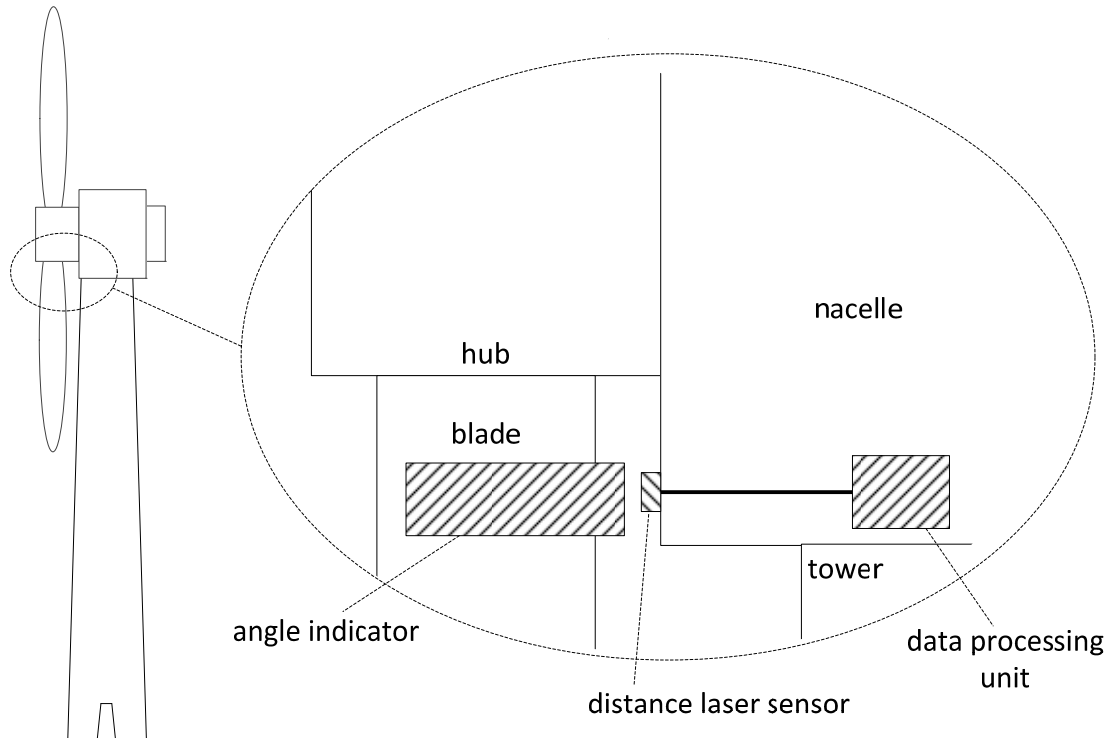


Figure 49: Sketch of the principal setup of the pitch angle measurement system.

The basic idea of the pitch angle measurement system is that the pitch angle of a blade is measured whenever it passes the stationary distance laser sensor, see Figure 52.

If the blade is turned around its longitudinal axis, the angle indicator exhibits more or less thickness in the direction of the distance laser sensor. I.e. for every pitch angle there is a unique thickness of the angle indicator.

When the rotor rotates, the blades with their angle indicators pass by the distance laser sensor. Due to the variable thickness of the angle indicator the distance that the distance laser sensor measures is variable, too. I.e. for every particular pitch angle of the blade there is a unique minimum distance between the distance laser sensor and the angle indicator. Figure 50 illustrates the concept for the smallest and the largest pitch angle with the largest and the smallest distance, respectively.

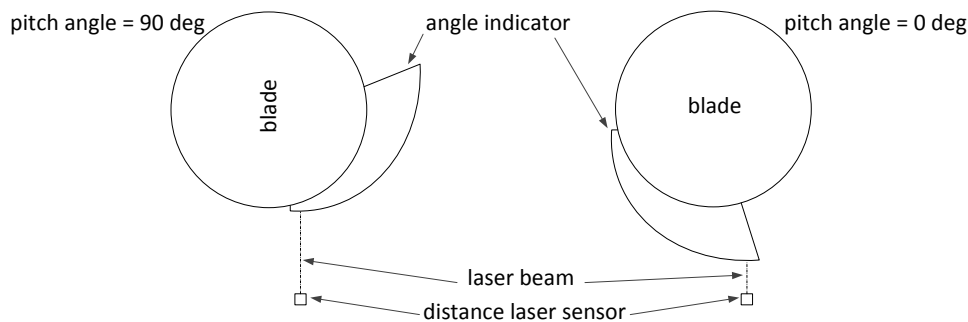


Figure 50: The distance measured by the distance laser sensor is a function of the pitch angle.

The angle indicators are made of polystyrene foam coated with glass fibre reinforced epoxy. The shape is designed such that the inner surface fits the blade root, while the outer surface is an Archimedean spiral. Figure 51 shows the 3-D plot of the angle indicator as it was milled out of a block of polystyrene foam. Also shown in Figure 51 is the plot of an Archimedean spiral.

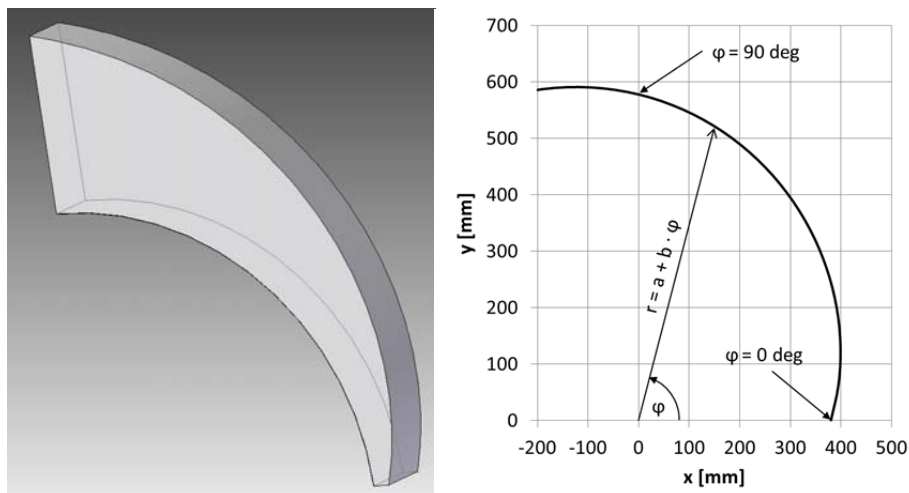


Figure 51: The angle indicator. Left: 3-D plot. Right: Archimedean spiral

An Archimedean spiral linearly increases its radius with the angle, as shown in Equation 6 and as plotted in Figure 51.

$$r = a + b \cdot \varphi$$

Equation 6

To avoid safety risks the angle indicators have to be lightweight components. They must neither pose a noticeable mechanical load for the surface of the rotor blades, nor must they be dangerous for people or animals under the wind turbine in case an angle indicator

unintentionally falls off its blade root. Hence, the weight of one angle indicator is about 750 g. The angle indicators are glued to the blade roots and secured with tensioning ropes.

The orientation of the angle indicators is such that the thick end points towards the distance laser sensor when the pitch angle is ≈ 0 deg, as illustrated in Figure 50. In this case the distance laser sensor measures a small distance. Typical for laser sensors is that their accuracy is higher at the minimum measurable distance, as opposed to worse accuracy at the upper range value. Accurate measurements are desired most when the turbine is in grid connected operation, as opposed to when the turbine is stopped and the blades are in feather position (pitch angle ≈ 90 deg, the thin end of the angle indicator points towards the distance laser sensor).

The distance laser sensor has to measure the distance to the angle indicator when it passes the sensor. Since this distance signal is the basis for the calculation of the pitch angle, it is crucial that this measuring happens reliably. If the distance laser sensor does not manage to measure a plausible minimum distance to the angle indicator while the blade passes, it takes a full revolution of the rotor before a new attempt can be undertaken to measure the pitch angle of this particular blade. Hence, the distance laser sensor has to work reliably. This means that it has to be resistant against extreme temperatures, a wide range of ambient light conditions, humidity in the air and even rain water.

Some of the environmental impacts can be mitigated by carefully locating the sensor, so that it is not likely to be exposed to direct sunlight or running water in front of its lens. As can be seen in Figure 52 the distance laser sensor is located below the rotor. Also, there is an oval plastic shelter around the sensor to prevent direct environmental impacts, see Figure 53.

When all potential environmental disturbances are prevented, the sensor has to produce a sensible distance signal that allows the data processing unit to calculate the pitch angle.

The rotor blade, whose pitch angle is to be measured, is not stationary in front of the distance laser sensor, instead it moves. Hence, the time available for carrying out the distance measurement is limited. Depending on the speed, with which the blade passes in front of the sensor, the sampling rate of the distance laser sensor, i.e. the number of measurements per second, has to be chosen. A detailed discussion on the boundary conditions and the resulting attributes, which the sensor has to feature is contained in [8]. The data sheet of the chosen distance laser sensor is contained in Appendix A.



Figure 52: Pitch angle sensor: laser sensor for distance measurement and angle indicator



Figure 53: Pitch angle sensor: detailed view of laser sensor for distance measurement

The distance laser sensor outputs a distance signal a certain number of times per second. Figure 54 shows a time series of the distance signal when an angle indicator passes the distance laser sensor. These measurements need to be evaluated and transformed into pitch angle values.

Since the pitch angle of a blade can only be determined once during a revolution of the rotor, i.e. when the blade is in front of the distance laser sensor, not every measured distance value leads to a pitch angle. In fact, most of the measurements need to be discarded as they do not relate to anything. Also shown in Figure 54 is the maximum measurement range of the distance laser sensor. When there is no object in front of the sensor it obviously outputs an out-of-range signal.

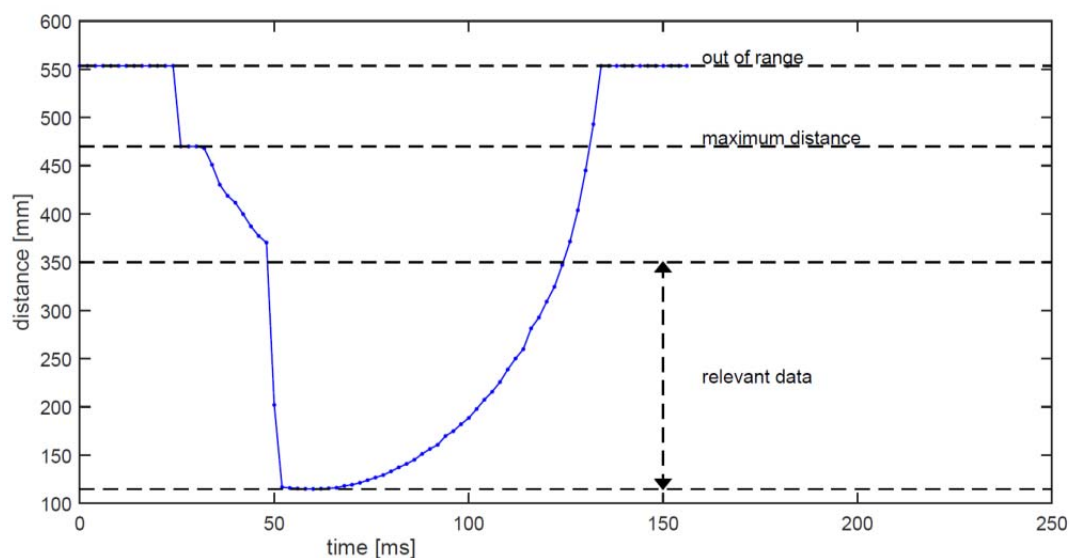


Figure 54: Measured time series of distance signal of an angle indicator passing the laser sensor

The sequence in which the data processing unit derives a pitch angle from the distance signals of the distance laser sensor is shown in Figure 55. The primary task of this data processing is to identify the minimum distance, and to discard obviously unrealistic spikes. Spikes are identified by the slope of the signal, i.e. by the difference between two subsequent distance measurements. Since the shape of the angle indicator is known, it is also known that the minimum distance has to be in the area where the slope of the surface of the angle indicator is around zero.

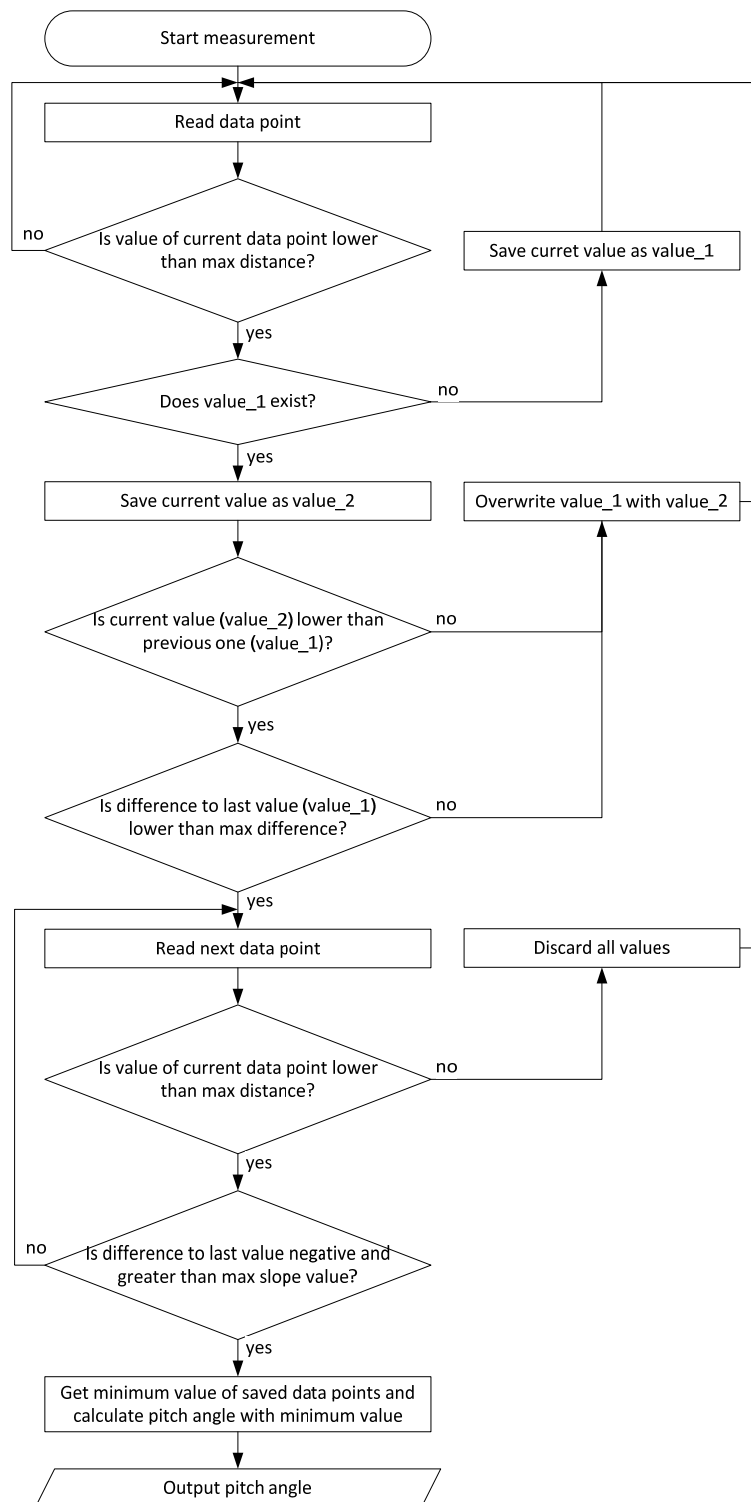


Figure 55: Flow chart of the data processing which derives a pitch angle value from the measured distance values.

Unusable distance measurements must not lead to wrong pitch angle values. Figure 56 shows an example where one faulty distance measurements leads to two minima in the distance while the angle indicator passes the distance laser sensor. The data processing unit identifies the correct minimum distance with help of the slope of the signal, see Figure 55.

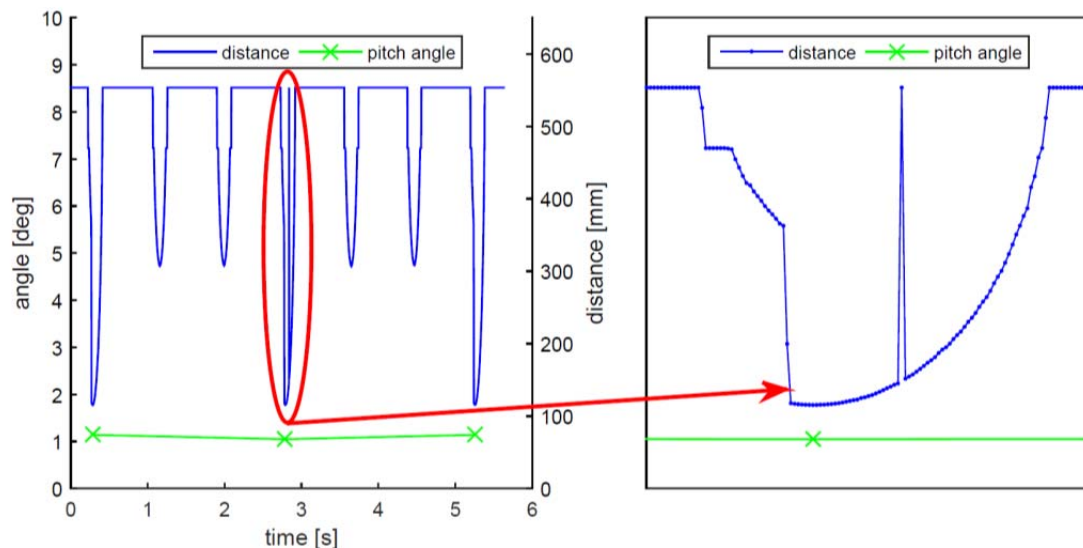


Figure 56: Left: distance measurement and calculated pitch angle. Right: zoom of disturbed distance measurement at angle indicator.

Once the correct minimum distance is determined, the data processing unit then derives a pitch angle value in degree from the measured minimum distance in mm. The Archimedean spiral of the angle indicator provides a linear relation between distance and pitch angle. Although the design of the angle indicator is known, a calibration needs to be performed to get the accurate parameters of this linear relation. On the one hand the production of the angle indicator is subject to finite accuracy. On the other hand the exact dimensions of the blade root, to which the angle indicator is attached, are relatively unknown. It can neither be assumed that the surface of the blade root is perfectly circular, nor can it be assumed that it is coaxial with the pitch axis. Therefore, the relation between distance and pitch angle is calibrated for different pitch angles.

The control system of the E30 allows manually setting the pitch angle and reading the measured pitch angle from a display in the control cabinet in the tower bottom. Figure 57 shows the time trace of the calibration run. The plotted pitch angles are the manually set values. The rotor speed is shown for reference. Since the rotor speed is always far away from its rated value of 50 RPM, the assumption is justified that the manually set pitch angles are kept unchanged by the control system of the E30.

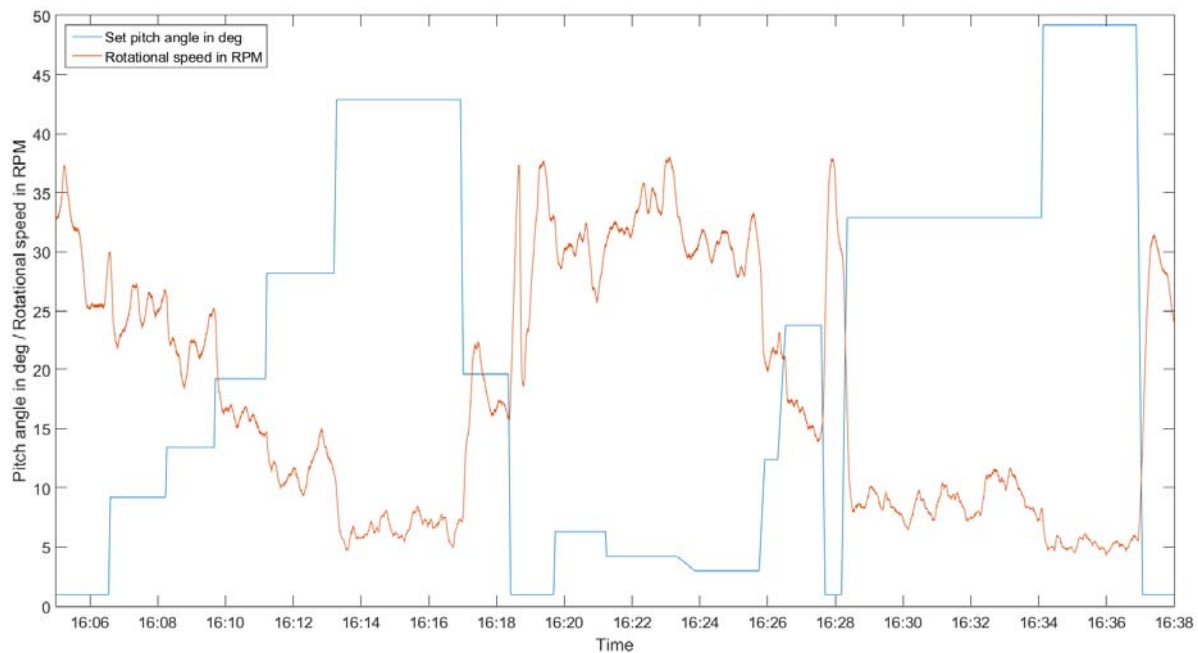


Figure 57: Time series of signals during the pitch angle calibration process.

For each period in which the pitch angle is kept constant (in Figure 57) the signal from the distance laser sensor is recorded. Figure 58 shows the example of the distance laser sensor signal for a manually set pitch angle of 1 deg.

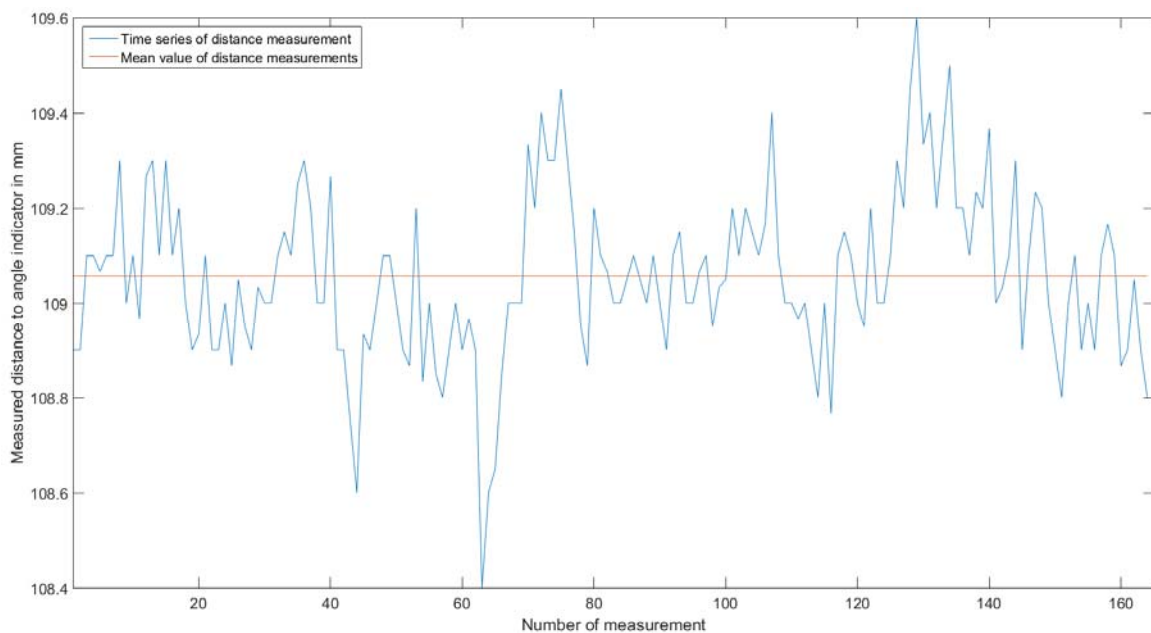


Figure 58: Variations of the measured distance to the angle indicator for a constant pitch angle.

Each time the angle indicator passes the distance laser sensor, a distance measurement is recorded. All measurements are averaged and allocated to the manually set pitch angle in degree. This method is applied for all the different manually set pitch angles in Figure 57. Figure 59 shows the resulting linear function that translates the measured distance to pitch angle. This linear function is implemented in the data processing unit, where it is extrapolated to also measure pitch angles up to feather position.

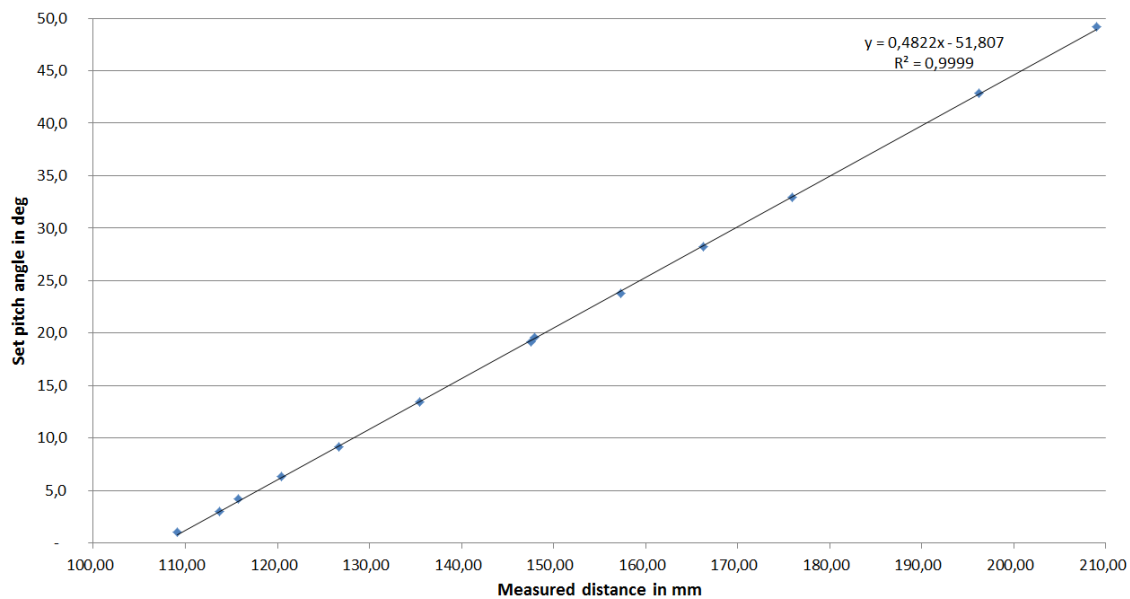


Figure 59: Relation between averaged measured distances to the angle indicator and pitch angles.

When the E30 wind turbine runs in part load operation the pitch angle is kept constant by the wind turbine controller, provided that the wind speed does not vary too much and that the speed gradient is not too steep. Hence, by carefully selecting a period of part load operation, it can be assumed that the pitch angle is constant. Such a period is used for evaluating the accumulated error that occurs in the measuring of the pitch angle.

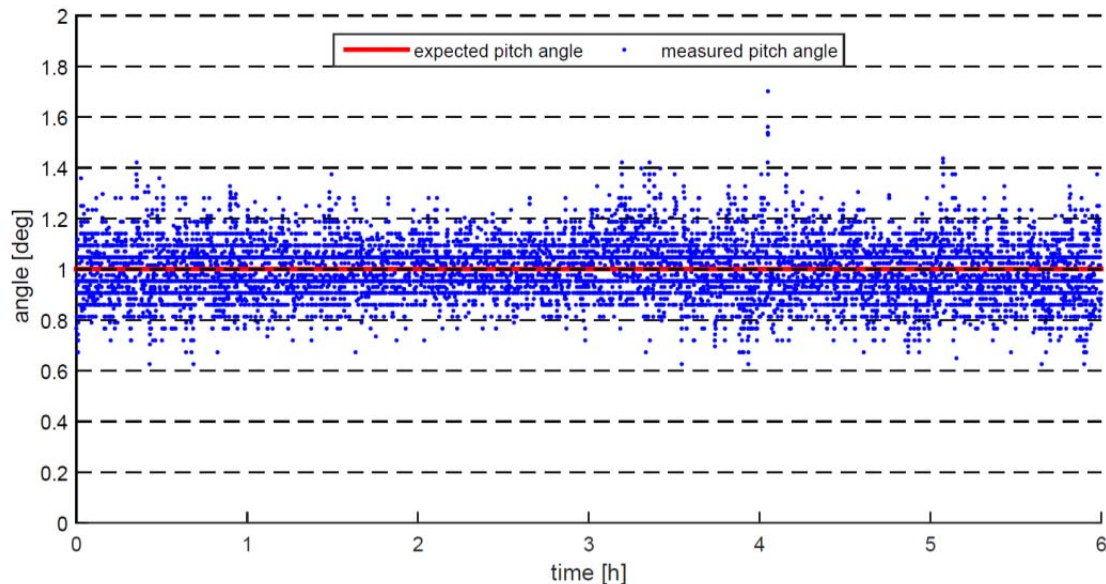


Figure 60: Stationary pitch angle measured by the pitch angle sensor. Variations in the signal are the sum of the measurement error and the pitch positioning error.

Figure 60 shows a 6 hour period of low part load operation. Light, relatively constant wind leads to operation where the pitch angle is expected to be kept at a constant 1 deg. Figure 60 shows that the measured pitch angle value generally varies in a band of about ± 0.2 deg. Less frequently there are pitch values that are in the range of ± 0.4 deg. Only very rarely there are outliers that are wrong by more than 0.4 deg. This variance of the pitch angle signal is an indicator for the accuracy of the measurement methodology. However, contained in this accuracy are also tolerances in the pitch positioning system. In the operating point shown in Figure 60 it is assumed that the wind turbine controller does not attempt to change the pitch angle. This, however, does not necessarily mean that the pitch angle does not vary by backlash in the pitch drive system and play in the pitch bearing. Such unintended pitch angle movements might not even be sensed by the wind turbine control system, as also the pitch angle sensors in the hub have a limited accuracy. In addition, the assumption that the pitch angle is not varied by the wind turbine controller, might be wrong in some instances. Hence, the accuracy evaluation done here is conservative.

As stated above the pitch angle of one particular blade is determined once every revolution of the rotor. This is shown in Figure 61, where the pitch angle of blade A is measured whenever the angle indicator of blade A is in front of the distance laser sensor. In order to identify the individual angle indicators the rotor position has to be known. For this purpose the spike in the

speed signal, as discussed in section Rotational Speed Measurement is utilised. This spike provides an accurate indication of the rotor position once every revolution. By integrating the speed signal over time the angular position of the rotor is calculated continuously. With knowledge of the rotor position the measured minimum distance of the distance laser sensor can be allocated one particular blade.

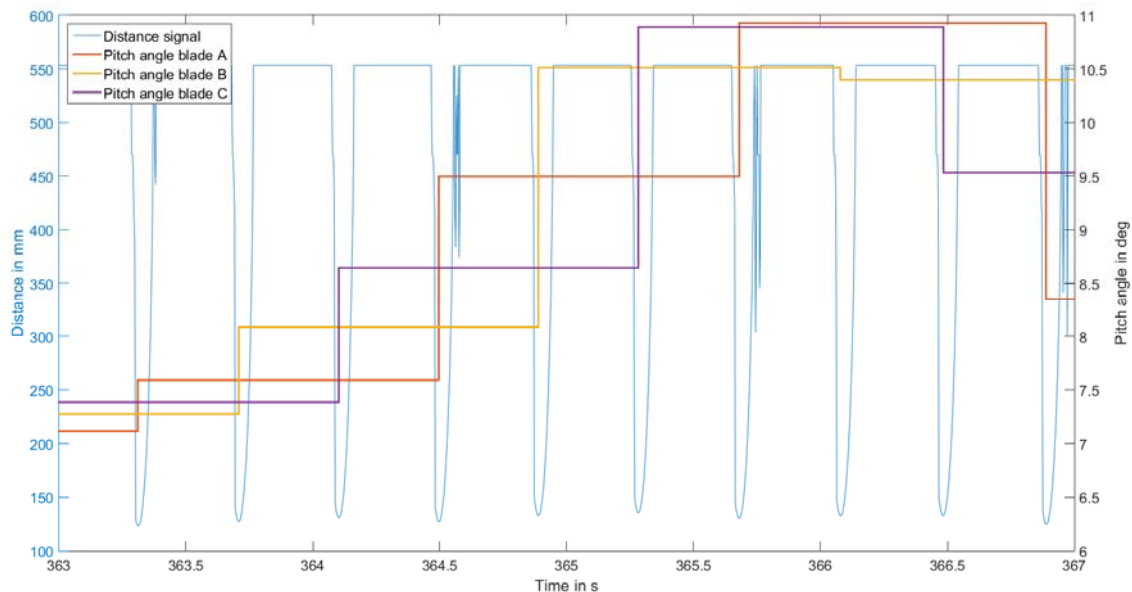


Figure 61: Distance signal and calculated pitch angle of one blade.

Since the pitch angle measurement is a distance measurement where a laser beam is sent through ambient air it is obvious that ambient conditions might have an effect on the accuracy of the measurement. Figure 62 shows the calculated pitch angle over a period of three days from 17 May to 20 May 2014 in which the rotor speed of the E30 (also shown in Figure 62) never reached its rated value. Hence, it is assumed that the pitch angle is kept at a constant 1 deg.

Figure 62 reveals that the calculated pitch angle varies with the time of the day. The ambient light has an effect on the measured distance, which is why during the day the pitch angle is perceived smaller than during the night.

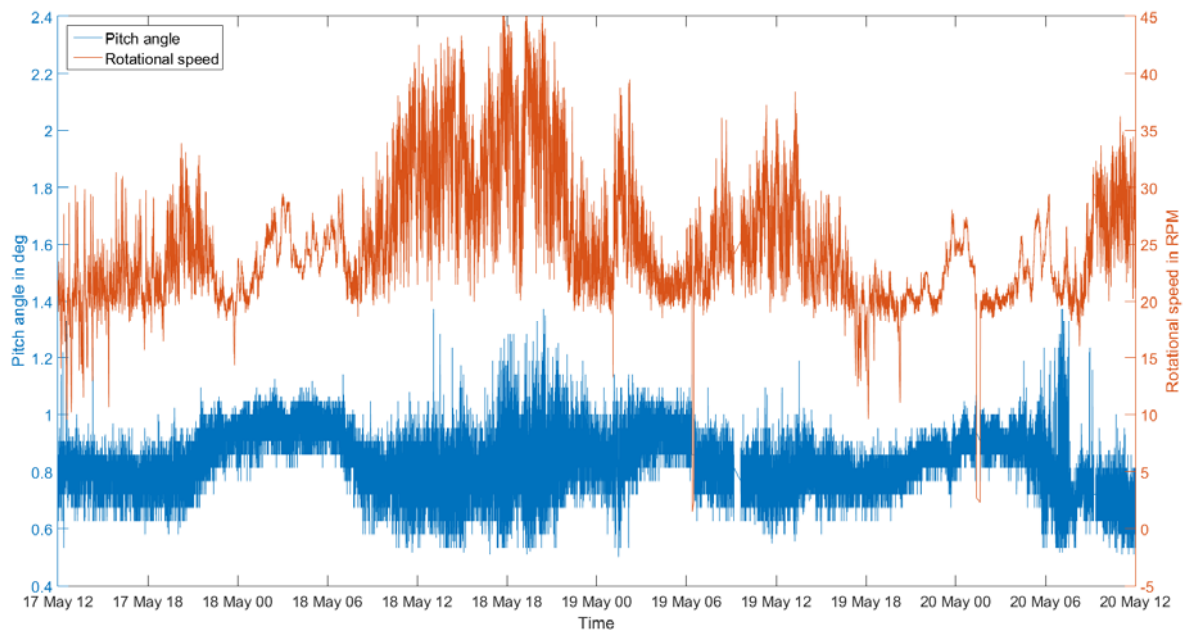


Figure 62: Measured pitch angle of one blade and the measured rotational speed of the rotor over a period of three days.

Figure 63 shows a fraction of Figure 62 (24 hours from 17 May to 18 May 2014). It can be seen that the speed is always in the lower part load range. I.e. pitch angle variations are not to be expected. Yet the measured pitch angle varies by about 0.2 deg between day and night. This further confirmed by the histogram of the measured pitch angle values of this interval, which is shown in Figure 64. The highest density occurs in the bins 0.75 to 0.8 deg (daytime) and 0.95 to 1.0 deg (night time). It is assumed that the observed variations are caused by the difference in ambient light.

Figure 62 and Figure 63 further reveal that the measured pitch angle tends to exhibit larger deviations the higher the rotational speed of the rotor is. Also the deviations appear to be generally larger during day light than during the night.

With increasing rotational speed, the distance between the measurement points on the surface of the passing angle indicator increases, as the distance laser sensor has a maximum frequency with which measurements are repeated. If a distance measurement has to be discarded, the angle indicator has moved before the next measurement can be conducted. This effect leads to measurement errors that increase with the rotational speed.

The light intensity variations during daylight are larger than during the night. Between sunrise and sunset the light intensity can range from dark clouds (almost as twilight) to direct sunlight.

Hence, the variations in the pitch measurement observed between day and night can occur almost as intense during the day when the light intensity changes due to clouds.

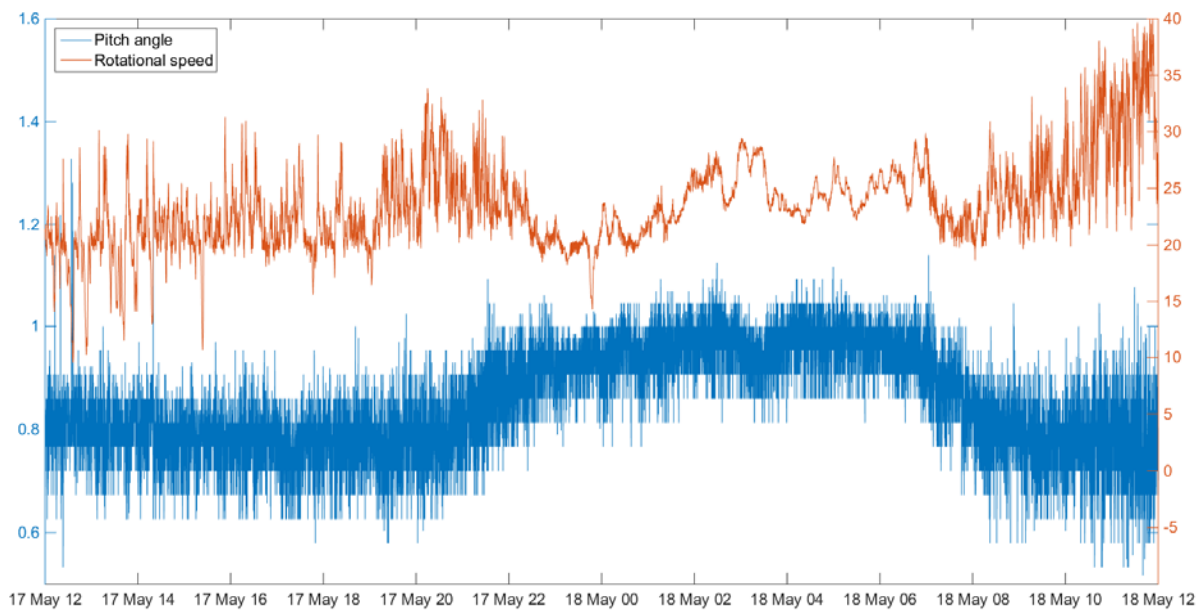


Figure 63: Extract of Figure 62. Measured pitch angle of one blade and the measured rotational speed of the rotor.

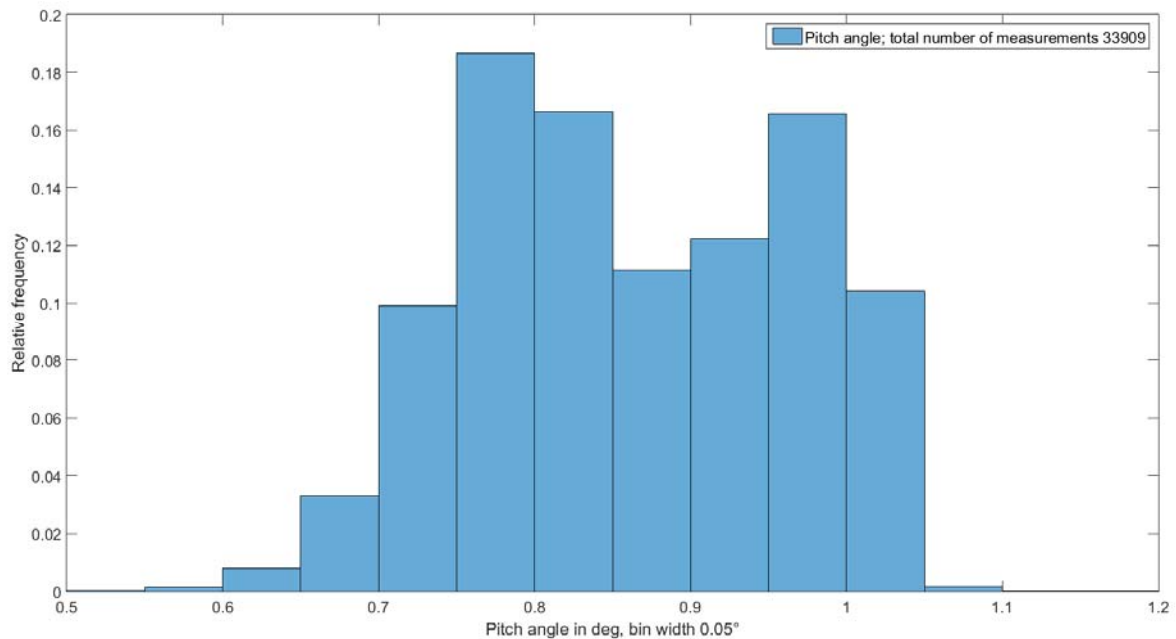


Figure 64: Histogram of pitch angle measurements for 17 May 2015, 12:00 to 18 May 2015, 12:00

The effect of humidity in the air is assumed to have a noticeable effect on the pitch angle measurement, too. This has not been analysed so far. The pitch angle time traces that have been used in this project have not been disrupted to the extent that they were unusable. Hence, it is concluded that the pitch angle measurement system works reliable under a wide range of climatic conditions. The effect of humidity rain, snow and hail has to be analysed in detail in future.

Development of the Simulation Model

Wind Model

The purpose of the wind model is to create a realistic time signal for the wind, which takes the different wind speed over the rotor plane into account. In particular the vertical wind shear has to be described by the wind signal as the aerodynamic is modelled by c_p and c_t look-up tables with only one input for the wind. The wind model is taken from Jauch [1]. The model was originally designed for wind farm simulation. Hence, only the part of the model is needed, which addresses the wind turbine itself (see Figure 65). The model uses a slowly changing wind signal as input signal, which represents gusts. Realistic turbulences are created by the combination of white noise generators, Kaimal filter and Admittance filter. In this project measurements from the 50 m US anemometer of the met mast are used as input signal. The original data are recorded with 10 Hz. These data have to be modified by a low pass filter in order to remove wind speed changes with high frequencies, as these are generated by the wind model.

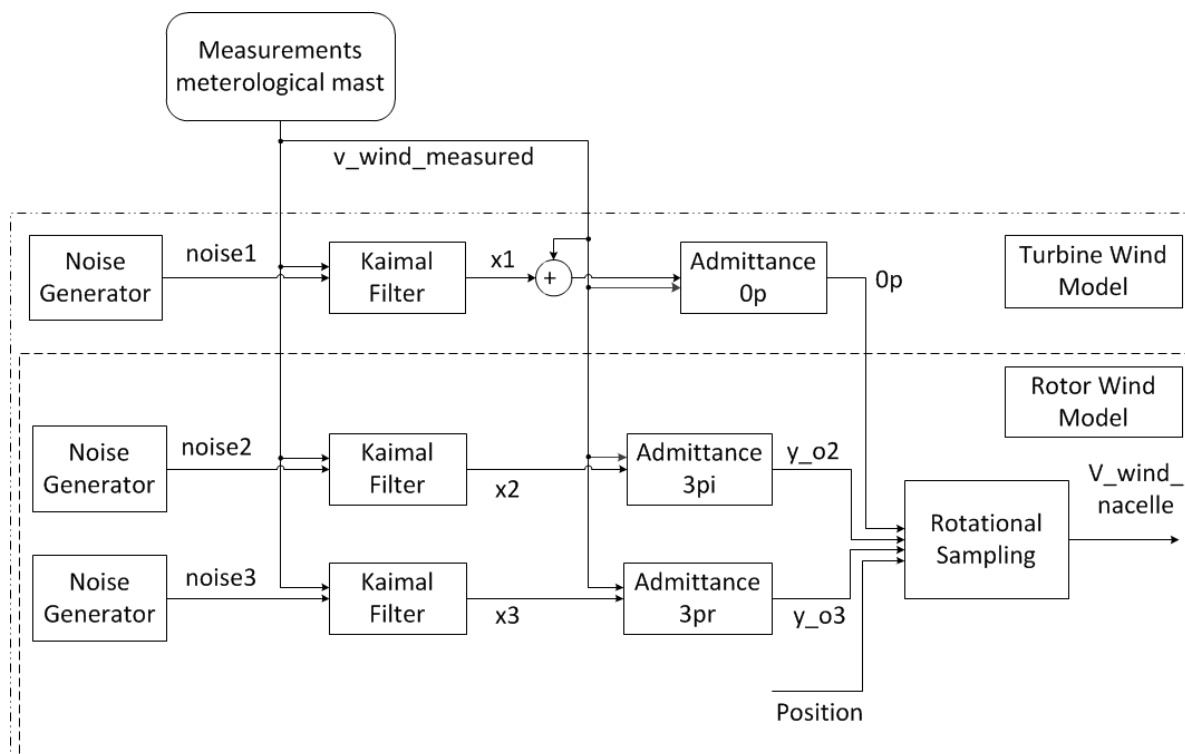


Figure 65: Block diagram of the wind model

The output signal of the model should include a realistic 3p-effect, which describes the vertical wind shear in the rotor plane seen by the three blades during one revolution. The effect can be validated by comparing the wind speed signals measured by the ultra-sonic anemometers at 50 m (hub height) and 35 m (lowest position of the blade tip) and is modelled as a sine function. This causes a slight deviation between the model and the reality as the increase in wind speed in the lower half of the rotor plane is stronger than in the upper half. The vertical wind shear can be calculated from long term measurements of the wind speed at the different anemometers (data averaged in 10 min intervals). Figure 66 shows the Weibull distribution of the three wind speed measurements at the different heights.

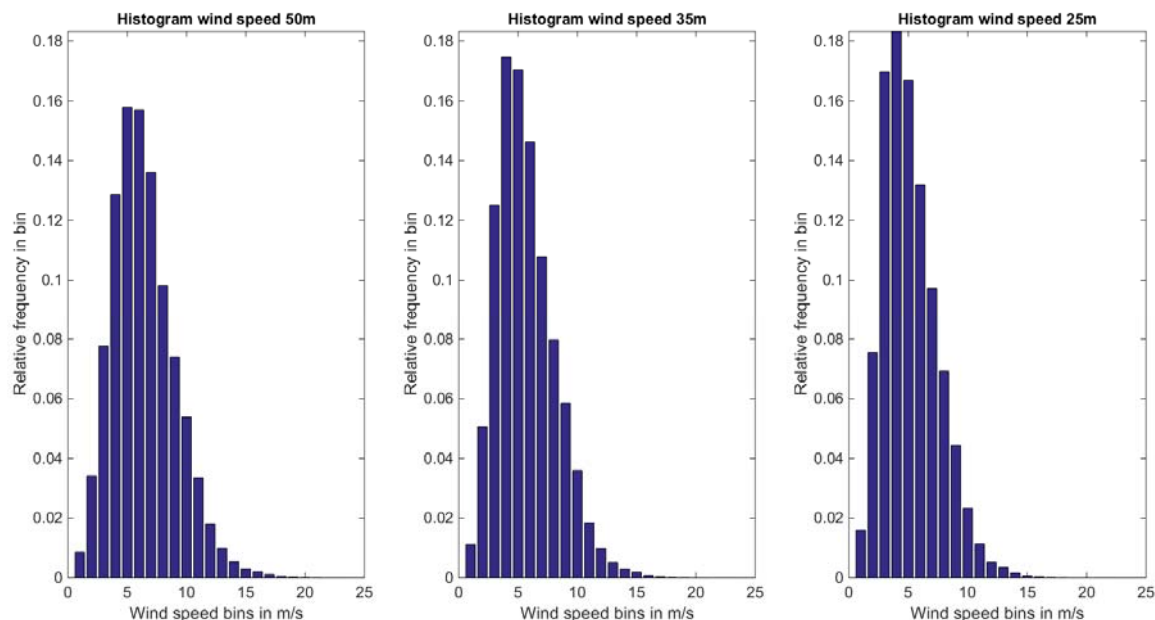


Figure 66: Weibull distribution of wind speed measurements (10-min averages)

The used data is recorded between August 2014 and August 2015. As expected the wind speed is strongly increasing with height. The magnitude of the vertical wind speed profile is described by the so called roughness length z_0 . It can be determined by fitting an exponential curve through the average values of the three wind speed measurements. The calculated value of 1.6 m is very high but not unrealistic for a site in a city. Hence, the height has a strong influence on the wind speed. This can be explained by the rough terrain, high buildings and the vegetation in the vicinity of the met mast and the wind turbine. All three factors create highly turbulent wind conditions with intense vertical fractions in the wind speed vectors.

Figure 67 shows the turbulence intensity for the three heights calculated with same data set as the vertical wind shear. It is calculated by dividing the standard deviation of the wind speed by the mean wind speed for 10-min-intervals using Equation 7 [9].

$$TI = \frac{\sigma_{v_{wind,10min}}}{\bar{v}_{wind,10min}} \quad \text{Equation 7}$$

Furthermore, the calculated values are classified in wind speed bins and the average turbulence intensity for each bin is determined. The highest turbulence intensity occurs during low wind speed. Furthermore, the turbulence intensity decreases with an increase in height. This can be explained by the weaker influence of the surface induced turbulences on the measurements.

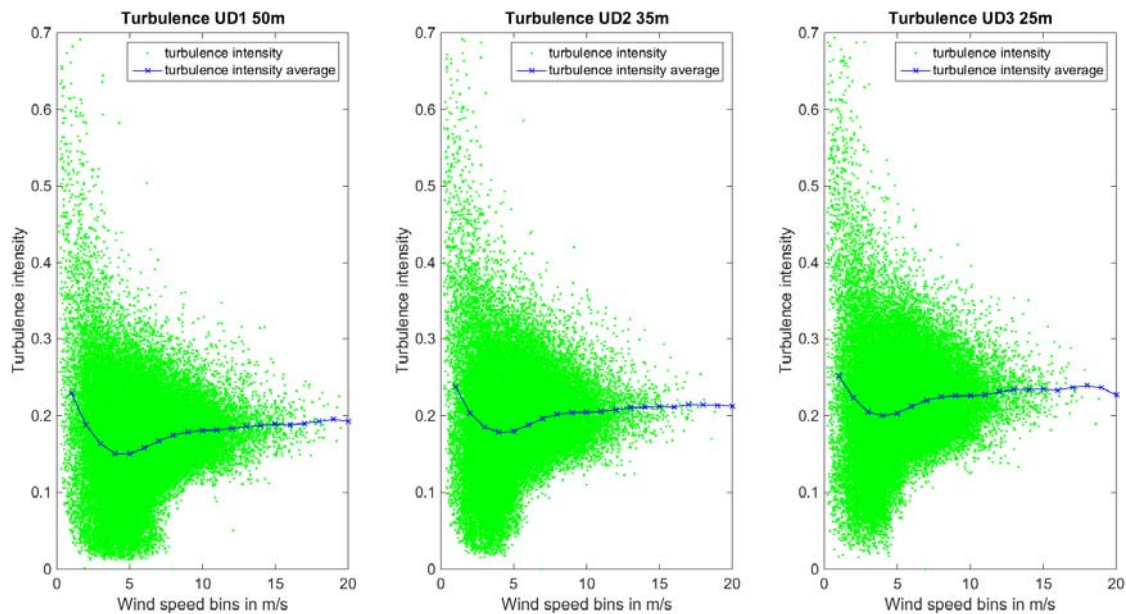


Figure 67: Comparison of the turbulence intensity of the three wind measurements

The turbulence intensity is also analysed with respect to the wind direction for the wind speed measurements at 50 m. In general, the turbulence intensity for westerly wind directions is slightly stronger than the one for easterly directions. This can be explained by a trough in the terrain to the west of the met mast. Similarly, northerly wind directions are more turbulent than southerly as most of the higher buildings and vegetation are north of the met mast. Figure 68 shows an analysis of the wind speed measurements for 30 deg wind direction bins. Besides, the described difference between north and south, the high turbulence intensity for the wind direction bin centred at 45 deg sticks out. This is caused by the induced turbulence from the wind turbine as the met mast is directly behind the turbine for this wind direction.

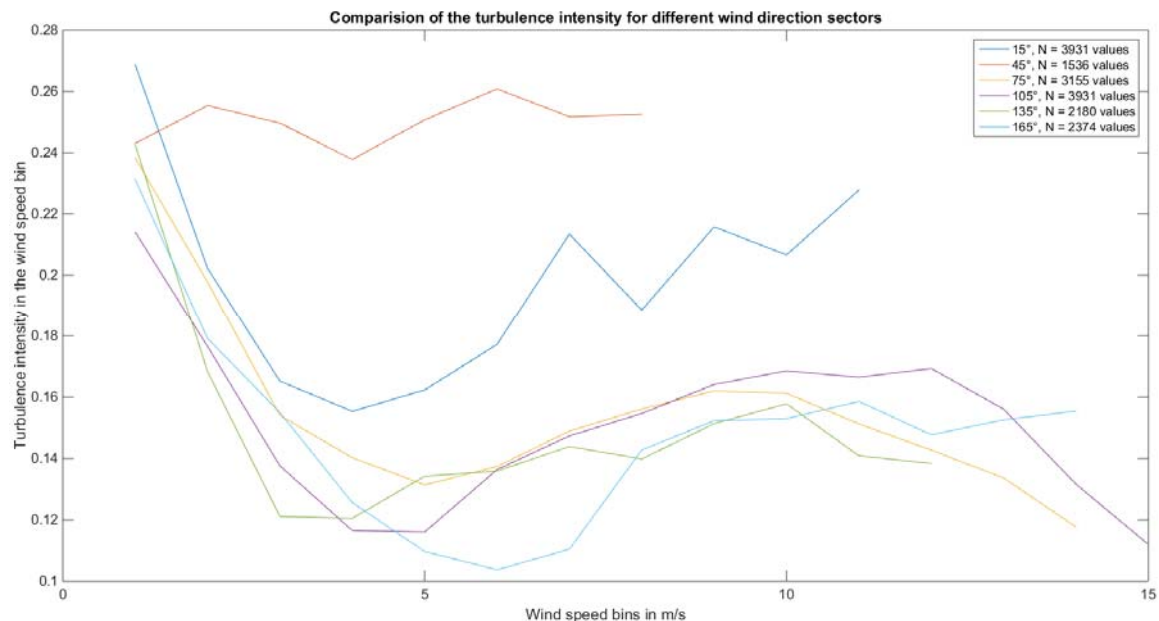


Figure 68: Turbulence intensity for easterly wind direction sectors for the measurement at 50 m

The data recorded between August 2014 and August 2015 are also used for a spectral analysis. The power density spectrum is calculated for the 10-min-average data of the wind speed measured at 50 m (see Figure 69). Diurnal and bi-diurnal effects are recognisable. Furthermore, slower variations with periods in the order of five to ten days are visible. These variations are caused by the passing of low pressure systems. The fluctuations with very high periods (several months) are showing the change of the wind speed over the year with higher wind speed in the winter and lower in the summer. These fluctuations can be analysed in greater detail once measurements over several years are available.

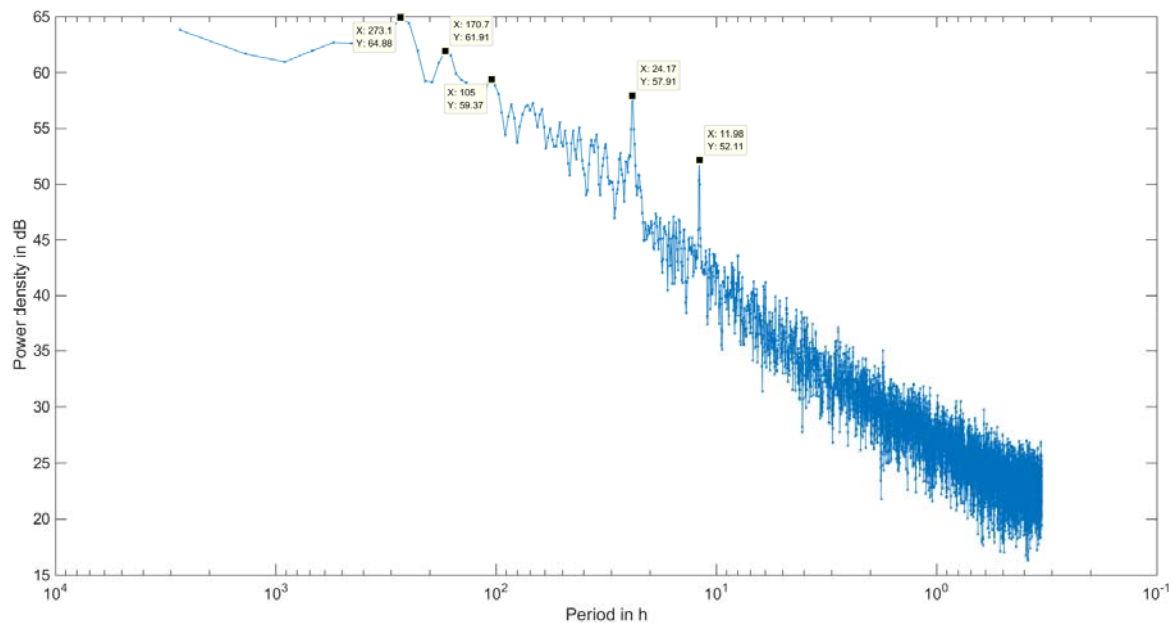


Figure 69: Spectral analysis of 10-min averaged values of the wind measurement at 50 m

In addition to the frequency analysis for a large time scale as described above, a frequency analysis of the turbulence is of interest. Figure 70 shows the power density spectrum of the wind speed measurements of all three anemometers. The analysis was performed with 12 hours data from December 2014. The wind speed changed between 6 m/s and 16 m/s during the analysed period. Up to one Hz and above three Hz the spectrum looks similar to spectrums which can be found in the literature [10]. By contrast, in between these values there are two humps which are not described in the literature. These humps look like side lobes from the Fourier transformation [5]. However, the humps are also present when a different window function with higher side lobe attenuation (i.e. Kaiser window with -100 dB attenuation) is used. Hence, these frequencies seem to be present in the measurements. However, as this part of the frequency spectrum is attenuated before the measured data are fed into the wind model, these frequencies are not analysed in detail. They will be analysed in the future during a comprehensive frequency analysis of the met mast data. Figure 70 also shows that there are no significant differences in the frequency spectra of the three sensors.

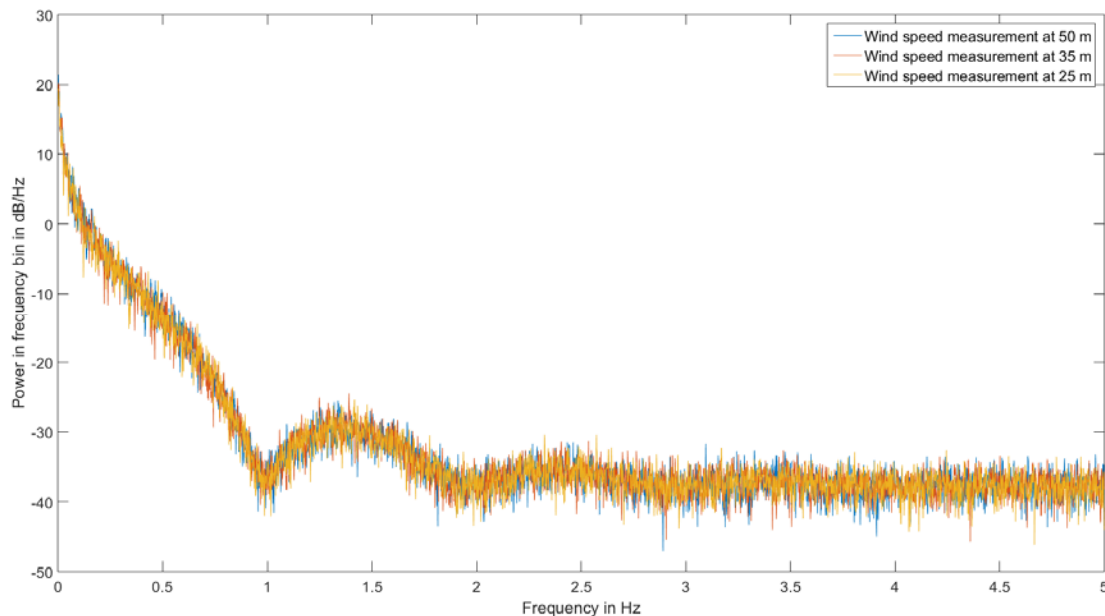


Figure 70: Spectral analysis of 10 Hz the wind measurement data at 50 m, 35 m, and 25 m

The frequency analysis above is used to tune the input parameter of the wind model. Figure 71 shows a comparison of the simulated wind signal and the measured wind signal for upper part load operation and full load operation. Both signals show a good agreement below 1 Hz and above 4 Hz. The intended simulation of the 3p-effect causes the hump in the frequency analysis of the simulated wind signal between 1 Hz and 3.5 Hz. The frequency of the 3p-effect depends on the rotor speed. In the shown simulation, the rotor speed was between 0.7 p.u. and 1.05 p.u. (0.6 Hz and 0.88 Hz). The magnitude of the effect is caused by the tuning of the model parameters with vertical wind shear in the time domain (see above). It has to be noted that the 3p-effect also overlay the humps in the measured frequency spectrum for most of the speed range. Hence, this unexplained part of the measured frequency spectrum is not important for most operational points. To sum, it can be concluded, that the wind model creates realistic time traces of the wind speed for the E30 site, which can be used for the intended simulations.

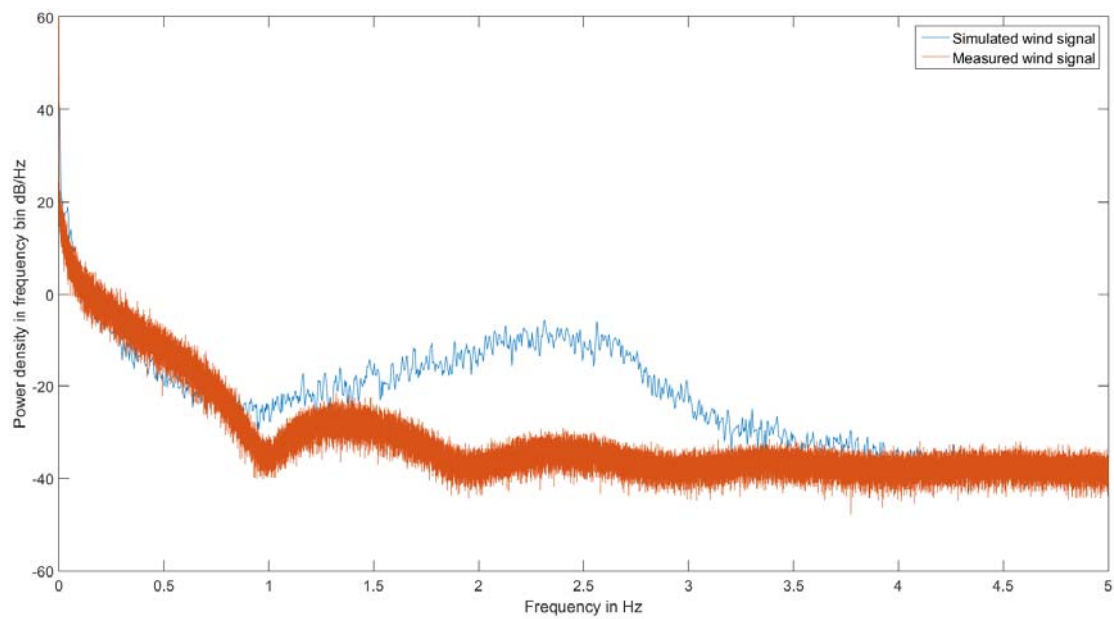


Figure 71: Comparison of the spectral analysis of simulated wind signal and the measured wind signal

Wind Turbine Model

The wind turbine is modelled in a Matlab/Simulink environment. The subsystems are coded in Matlab function, which are called from Simulink. The subsystems are connected in Simulink. The block diagram of the wind turbine model including the wind model is shown in Figure 72. The subsystems (green boxes in Figure 72) are described in the following chapters.

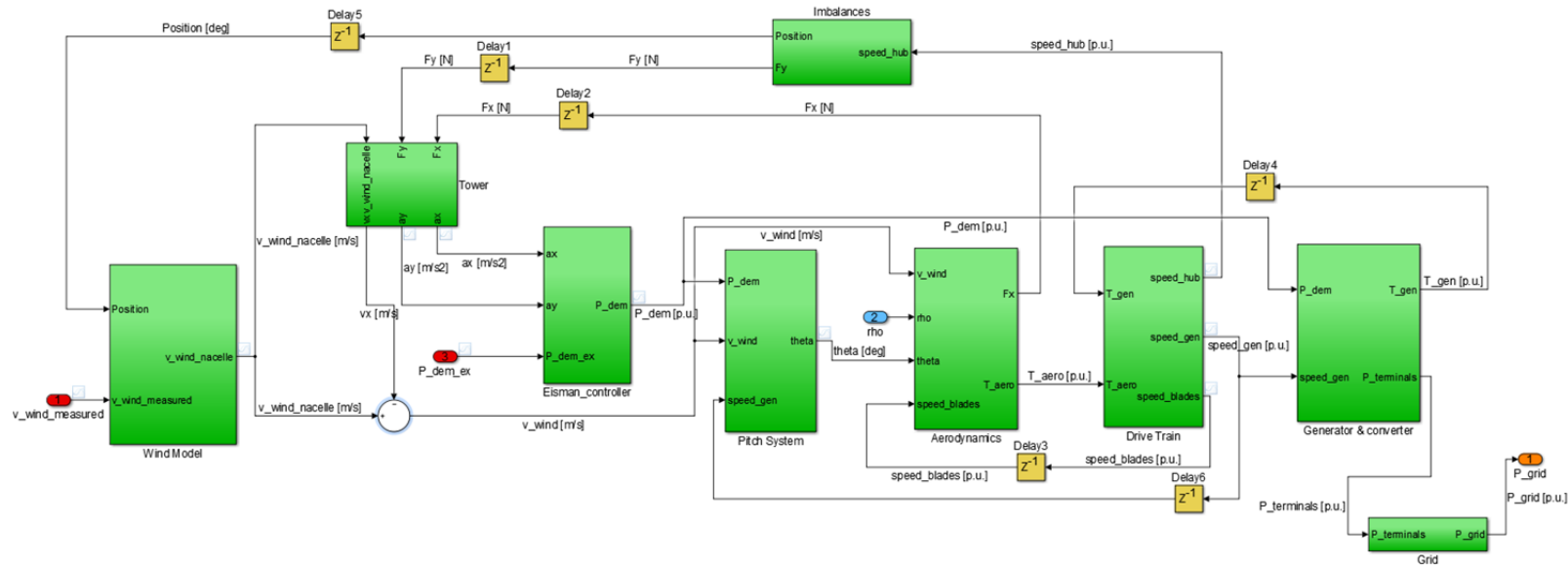


Figure 72: Block diagram of the simulation model

Aerodynamics of the Rotor

The aerodynamics of the rotor is modelled by means of the aerodynamic power coefficient, c_p , and the aerodynamic thrust coefficient, c_T (see Figure 73). These parameters are implemented in tables, where c_p and c_T are functions of the tip speed ratio, λ and the pitch angle, θ . More detailed models like a blade element method model would require further information on the geometry and the stiffness of the blades, which the manufacturer regards as confidential information. Hence, these models could not be used in this project. However, for the intended controller design the used models are accurate enough. Furthermore, a simple aerodynamics model is beneficial regarding computational time. It has to be noted, that the used power coefficients do not allow simulating a start from stand still. That would require determining the torque coefficient of the rotor, which is not possible with the available data. To avoid this problem a small, arbitrary value was used for the rotor torque when starting from standstill. Although this is not correct, it should not affect the simulation results as the simulation time step is very small and a power coefficient is computable once the turbine rotates even at a very slow speed.

The needed tables are created by using standard shapes from the literature. Measured values are used to adopt these shapes to the behaviour of the turbine.

C_p and c_T are usually derived for steady-state operation of the wind turbine. However, during normal operations the wind turbine will almost never be in a steady operation point due to the turbulent wind. Hence, all measurements will be taken during non-steady state operation. Averaged values were used to address this problem as described in the following sections.

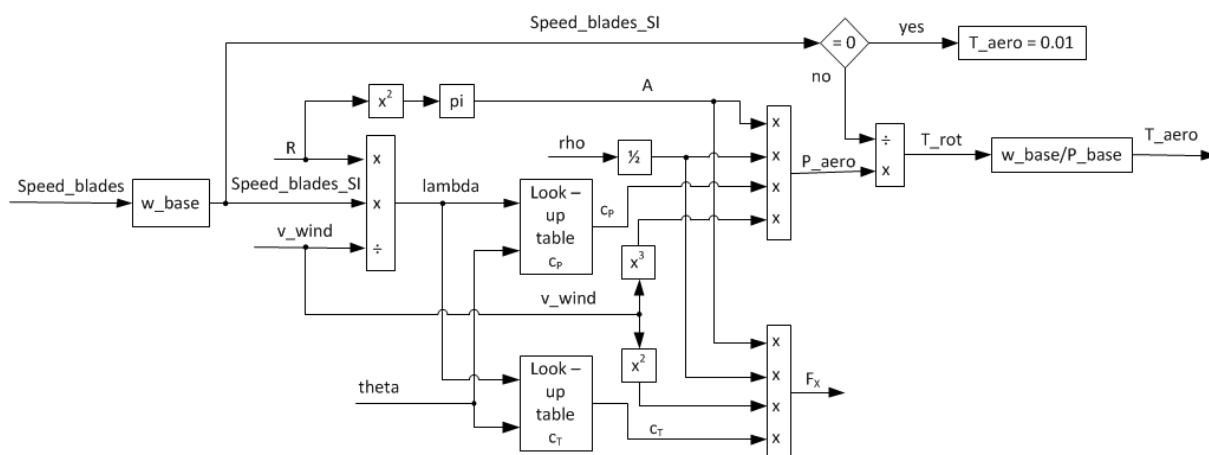


Figure 73: Block diagram of aerodynamic model

c_p Table:

The c_p -characteristic of the rotor is a function of the tip speed ratio and the pitch angle. Its general shape was taken from the literature [11]. As stated above averaged values are used to adopt the characteristic to the measurement.

For this purpose 10-min average data (drive train speed, wind speed, and grid power) from Enercon's customer interface were combined with the pitch angle measurement from the Dewetron. Furthermore, long term measurements with the Dewetron are used to estimate the generator power from the grid power. The mechanical losses in the drive train and losses of the generator are assumed to be 7 % (constant over the whole power range). The required air density is calculated using data from the metrological mast.

During the assessment of the data it becomes obvious, that using data with an averaged pitch angle greater than 1 deg (i.e. the minimum pitch angle) does not lead to reasonable results. This can be explained by the strong non-linear influence of the pitch angle on the aerodynamics, which makes the use of averaged data for the pitch angle unreasonable. Hence, data with varying pitch angles (i.e. full-load operation) has to be excluded from the analysis. Furthermore, data from 10-min intervals are excluded, during which the turbine is occasionally disconnected from the grid due to a lack of power in the wind. An analysis of these time series showed unreasonable low c_p -values, which can be explained by the averaging of the grid power within in the 10-min intervals.

For the analysis one year data (August 2014 to July 2015) is used. Excluding data as described in the paragraph above limits the data pool to approximately 22750 combinations of c_p and λ at a pitch angle of 1 deg. These values are used to adopt the c_p curve taken from the literature (see Figure 74). The results show good agreement between the measured and the used values, especially for the most important tip speed ratios between 7 and 8. As the nacelle anemometer is used for the wind speed measurements, the analysis contains some uncertainty. This uncertainty is reduced by the large amount of data used. However, any unknown systematic errors in the wind measurements cannot be accounted for.

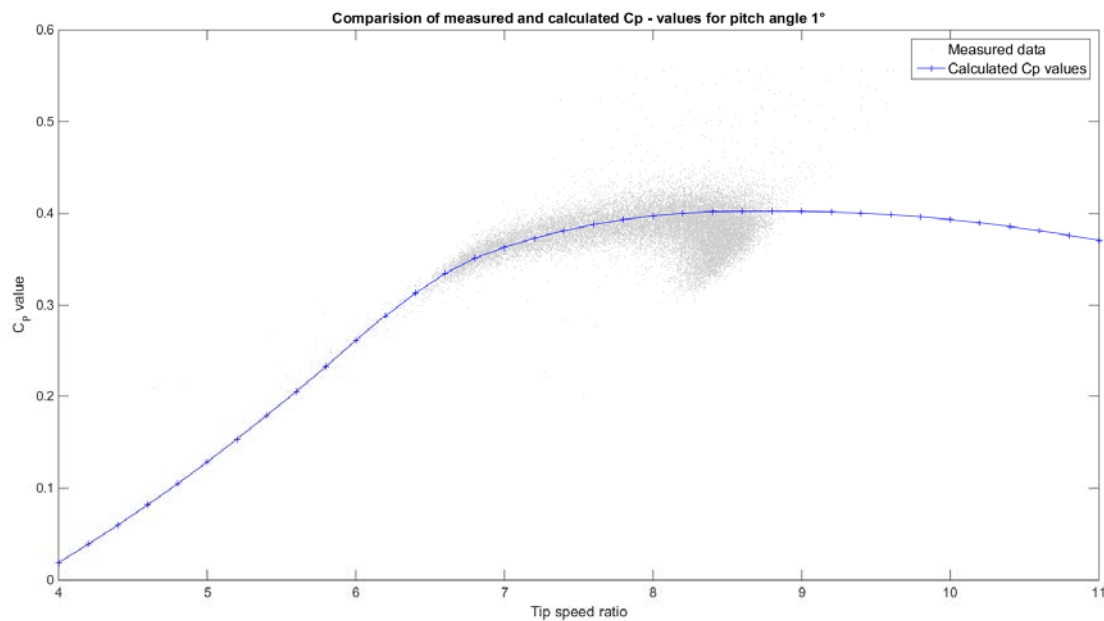


Figure 74: Comparison of measured and calculated C_p values for a pitch angle of one degree

Values for other pitch angles are analysed for time series, during which the pitch angle is manually set to values between 3deg and 8deg. The measurements show fairly good agreement. However, the analysis contains a higher uncertainty as for $\theta = 1\text{deg}$ as the analysed time series are short (several hours).

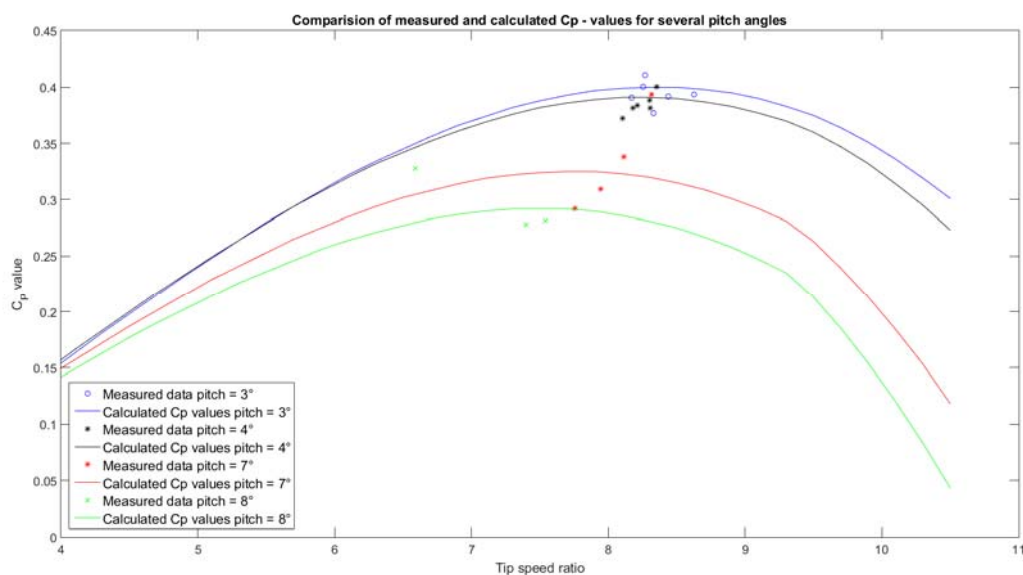


Figure 75: Comparison of measured and calculated C_p values for different pitch angles

Figure 76 shows a surface plot of the used power coefficient characteristic for the most important combinations of pitch angle and tip speed ratio.

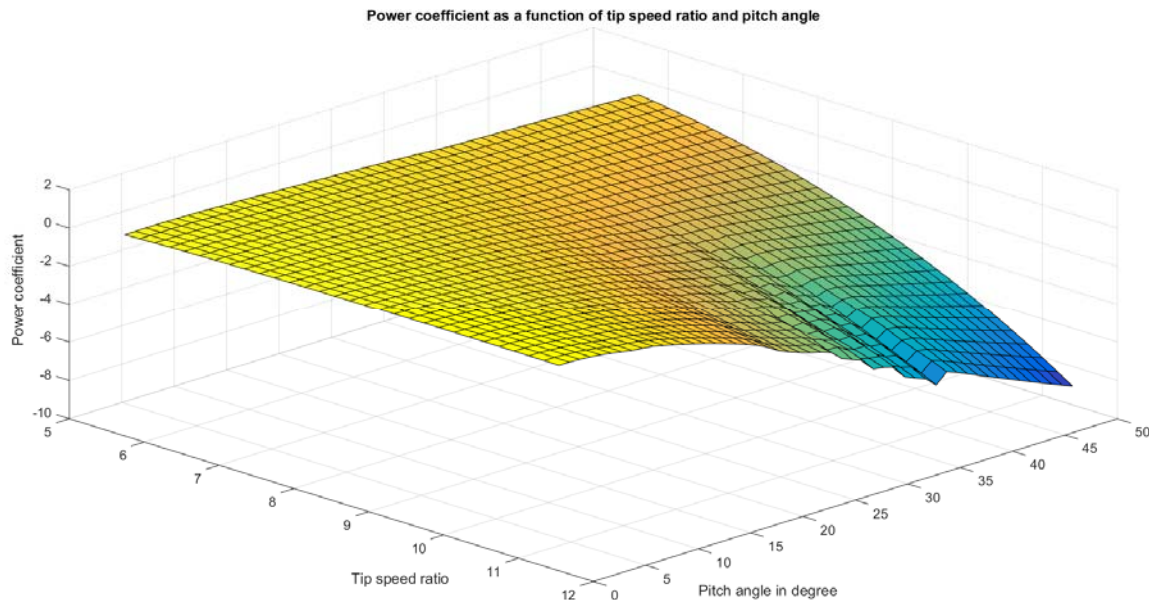


Figure 76: Surface plot of the power coefficient as a function of tip speed ratio and pitch

C_T Table:

The c_T -characteristic of the rotor is also a function of the tip speed ratio and the pitch angle. As these characteristics are disclosed information, it has to be derived from measurements and commonly used values in the literature.

As a first step the shape of the c_T -characteristic of the NREL 5 MW reference turbine [11] is used. These curves are shifted according to measurements at the E30. The measured data are acquired by conducting several emergency stops with the turbine (see Figure 77). The thrust force can be derived by comparing the nacelle position directly before the emergency stop and after the end of the tower oscillations.

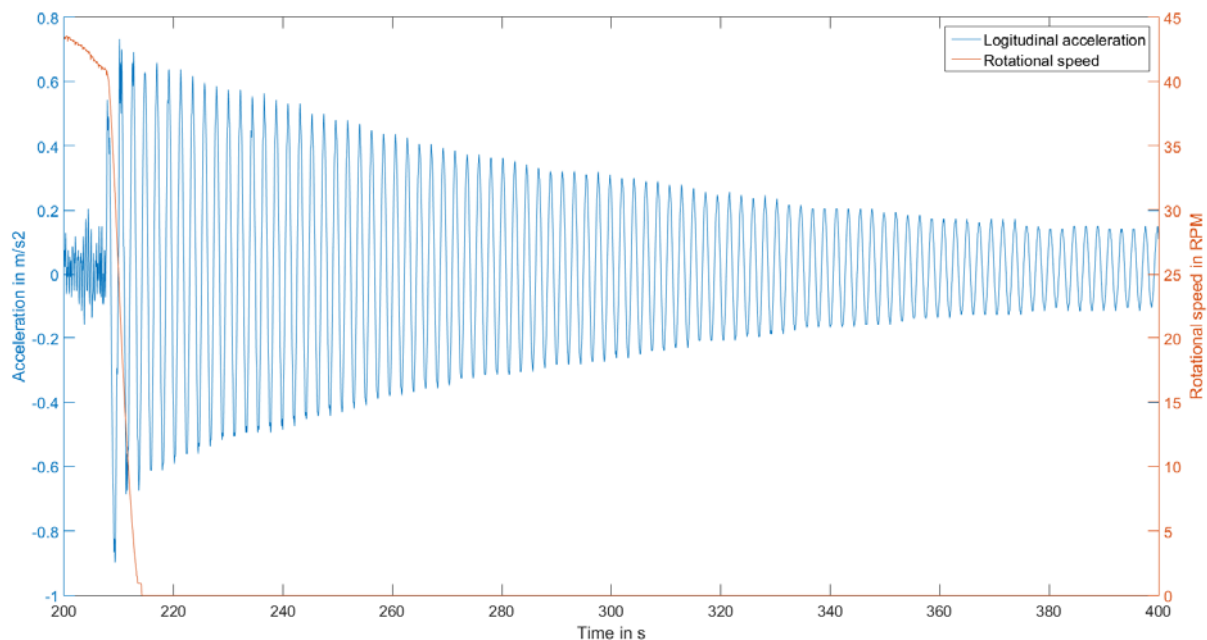


Figure 77: Plot of longitudinal acceleration and drive train speed during an emergency stop

However, the measurements can only be an indicator for the magnitude of the c_T -values as the wind turbine is not working in steady-state operation before the emergency stop. Furthermore, there is a great uncertainty in the wind measurement on the nacelle of the wind turbine. Hence, the mean value of the tip speed ratio and the calculated c_T -values are used to shift the curves from the literature. The resulting c_T -curve is within a typical range for the tip speed ratios, which occur in during normal operation.

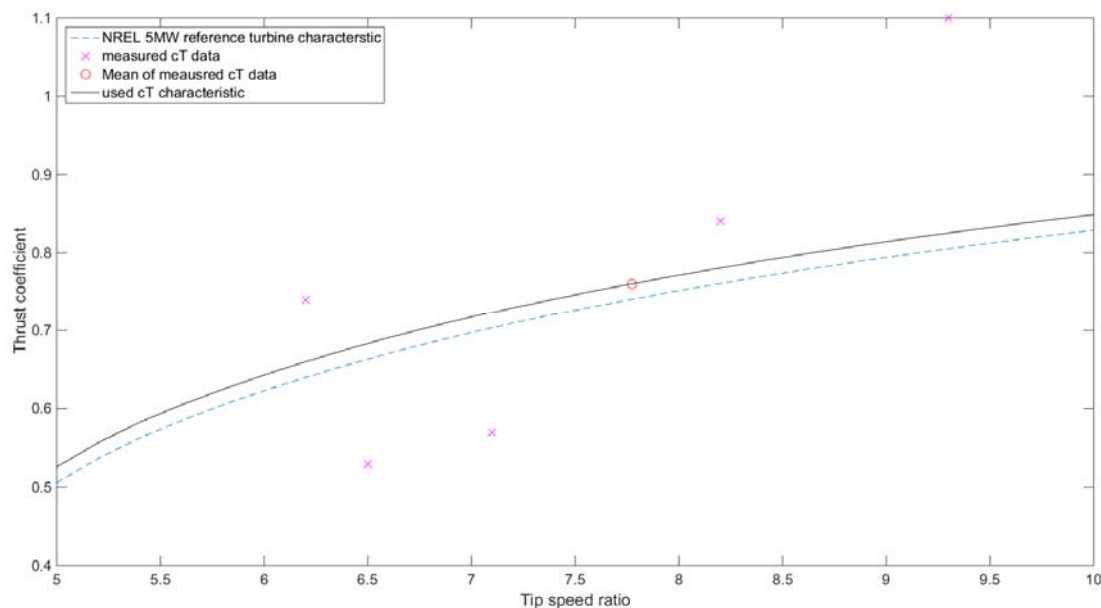


Figure 78: Comparison of measured values for c_T with data for the NREL 5 MW reference turbine

Model of the Mechanical Structure of the Rotor and of the Drive Train

The mechanical drive train of the E30 consists of the blades, the hub, the main shaft with the rotor brake disc, and the rotor of the generator. The blades are the softest part of the drive train with the lowest Eigenfrequency. Usually it is distinguished between the flapwise and the edgewise Eigenfrequency. At a pitch angle close to zero degree any movement in flapwise direction is out of the rotor plane. As out of plane movements do not directly affect the rotational speed and cannot be simulated with the used aerodynamic model. On the contrary any movements in edgewise direction are in the rotor plane and have therefore a direct impact on the rotational speed. These movements must be accounted for by the simulation model. However, the rotor blades shall also be represented by a simple model, as the aerodynamic model does not allow simulating different wind speeds over the rotor plane. Hence, a complex model of the blades would not lead to better results. Therefore, the blades are modelled as a stiff ring, which is connected to the hub via springs. This allows simulating the blade dynamics in plane as a torsional system. This model was proposed by [12].

The rest of the mechanical drive train is modelled as a two-mass model as typically used. The hub and the brake disc are considered as one mass, which is connected to the second mass (the rotor of the generator) by a spring-damper system. Hence, the whole mechanical drive train is represented by a three-mass model as shown in Figure 79.

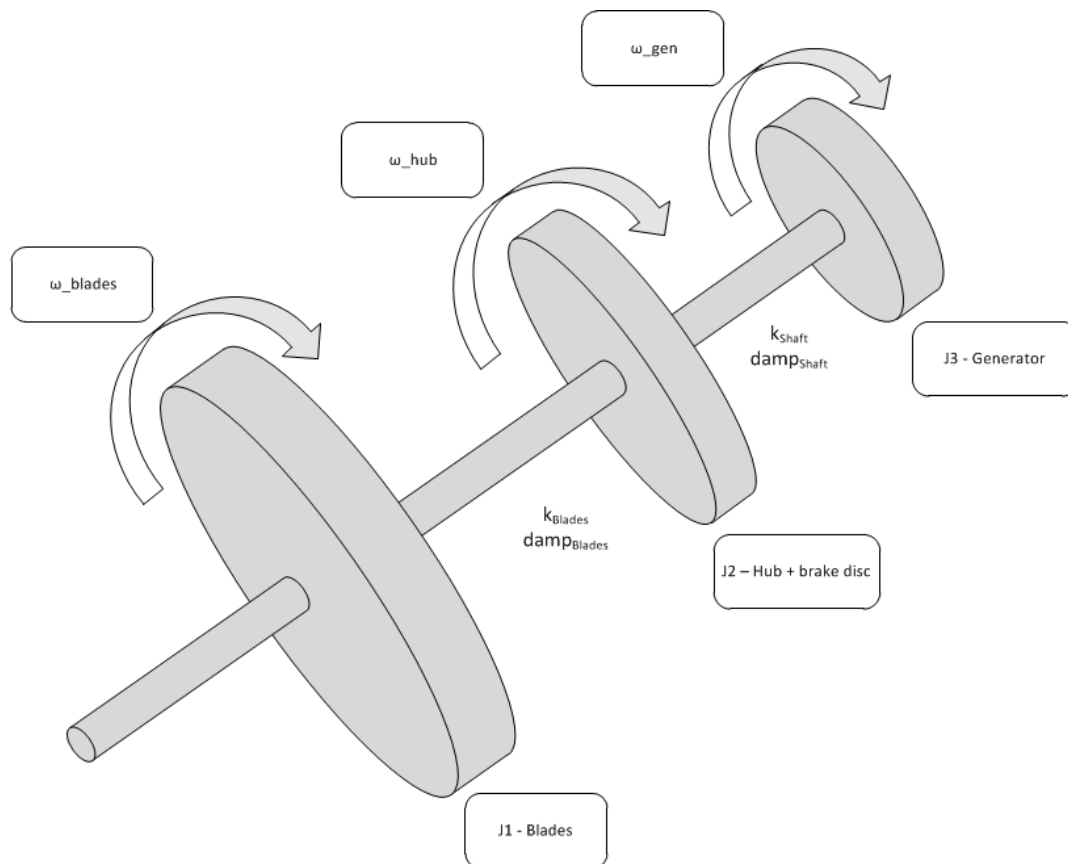


Figure 79: Three-mass representation of the drive train

For all three masses the mass moment of inertia has to be determined. This is done by using information from the structural assessment and FEM models of the drive train which were created in a previous project [6]. The spring coefficients are determined by analysing the frequency spectrum of the rotational speed measurement (blue line in Figure 80). There are three dominant frequencies (3 Hz, 7.8 Hz and 9.7 Hz) which are representative for the dynamics of the drive train. The Eigenfrequency at 3 Hz was also the most dominant measured Eigenfrequency of the blades in a previous project [6]. The two lower frequencies are used to determine the spring coefficients. The peak at about 2.1 Hz in the frequency spectrum is showing the 3-p effect. The damping coefficients are adjusted in the simulation model itself. The two springs of drive train model are separated and excited by an impulse of the driving moment. The damping coefficients are set to values at which the oscillations are decreasing in a reasonable time. Figure 81 shows the block diagram of the used drive train model

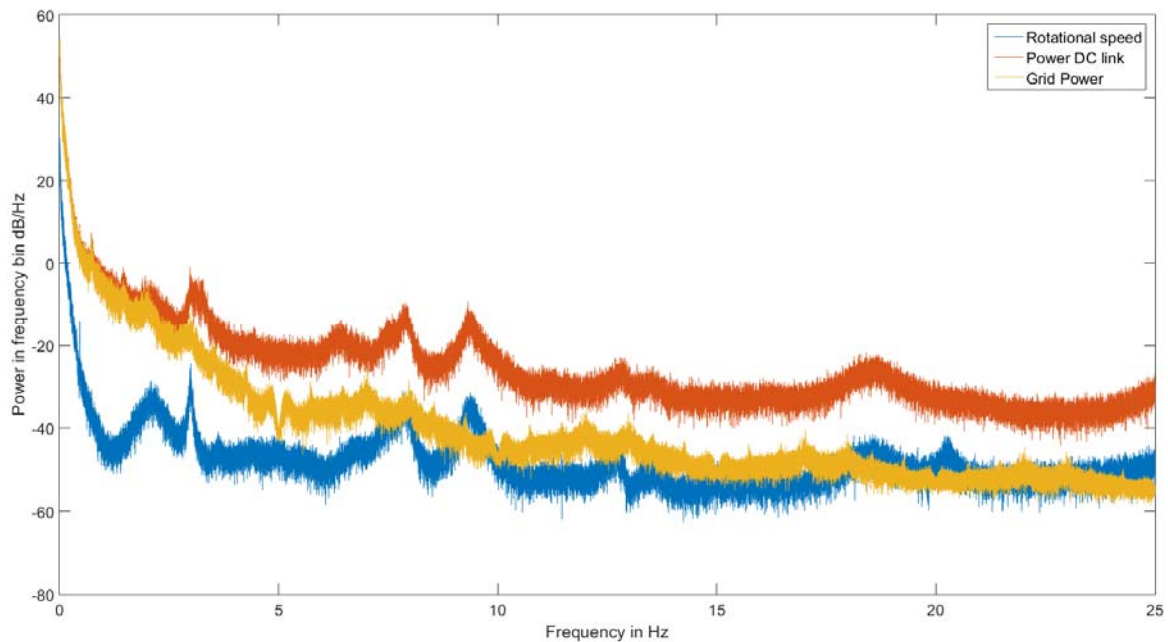


Figure 80: Frequency spectrum of measured power and of measured rotational speed

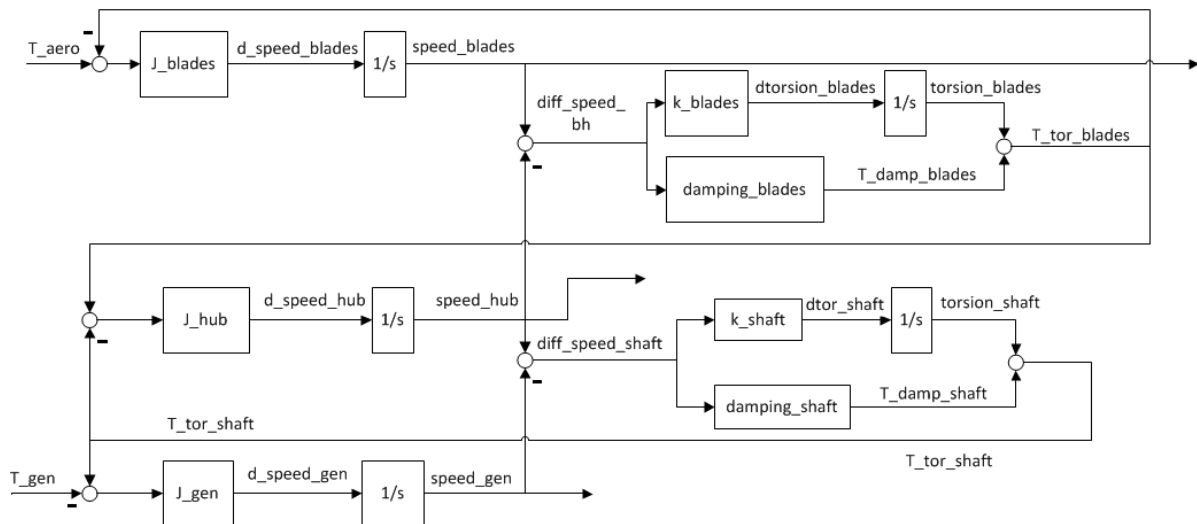


Figure 81: Block diagram of the drive train model

Imbalance Model

The measurements with the acceleration sensor at the E30 (see chapter on Longitudinal and Lateral Acceleration Measurement in Nacelle) show strong lateral oscillations of the tower,

whenever the drive train speed is close to the first Eigenfrequency of the tower (i.e. a 1p effect, see Figure 82).

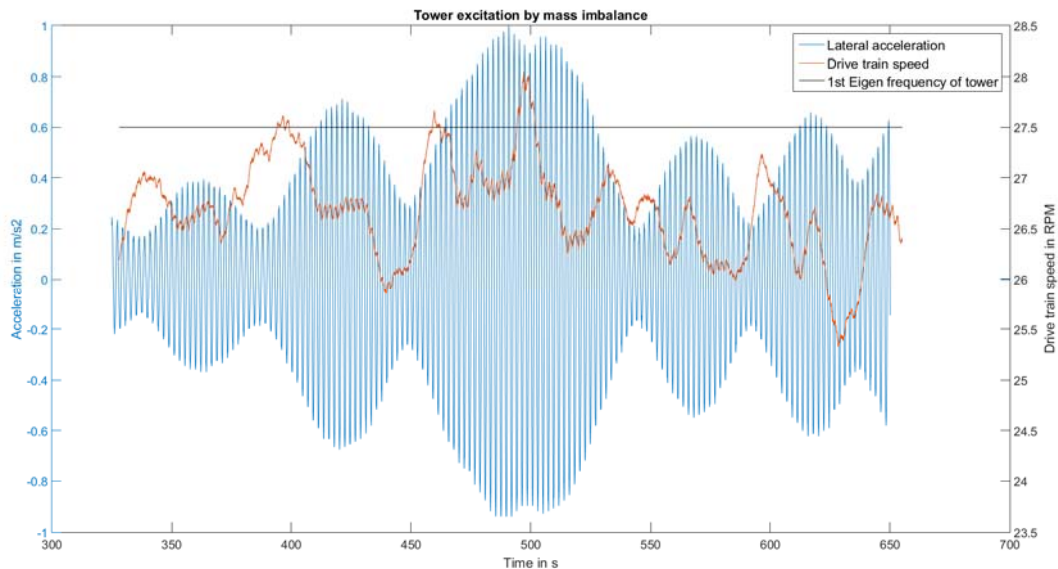


Figure 82: Tower excitation by mass imbalance

These oscillations are most likely caused by mass imbalances in the rotor blades. Hence, an imbalance model is included to simulate the excitation force acting on the tower. This force is modelled as lateral force with a sinusoidal characteristic. Its magnitude and phase are defined by the centrifugal force of a mass m_{imb} , which rotates at a distance r_{imb} and a speed Ω_{hub} around the centre of the drive train (see Figure 83).

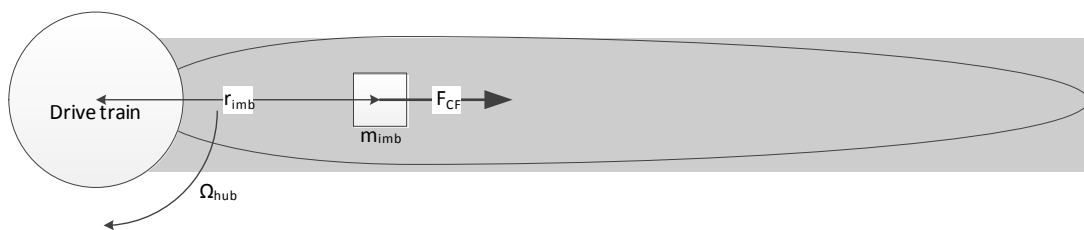


Figure 83: Imbalance model

The centrifugal force is a function of the rotational speed and the two parameters m_{imb} and r_{imb} . It is calculated with the well-known Equation 8.

$$\mathbf{F}_{CF} = \mathbf{r}_{imb} \cdot \mathbf{m}_{imb} \cdot \Omega_{hub}^2 \quad \text{Equation 8}$$

The lateral excitation force is calculated by combining the centrifugal force with the rotor position using Equation 9.

$$\mathbf{F}_y = \mathbf{F}_{CF} \cdot \sin \varphi_{Rotor} \quad \text{Equation 9}$$

The distance to the centre of rotation and the mass imbalance are determined by feeding measured time series of the drive train speed into the imbalance model and comparing the simulated lateral acceleration of the tower with its measured values (see Figure 84). When the product of r_{imb} and m_{imb} is assumed to be $53 \text{ kg} \cdot \text{m}$ the simulation shows a good agreement with the measurements.

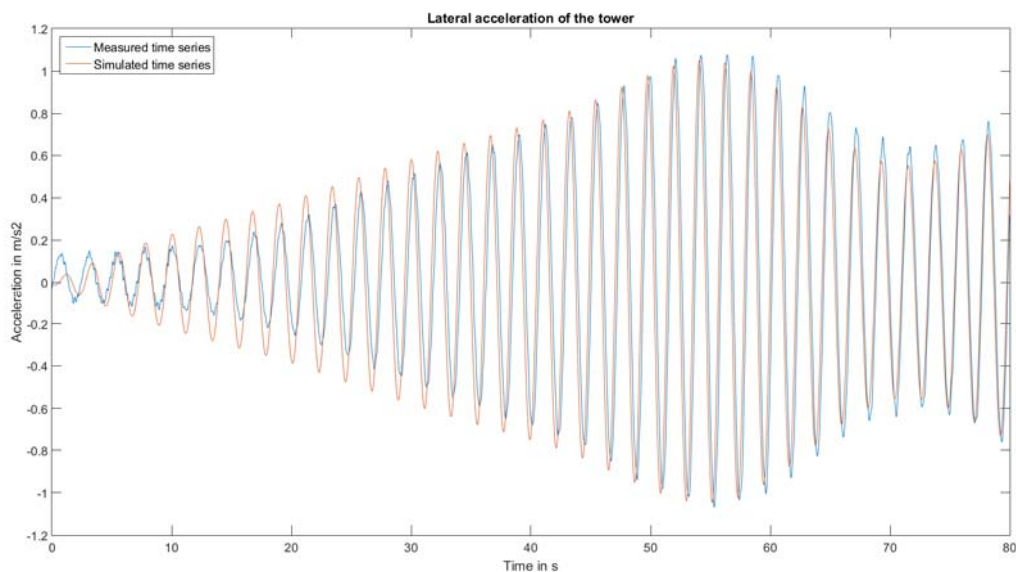


Figure 84: Comparison of measured and simulated lateral acceleration of the tower

Model of the Tower

The tower of the wind turbine is modelled as a harmonic oscillator with a concentrated mass at the tower head which is connected to the foundation by a combination of spring and damper (see Figure 85). The tower is stiffly connected to the foundation. The model describes the first Eigenform of the tower in lateral and longitudinal direction. The tower model is excited by two

forces: a thrust force in longitudinal direction resulting, which is created by the aerodynamic, and an imbalance force, which is created by the mass imbalance of the rotor (see Equation 8). The effect of the imbalance force strongly depends on the rotor speed, as its frequency is equal to the first Eigenfrequency of the tower for a certain rotor speed (see Figure 104).

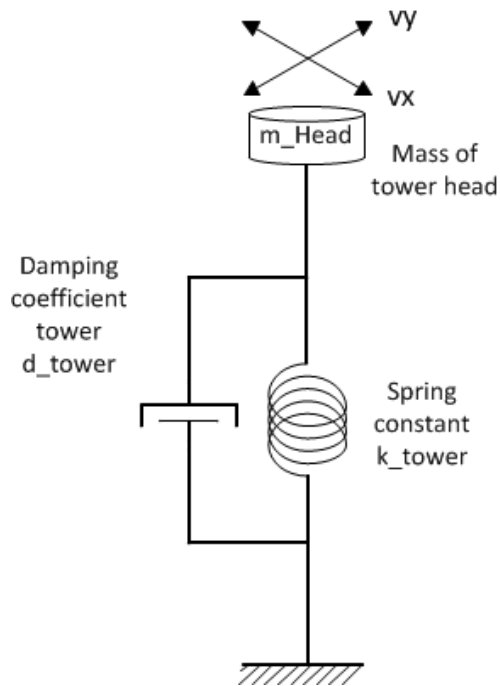


Figure 85: Model of the tower

The parameters for the model are determined by using information from the structural assessment, and measured time traces during emergency stops as well undisturbed operation. All needed equations can be found in [13]. The representative mass of tower and tower head is known from the structural information. Its value is determined to be 20,653 kg. The damping constant and the damped Eigenfrequency is derived from the decaying tower oscillations after several emergency stops measured with the installed acceleration sensor. Figure 77 shows such a measured time series. The acceleration in longitudinal direction shows a decaying behaviour. The damping constant can be determined by fitting an exponential curve through the local maxima of the measurements. The derived value for the damping constant for the lateral direction is 250 kg/s. A wind speed depending share is added in longitudinal direction. Hence, the damping constant for this direction varies between 250 kg/s at cut-in wind speed and 515 kg/s at cut-out wind speed. The damped Eigenfrequency is determined to 0.459 Hz by performing a frequency analysis over several time series of acceleration measurements in both

directions. The spring coefficient of the tower can be calculated from the already determined values. Its value is determined to be 171,780 N/m.

Model of the Generator-Converter-Unit

A generic model is used to simulate the generator-converter-unit. The dominant frequencies of the power are analysed and compared with the frequency spectrum of the rotational speed (see Figure 80). Figure 80 shows that low frequencies (< 10 Hz) are dominant in the grid power frequency spectrum. Furthermore, these frequencies are also present in the frequencies spectrum of drive train speed. These frequencies are caused by the drive train oscillations and are not generated in the converter. Hence, the electrical processes in the generator-converter-unit, which are associated with high frequencies in the spectrum, do not have to be modelled. The power controller and the generator are modelled as PT1 elements, which represent the behaviour of the generator – converter unit in the time domain according to the IEC standard for generic models [14]. It is enhanced by a logic which considers the modified speed set point for reduced power set points (see chapter on Control strategy). Figure 86 shows the block diagram of the used model.

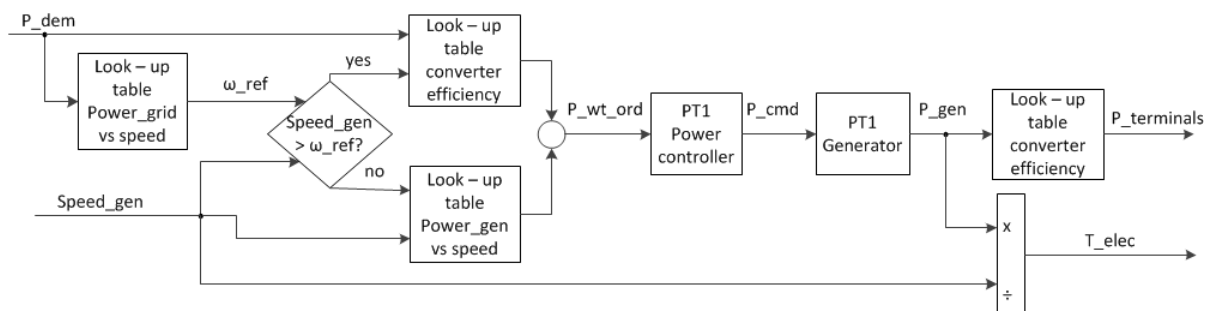


Figure 86: Block diagram of the model of the generator-converter-unit

Both look-up-tables are derived with measured data as described in the chapter on Control strategy. The time constants of the model are determined with data from laboratory exercises. Time series of measured rotational speed are fed into the model. The simulated power values are compared with measured power values for different parameter combinations. The time constants which show the best agreement between measurements and simulation are 0.78 for the power controller and 0.1 for the generator.

Model of the Speed Controller with Actuator

As the E30 is a wind turbine with variable speed its rotational speed has to be controlled. This is done by controlling the pitch angle. The speed set point depends on the chosen power set point

for the grid power. The speed controller must be adjusted carefully as it can cause critical oscillations in all mechanical parts of the turbine. One method to avoid stimulations is to limit the rate of change of the power set point. This is done in the E30 and has therefore to be modelled. Measurements during changes of the power set points show a constant rate of change for the grid power (see Figure 88). Hence, a power demand rate limiter is included in the speed controller as shown in Figure 87.

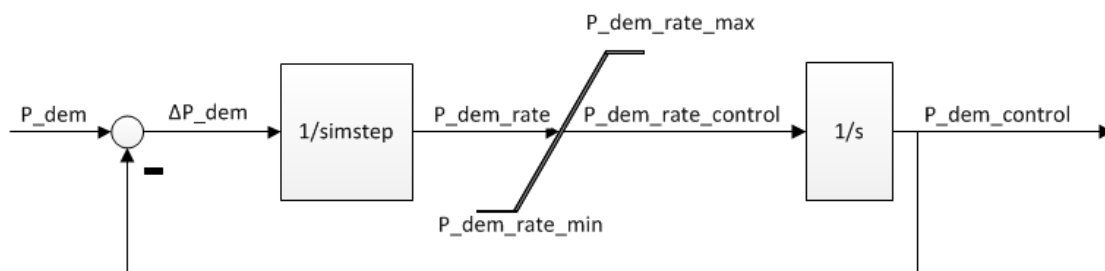


Figure 87: Block diagram of the power demand rate limiter as part of the speed controller

The parameters of the limiter are determined with data acquired during laboratory exercises (see Figure 88). During these exercises the power set point is changed regularly. While Figure 88 also shows increases of the power set point, only data acquired during decreases are used for the parameter determination.

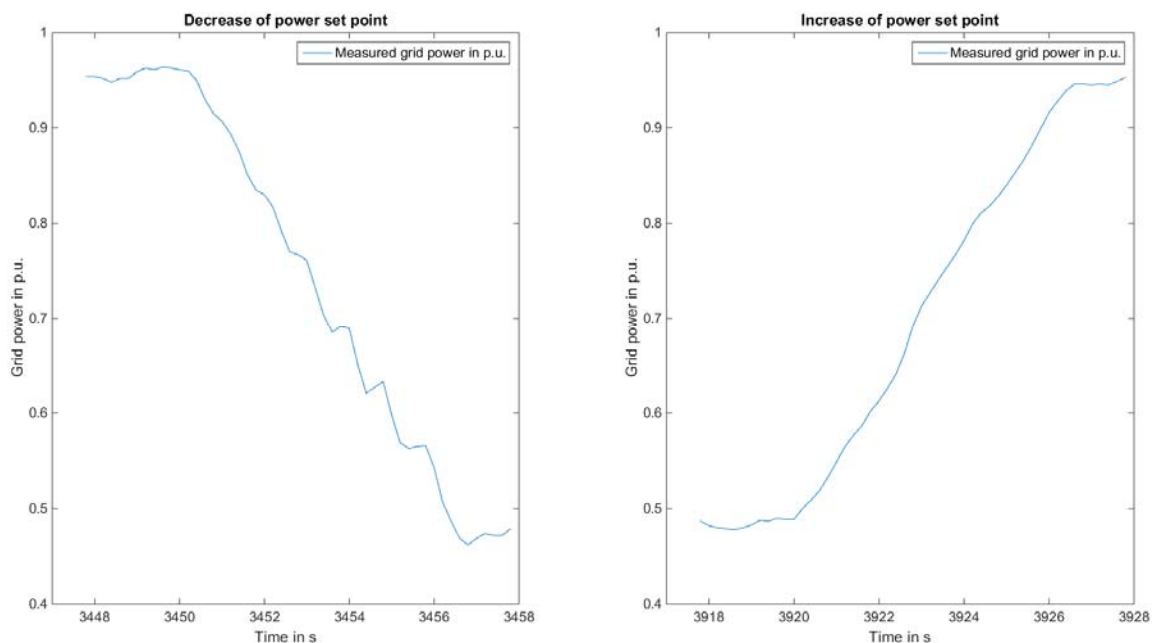


Figure 88: Measured grid power during a decrease (left) and an increase (right) of the power set point

From this data the difference of the measured grid power between begin and end of the power decrease is calculated. These values are plotted versus the elapsed time during the decrease (see Figure 89). A line is fitted through these data points by performing a linear regression. The slope of the line represents the maximum rate of change of the power set point which is used in the model (0.068 p.u./s). The fitted line has a high coefficient of determination (0.936).

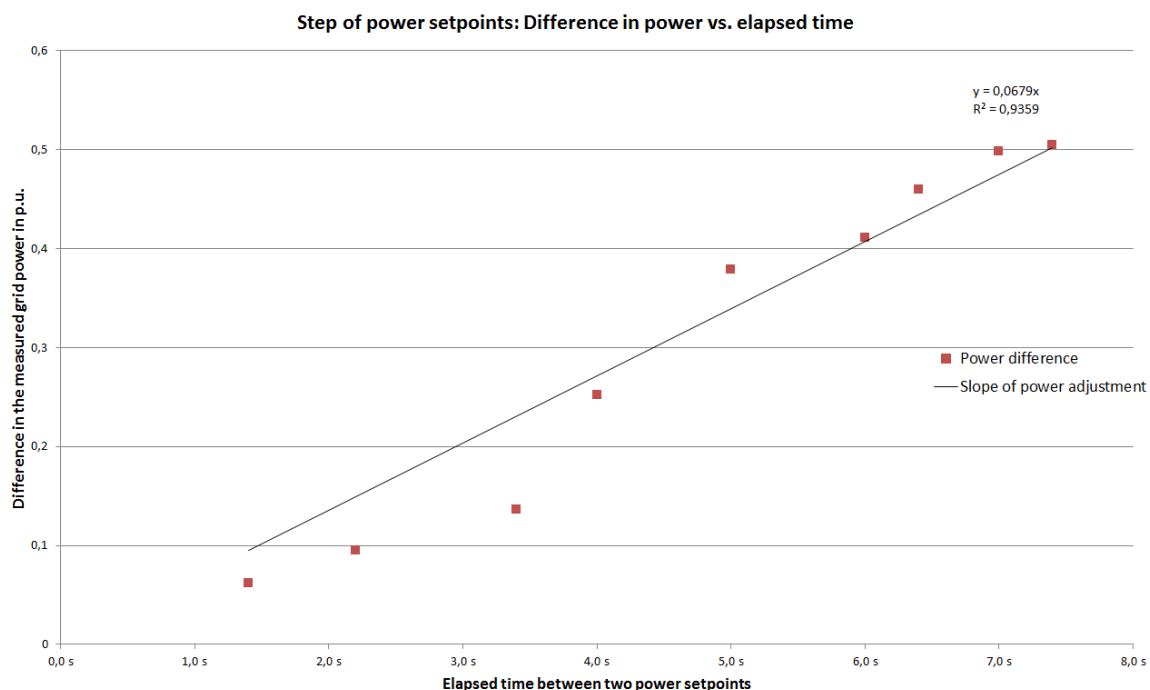


Figure 89: Difference in measured grid power vs. elapsed time for different steps in the power set point

In the next step the speed set point has to be determined from the power set point. Usually this is done by a power-vs-speed-characteristic of the wind turbine. For the E30 it is slightly different as the characteristic looks different for reduced power set points than for undisturbed operation (see Control strategy). Hence, it can be distinguished between undisturbed operation with a speed set point of 1 p.u. and reduced power set point operation (see Figure 90). The determination of the needed look-up-table is explained in the chapter on Control strategy. With this value a speed error can be calculated.

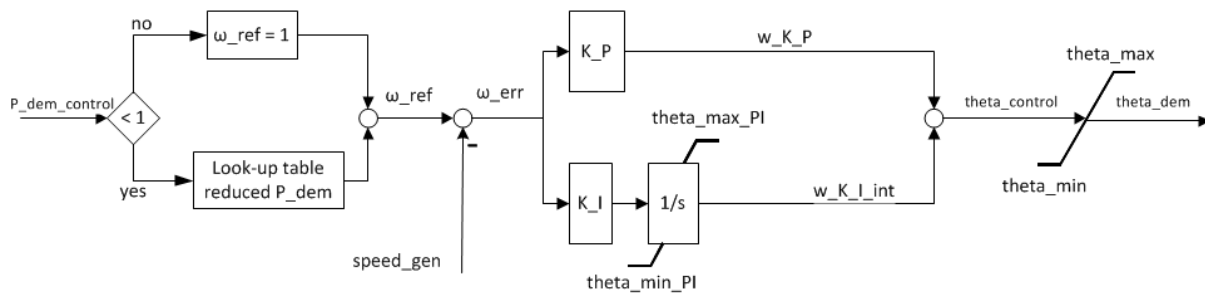


Figure 90: Block diagram of the speed controller

The needed pitch angle is calculated from this speed error by using a PI controller. The controller parameter are being determined by a methodology based Ziegler and Nichols methodology for PI controller [15]. The system is excited by a wind speed change from 17 m/s to 25 m/s within one second.

A simulation is performed with $K_I = 0$ and a high K_P , i.e. $K_P = -1500$. With such a high K_P the slew rate of the pitch drive limits the change of the pitch angle. This is not desired as it decreases the linearity of the system even further than already done by the aerodynamic. Therefore K_P must be reduced to a value at which the slew rate operates barely in its limits. The determined K_P is multiplied with a safety factor of 0.45, according to Ziegler and Nichols.

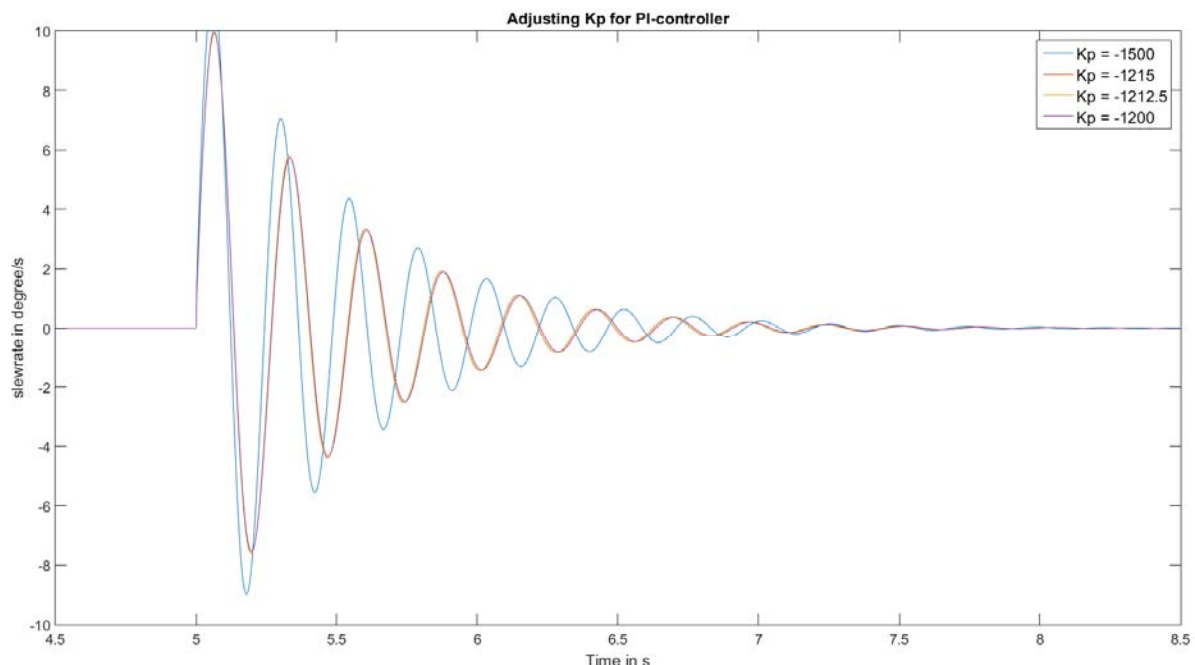


Figure 91: Determination of controller parameter: proportional term

Figure 91 gives an overview over the influences of different K_P values. The maximum allowable K_P is -1,212.5, which leads to a slew rate of the pitch angle just below 10.9 deg/s. This value is multiplied with the safety factor. The final K_P is therefore -606.25.

In a first attempt K_I is also determined according to Ziegler in Nichols. However, the system becomes unstable with such a value. Hence, simulations with different K_I are performed in order to reduce the rotational speed error to a small value within a reasonable time (see Figure 92). A compromise must be found between small K_I values, which cause a high remaining speed error (e.g. for $K_I = 10$), and high values, which can cause oscillations in the system (e.g. $K_I = 500$). Both requirements were fulfilled satisfactorily for a $K_I = -237.5$.

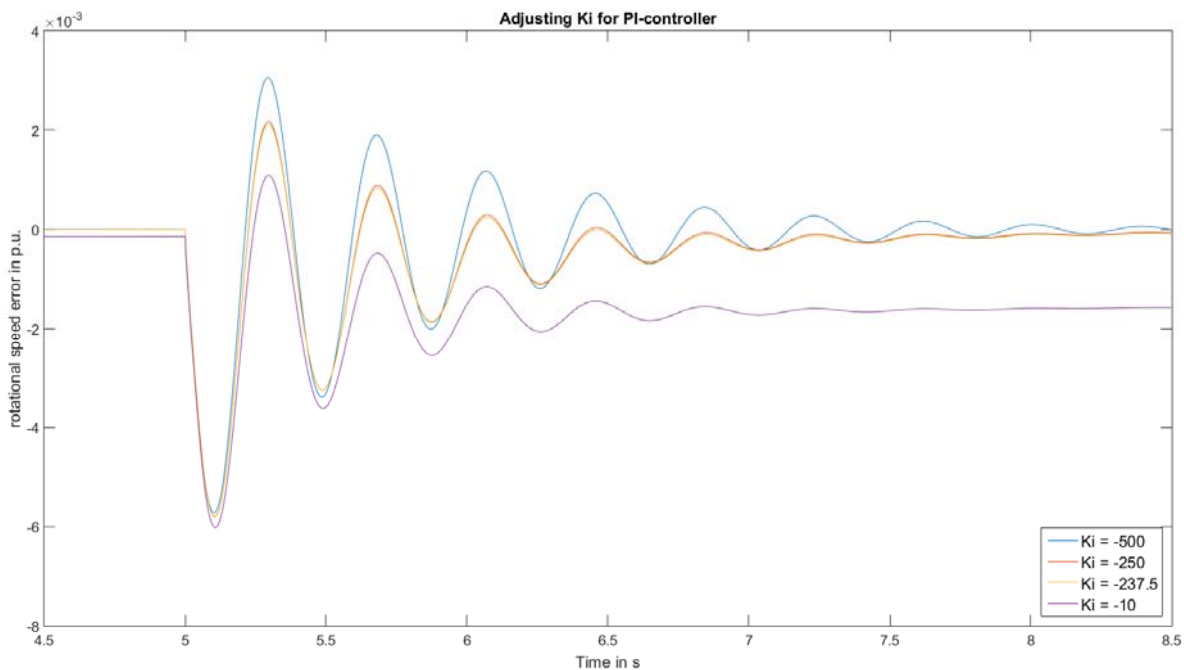


Figure 92: Determination of controller parameter: integral term

As the pitch angle is limited by an upper boundary (90deg) and a lower boundary (1 deg), anti-wind up is used for the integrator in PI-controller.

The pitch angle calculated with the controller is set by a pitch drive with a limited slew rate and PT1 behaviour. The block diagram of the used pitch drive is shown in Figure 93. It has to be noted that the acceleration of the pitch drive is not limited. This leads to an inaccuracy, which is considered to be of minor importance, as the slew rates during power production mode are usually small compared to the maximum slew rate and are therefore reached fast.

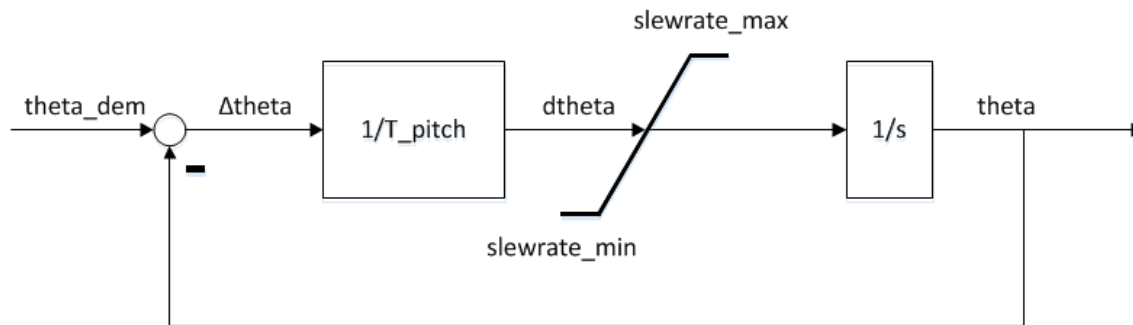


Figure 93: Block diagram of the pitch drive model

The Measurement of the slew rate is difficult due to the unsteady character of the pitch measurement. Discrete measurements of the pitch angle have to be used at times when a blade passes the pitch angle sensor. Hence, the calculated slew rate will always be an average value between two measurements. Measurements during several emergency stops of the WT were used to determine the slew rate. The measured slew rates varied between 10.1 deg/s and 12.1 deg/s (see Figure 94). Most of the differences can be explained by small deviations in the pitch angle measurement for the three blades which are related to imperfections of the installed wedges. Furthermore, according to data from the turbine control, the pitch angles of the different blades slightly deviate from one another. The overall average of the measured slew rates during emergency stops was 10.9 deg/s. Hence, this value was chosen as the maximum slew rate of the pitch drive.

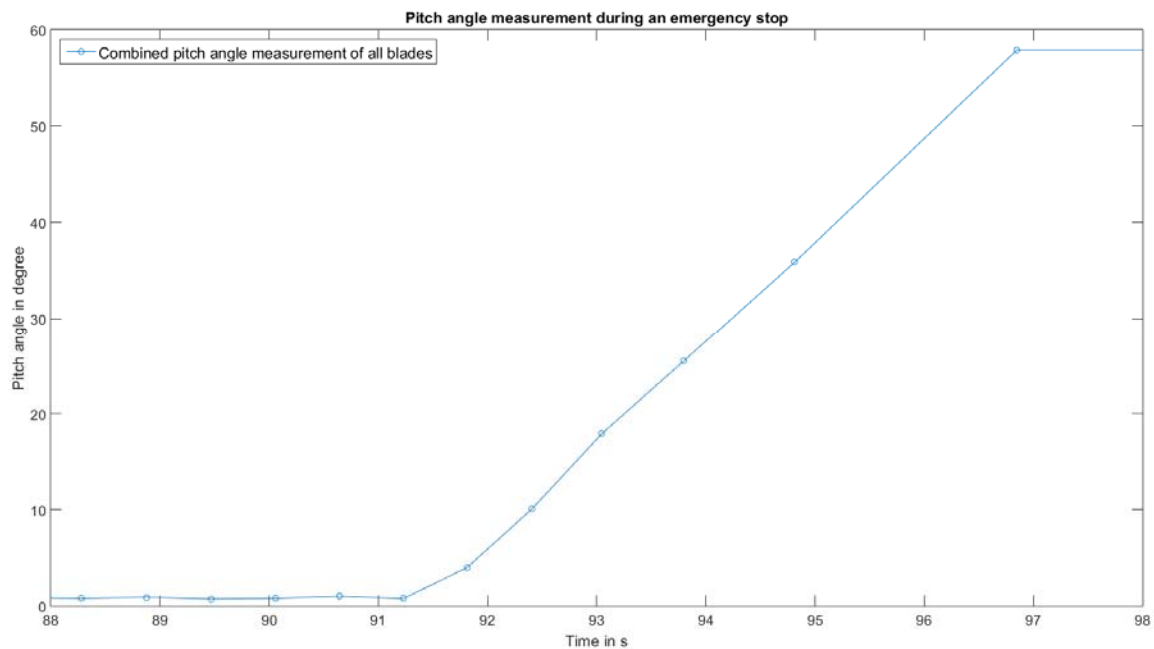


Figure 94: Pitch angle measurement during an emergency stop for all blades (pitch angles above 59 deg have not been measured during this event)

As the pitch angle is only measured three times per rotation, the exact time of the pitch command is unknown. Hence, the delay time of the pitch drive cannot directly be determined from the measurements. As shown in Figure 94 the pitching process starts sometime between the two pitch measurements between 91 and 92 seconds. The slow rate of the pitch angle between these measurements is only 5.6 deg/s. The difference in the slow rate is a combination of the unknown time of the pitch command, the limited acceleration of the pitch drive (which is not modelled) and the delay time of the pitch drive. These three effects cannot be separated. However, a maximum value for the delay time can be deducted from all analysed emergency stops. Assuming that the slew directly jumps to the average value of 11 deg/s, the time difference between the last pitch angle measurement and the start of the pitch process can be determined. The minimum of the time differences for all emergency stops is 0.15 seconds. This is assumed to be the delay time.

Control strategy

One important feature of the control strategy is the power-vs-speed-characteristic. Similar to the c_p and c_T tables it is derived for steady-state operation of the wind turbine (see Aerodynamics of the Rotor). Hence, the same data set of 10-min-average values from the SCADA system is used to derive the characteristic for the grid power. The SCADA data do not include information

about the generator power. Hence, the characteristic of the generator power has to be derived from measurements with the Dewetron. Even though data from both measurement systems (SCADA and Dewetron) show good agreement, it is reasonable to change the methodology of generating the data as little as possible. Hence, long term data from the Dewetron is only used to determine the losses of the converter to represent the difference between generator power and grid power. These losses vary with the operational points. Every value of the grid-power-vs-speed-characteristic is divided by its corresponding converter efficiency to compute the power-vs-speed-characteristic for the generator. The results for both characteristics are shown in Figure 98.

When the wind turbine is running at a reduced power set point, it uses a different power-vs-speed-characteristic compared to undisturbed operation. Figure 97 shows the characteristic for the grid power created from instantaneous measurements. The different speed set points are visible as horizontal extensions to the power curve for undisturbed operation. The speed set point at a given power set point is increased (see also Figure 98). Hence, the turbine usually runs at a higher rotational speed than necessary to produce a certain power, which allows a steadier power production.

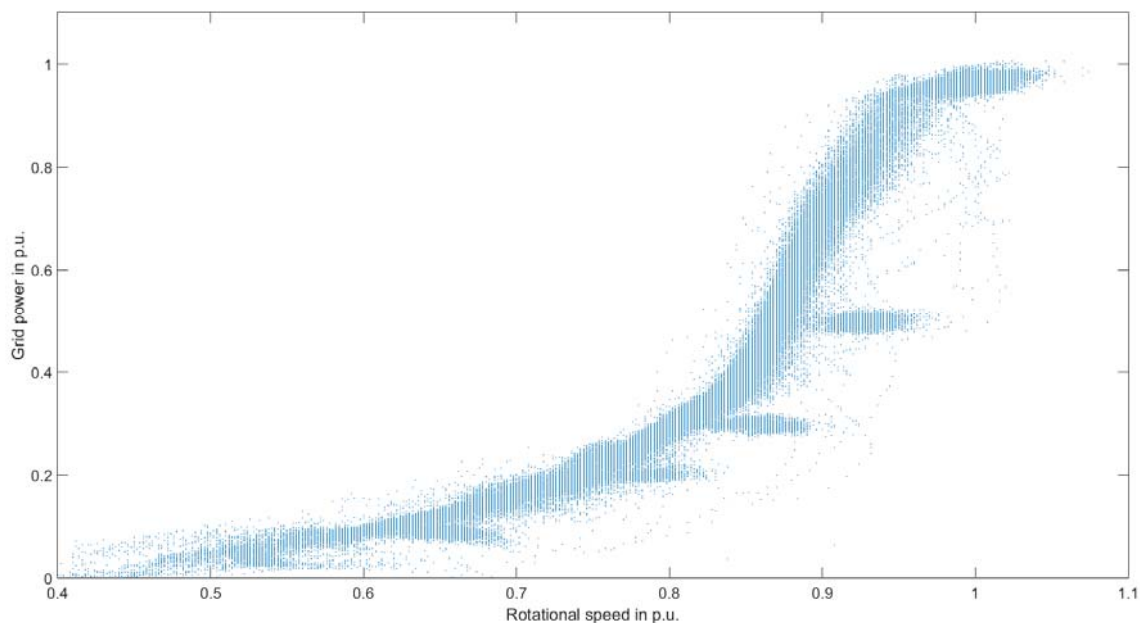


Figure 95: Grid-power-vs-speed-characteristic created from instantaneous values

The modified power characteristic was created from measurements, which were acquired while the turbine was running at the five different power set points. Some power set points were measured several times. A typical time series of measured values is shown in Figure 96.

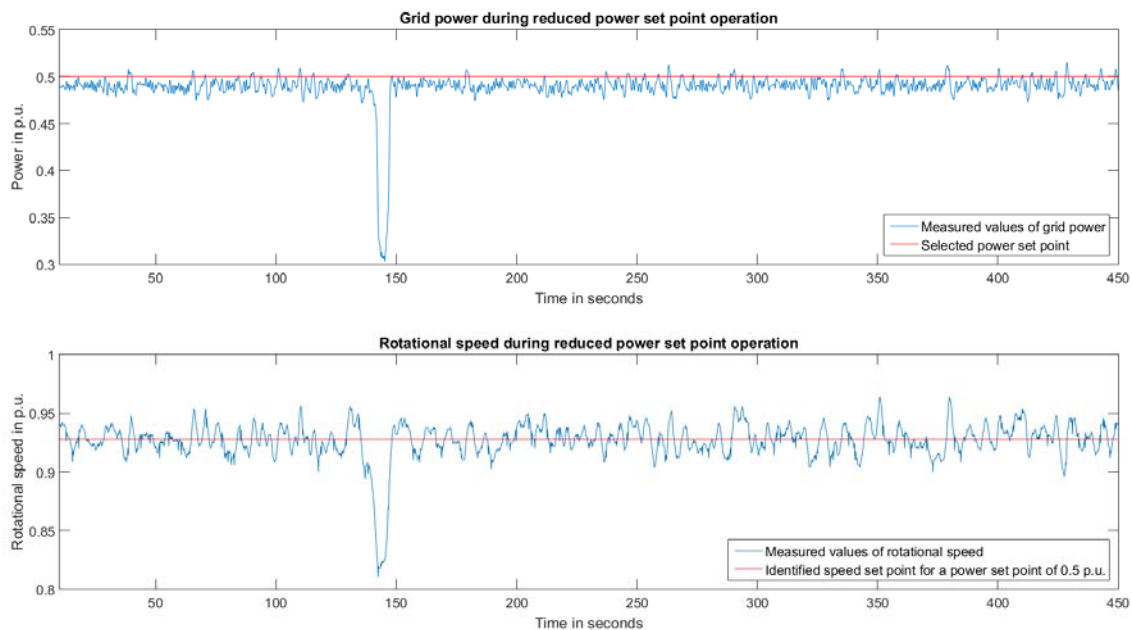


Figure 96: Measured values of grid power (top) and rotational speed (bottom) during reduced power set point operation

In each of these time series a speed set point was identified. In a first step the times series was reduced to time periods with sufficient wind to generate the chosen power (e.g. 0 s – 140 s and 150 s – 450 s in Figure 96). Then the average value of all rotational speed measurements during these periods was calculated. The identified speed-power-combinations are shown in Figure 97. As data is only available for certain reduced power set points, the power vs speed characteristic has to be determined by fitting a polynomial through the measured data. The result is shown in Figure 97. Although the maximum of the reduced power set points is far of 1 p.u. the polynomial should also be valid for higher power set points as the speed set point is already high for this power set point (0.93 p.u. speed set points for 0.5 p.u. power set point).

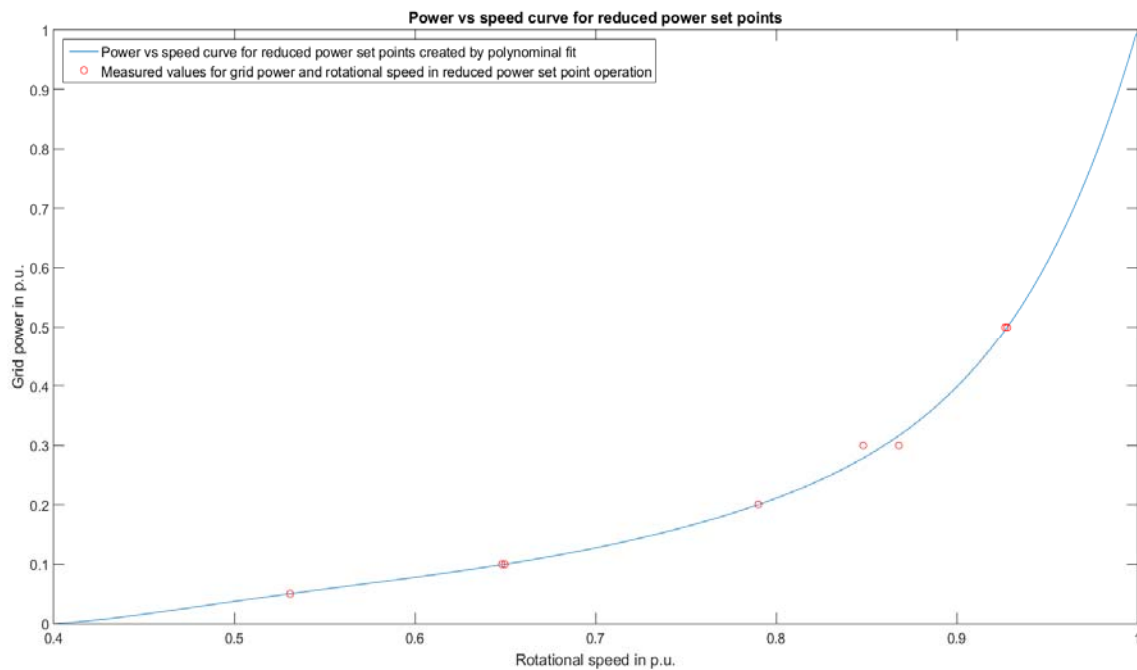


Figure 97: Comparison of fitted power-vs-speed-characteristic for reduced power set points with measured values

The power-vs-speed-characteristic for the reduced power set points is used as a look-up-table in the speed controller (see Figure 90).

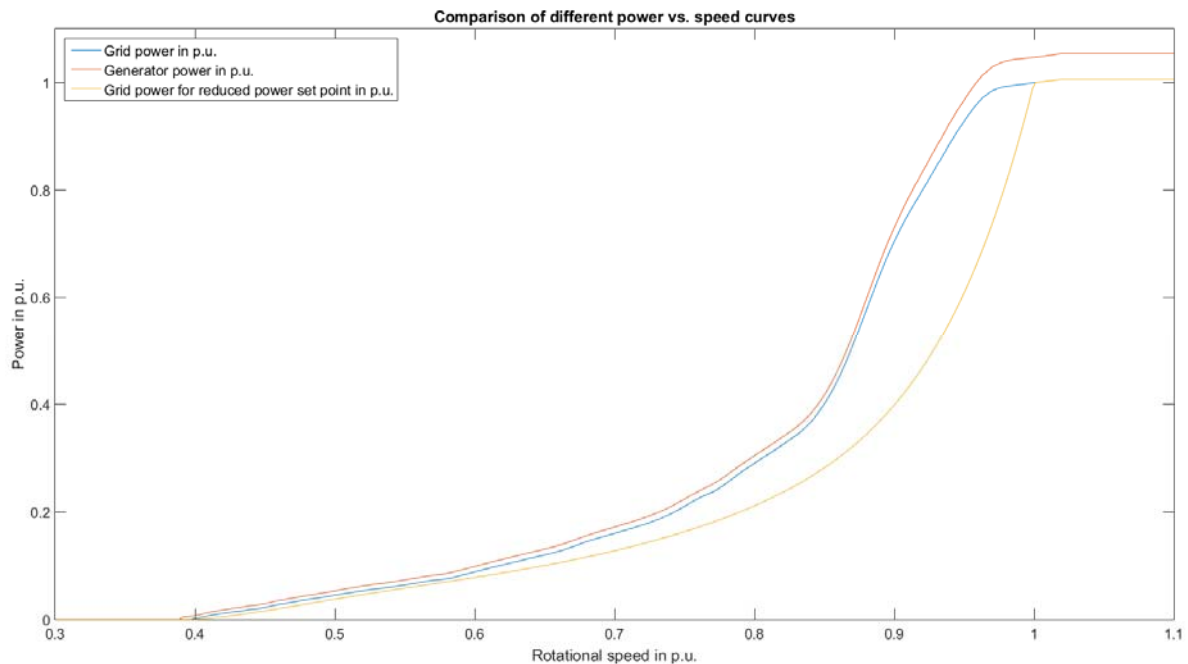


Figure 98: Comparison of power-vs-speed-curves for grid power (normal operation and reduced power set point) and generator power.

In order to derive the pitch control strategy the pitch angle is measured and plotted versus the rotor speed. However, the pitch angle sensor described in the section Pitch Angle Measurement only yields one pitch angle value for each blade per revolution of the rotor. Hence, the pitch angle is measured temporarily with a camera, as shown in Figure 99. The camera and a reference point are installed on the spinner of the rotor. A metric scale is attached to the blade root.

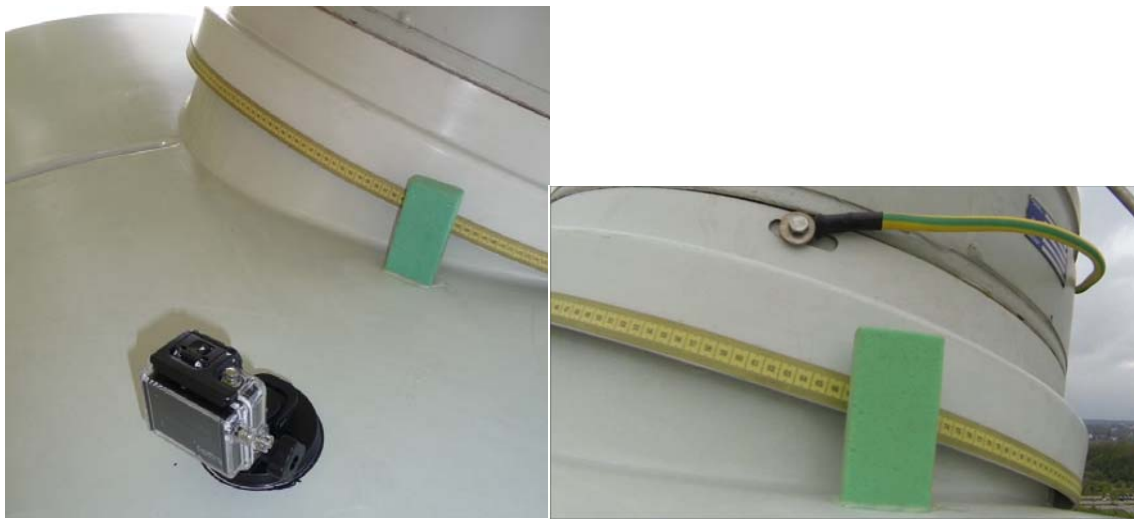


Figure 99: Continuous optical pitch angle measurement with a camera on the spinner. Left: camera on spinner. Right: view as seen by the camera

The pitch angle values are calculated from the metric scale readings as contained in the video clip. The resulting pitch angle and pitch rates vs. rotor speed are plotted in Figure 100 for a starting up of the E30.

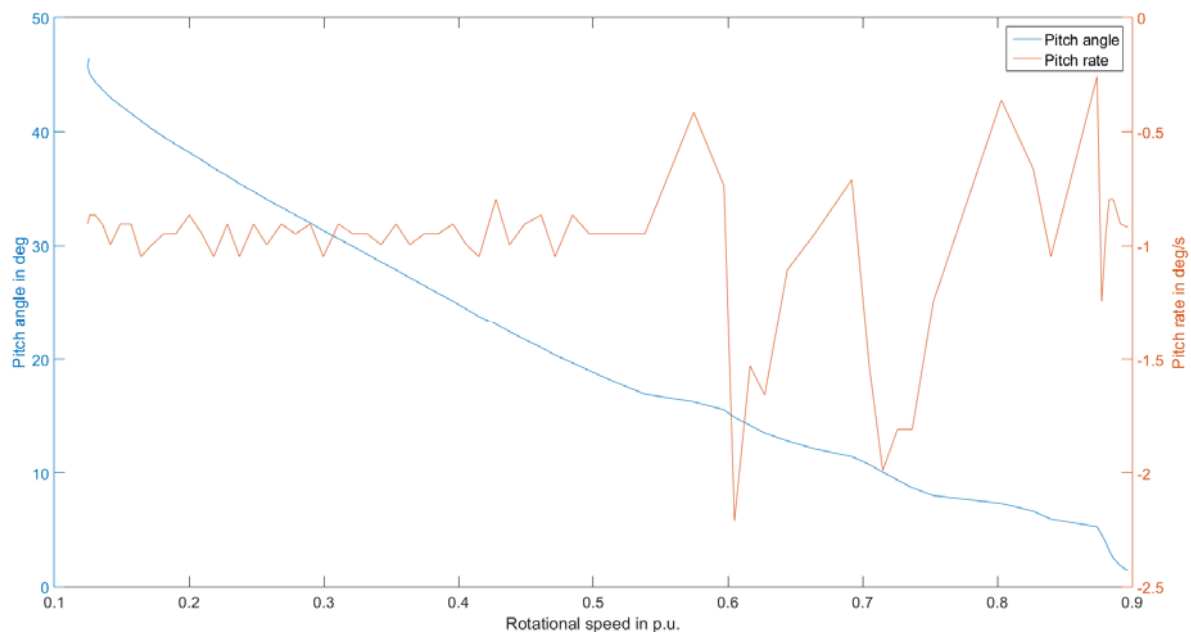


Figure 100: Pitch angle and pitch rate versus rotational speed during start-up of the E30.

The pitch angle and pitch rate for a soft braking procedure of the E30 are plotted vs the rotor speed in Figure 101. It has to be noted, that the x-axis is reversed in that figure to show the development in time.

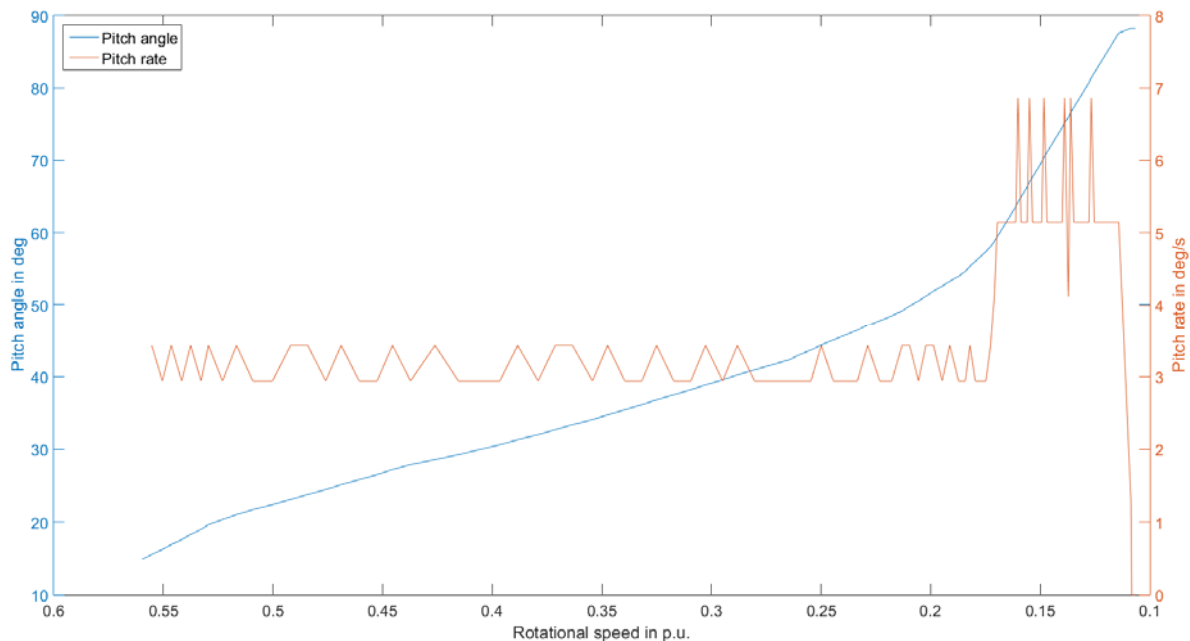


Figure 101: Pitch angle and pitch rate versus rotational speed during a soft braking procedure of the E30.

Model of the Grid

The connection of the wind turbine to the grid is modelled as a combination of the impedance of the cable to the transformer and the transformer itself (Figure 102). The voltage at the terminals of the grid-side-converter is adjusted in magnitude and phase. By doing so the produced active power is transmitted to the grid and there is no exchange in reactive power. The grid behind the transformer is modelled as an infinite stiff bus bar. Hence, the impedances of the cable and the transformer have to be determined.

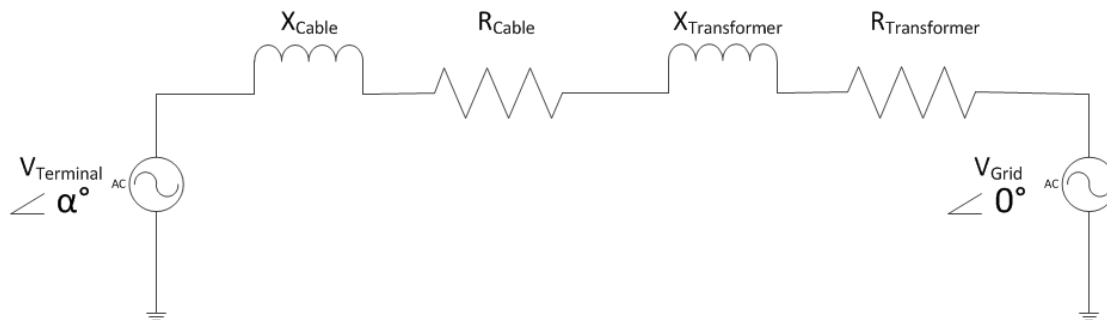


Figure 102: Equivalent circle diagram of the grid.

The transformer, which steps up the voltage from the wind turbine terminals (400 V) to medium voltage (15 kV), is modelled as an impedance. The real and imaginary part of this impedance are derived from the data sheet of the transformer, see Figure 103.

As the data sheet is in German, the names of all relevant parameters are translated to English and the corresponding values are listed in Table 3.

Table 3: Relevant transformer data

German	English	Symbol	Value	Unit
Bem.-Lstg kVA	Rated power	S_r	250	kVA
U_N	Rated voltage	V_r	15,000	V
Pk (In)	Short circuit power losses	P_{scl}	3.56	kW
Uk	Short circuit voltage	u_k	3.54	%

WKA 2006

Prüfungsnachweis Trafo-Union

WKA1

Typ 4H85467-3FA (Typ alt TS 5444F)		3 - Phasen		Öl-Transformator		Blatt-Nr. 02 Insges. 02 Blatt	
Baujahr 1995		Best.-Nr. G24H-P-T311-4055340		WNR: 3145 3172		Fabr.-Nr. KM 58495	
Besteller FACHHOCHSCHULE		Stellg. Spg.		OS		US	
VDE 0532		Art LT		Betriebsart DB		Daten bei 75 °C	
Kühlungsart ONAN		2-2		V		u. Übersetzg. 15000 V/ 400 V	
Bem. Frequenz 50 Hz		2-3		Un V		Sollwert 0.310 4.100 4.00	
D.-Kurzschl.-Str. kA		2-4		V		Toleranz + 15 % + 15 % ± 10.0%	
max. Kurzschl.-D. 2 s		Bem. Strom A		9.62		Werkprfg. 0.318 4.297 3.72	
Therm. Kl. OS/US		Betrieb		OS/US		Abnahme	
Schutzart IP00		Bem.-Istg. kVA		250		Gesamtgewicht 1.09 t	
Versand-schaltung V		Uk %		3.72		Öl-gewicht 0.25 t	
20000		Stellung		2-3		Öl-Sorte	
Isolations-pegel		Schaltgr.		Dyn5		Schaltschild	
LI125 AC 50 LI -- AC 3		Widerstandsmessung				O.-Nr.	
						bei 20.3 °C Werte in Ohm	
Ans./Stellg.		2-3					
1U - 1V		14.835				2U - 2V 0.006628	
1V - 1W		14.820				2V - 2W 0.006654	
1W - 1U		14.809				2W - 2U 0.008825	
Rmitt.		14.821				Rmitt. 0.007369	
Übersetzungsmessung							
Übersetzungen und Schaltgruppen entsprechend Leistungsschild geprüft							
Anschluß 1U-1V / 2N-2U ; 1V-1W / 2N-2V ; 1W-1U / 2N-2W							
Stellung		2-2		2-3		2-4	
Soll		67.550		64.952		62.354	
Ist		67.591		64.973		62.375	
f %		≤ 4.0		≤ 4.0		≤ 4.0	
Leerlaufmessung							
Anschluß 2U-2V-2W						bei 50 Hz	
Spg. in V		Ströme in A		%		Verluste in kW	
U		Io		Io		Io	
400		0.59		0.52		0.67	
		0.59		0.16			
Kurzschlußmessung							
Anschluß 1U-1V-1W						bei 50 Hz und bei 20 °C	
Kurzschluß 2U-2V-2W							
Stellg. Str in A		Spg in V		%		Verluste in kW	
I		U		Uk		Pk (In)	
2-3		9.48		531.5		3.559	
						4.297	
Wechselspannungsprüfungen							
Wicklungsprüfung		OS		50		50	
Wicklungsprüfung		US		3		50	
Wicklungsprüfung							
Windungsprüfung		US		0.800		100	
Bemerkungen:		Die von uns verwendeten Öl-sorten entsprechen VDE 0370 T1 - PCB-Gehalt nach DIN 51527 T1 < 1 ppm.					
		Prüffeld, 18.12.95					

Figure 103: Data sheet of the power transformer of the E30.

The transformer is modelled as impedance, Z_{tr} , on the 400 V level. The rated current I_r , is derived from the rated apparent power S_r and the rated voltage V_r , see Equation 10

$$I_r = \frac{S_r}{\sqrt{3} \cdot V_r} \quad \text{Equation 10}$$

I_r and the losses from the short circuit test of the transformer, P_{scl} , allow deriving the ohmic resistance, R_{tr} , of Z_{tr} .

$$R_{tr} = \frac{P_{scl}}{I_r^2} \quad \text{Equation 11}$$

The voltage drop across the resistance R_{tr} is V_R .

$$V_R = R_{tr} \cdot I_r \quad \text{Equation 12}$$

Deriving the voltage drop across the reactance, V_X , also requires the short circuit voltage u_k .

$$V_X = \sqrt{\left(\frac{u_k \cdot V_r}{100}\right)^2 - V_R^2} \quad \text{Equation 13}$$

The imaginary part of Z_{tr} is hence X_{tr}

$$X_{tr} = \frac{V_X}{I_r} \quad \text{Equation 14}$$

Which leads to the impedance that characterises the voltage drop of the transformer $Z_{tr} = R_{tr} + jX_{tr} = 0.033 + j0.021 \Omega$.

The voltage drop of the cable is also characterised by an impedance. The length and type of the cable are known from wiring diagrams of the turbine. Typical values for the resistance and the reactance of such a cable are taken from a cable manufacturer [16]. This leads to an impedance for the cable of $Z_{cable} = R_{cable} + jX_{cable} = 0.0011 + j0.0012 \Omega$.

Design of Controller for Enhanced Congestion Management

Controller Design

When the wind turbine should be controlled to enable a fast congestion management, oscillations in the system have to be avoided. A frequency analysis of all relevant measurements in this project shows that the tower is most likely to reach critical oscillations (see Figure 104). In fact, even during undisturbed operation the lateral accelerations exceed a critical threshold, when the wind turbine is running at a certain rotational speed (i.e. 28 RPM). Hence, the first draft of the controller is limiting the speed at which the demanded power is changed, when the combination of the longitudinal and lateral acceleration of the tower reaches a critical threshold.

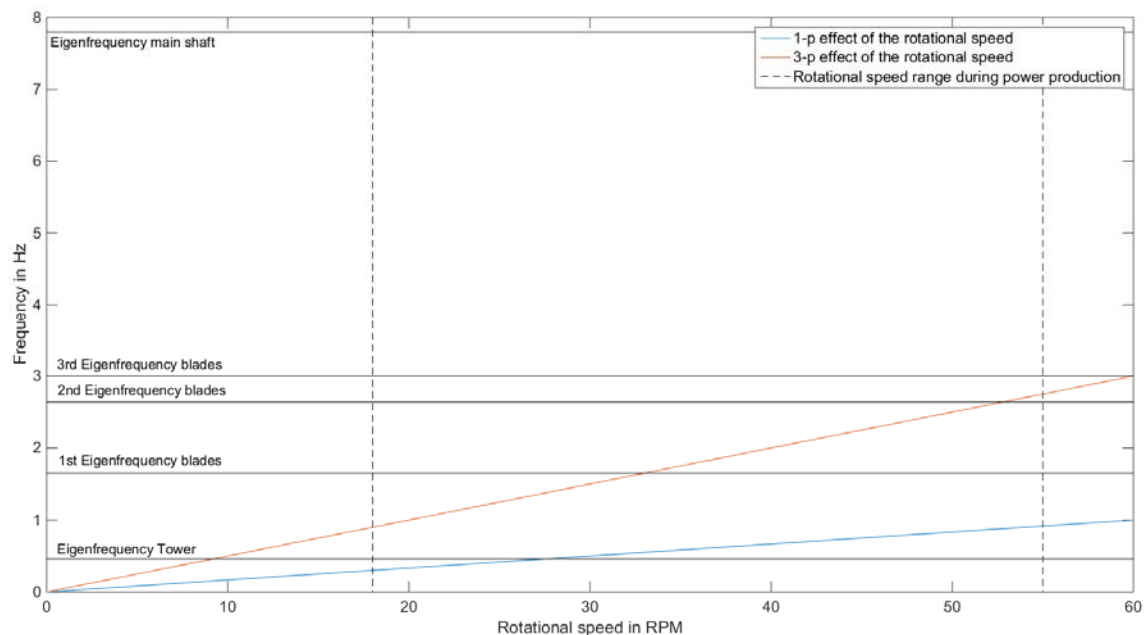


Figure 104: Campbell diagram of the E30

The E30 is already limiting the rate at which the power demand signal is changed (see chapter on Model of the Speed Controller with Actuator). The designed controller is modifying the external power demand signal before it enters the speed controller and the power controller (Eisman_controller in Figure 72). The controller is using a PT1 element with a time constant which is adjusted depending on the magnitude of the tower head acceleration. During undisturbed operation the E30 shuts down at lateral accelerations with a RMS value of 1.5 m/s^2 . This value should not be exceeded for the sum of lateral and longitudinal during the congestion

management and is therefore used to tune the controller. Figure 105 shows the bloc diagram of the used controller.

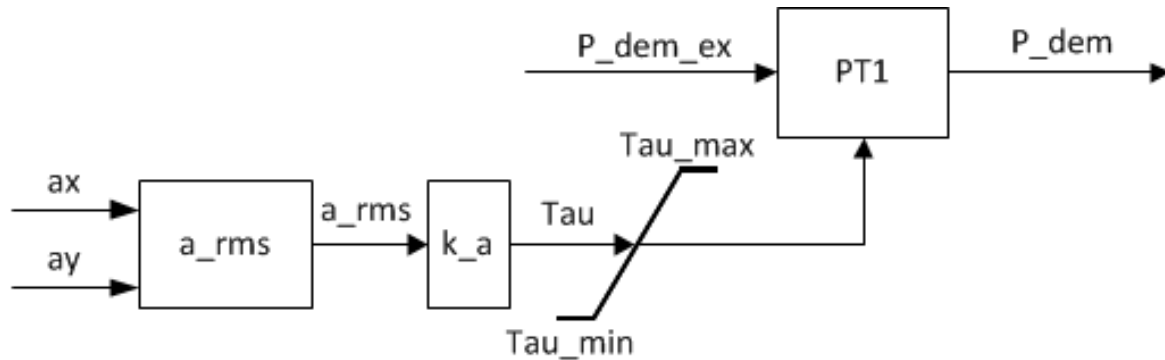


Figure 105: Block diagram of controller to modify the power limitation of the grid operator

An actual congestion management signal from the transformer station in Strübbel in 2015 [17] is used as external power demand signal (see Figure 106). The time steps of the signal are shortened until oscillations are excited in the wind turbine. For the first simulations the controller is disabled by choosing a very small Tau_{\max} .

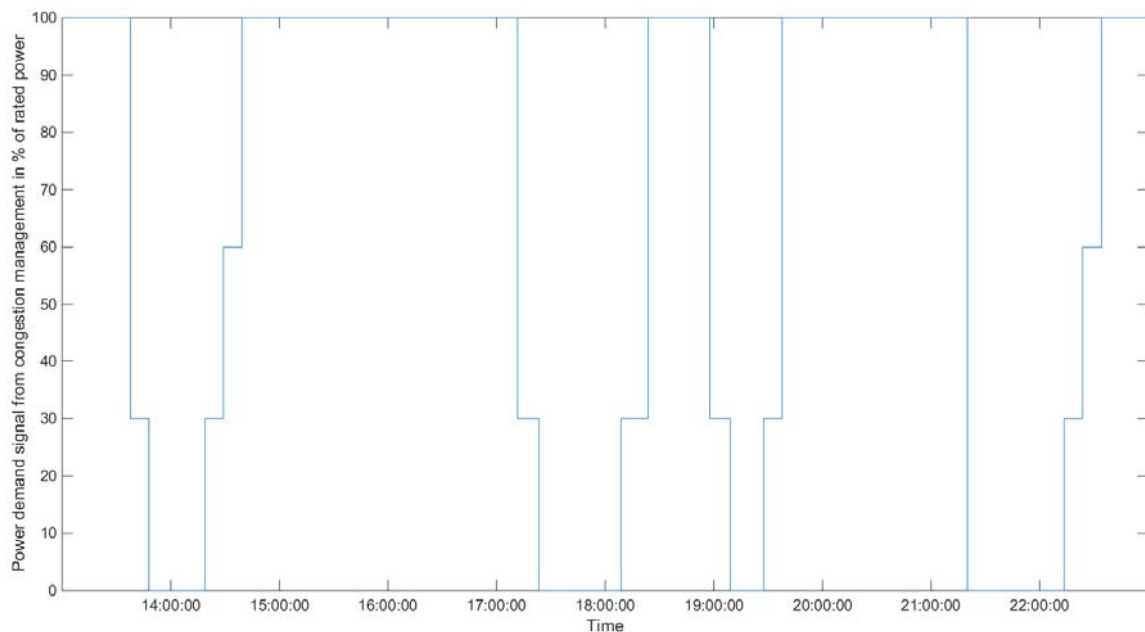


Figure 106: Power demand signal from congestion management; transformer station Strübbel Oct 2015 [17].

Simulation Results

The simulations with the disabled controller show that the E30 can cope even with very short time periods of the signal as shown in Figure 106. The turbine avoids oscillations by limiting the rate at which the power set point is allowed changing. Hence, the rectangular signal shown above is seen as a triangular signal by the speed controller of the turbine (see Figure 109). The slope of the triangular function is relatively flat (0.07 p.u./s). Hence, strong excitations which are close to the identified Eigenfrequencies are avoided. Furthermore, the signal shown in Figure 106 is most of the time either at 100% or at 0% demanded power. However, this is very unlikely when congestion management is to be enhanced. Depending on the actual state of the grid, the power demand signal would rather oscillate between two values, e.g. 0% and 30%. Hence, a new signal was created, that accounts for such a behaviour and is shown in Figure 107.

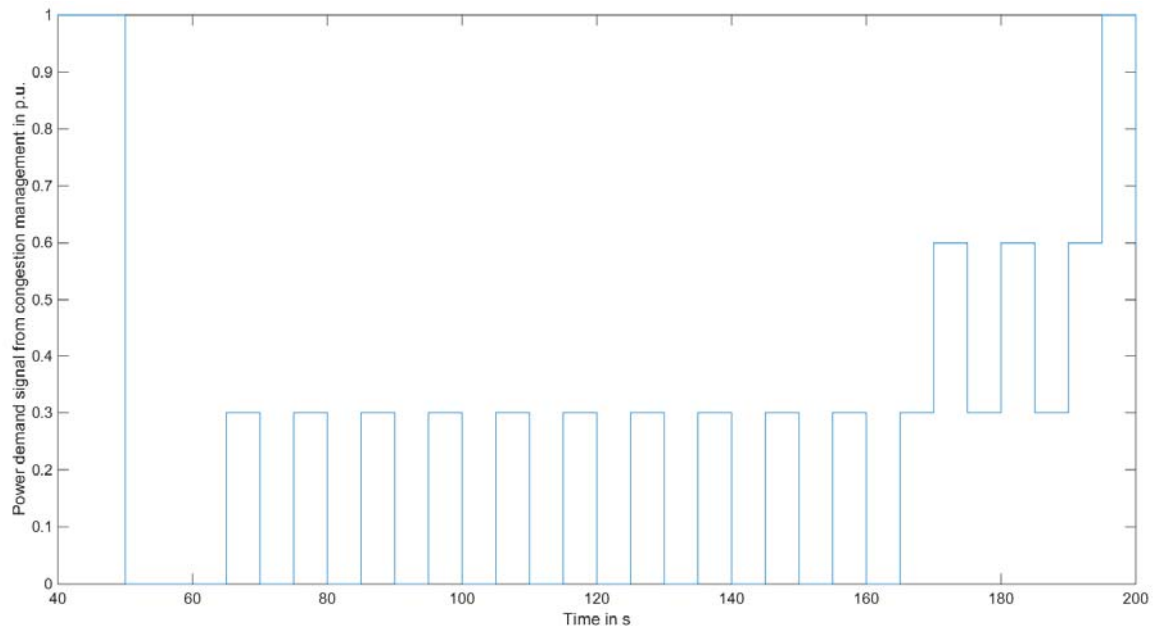


Figure 107: Power demand signal for enhanced congestion management.

Congestion management is more likely during times with high wind. Hence, most of the simulations are done at wind speeds which are sufficient for full load operation. Figure 108 shows the wind speed signal and the pitch angle during such a simulation. The fast changes in the demanded power cause the pitch to change at its maximum rate. Figure 109 shows the different power signals during the same simulation. It shows how the turbine is modifying the congestion management signal in a way that the power demand signal for the control system is a triangular function. As the changes in power demand are very fast the turbine cannot follow the signal to the full extend. Figure 109 furthermore shows that the RMS value of the tower

head accelerations exceeds its allowed value. This should be avoided by enabling the Eisman controller.

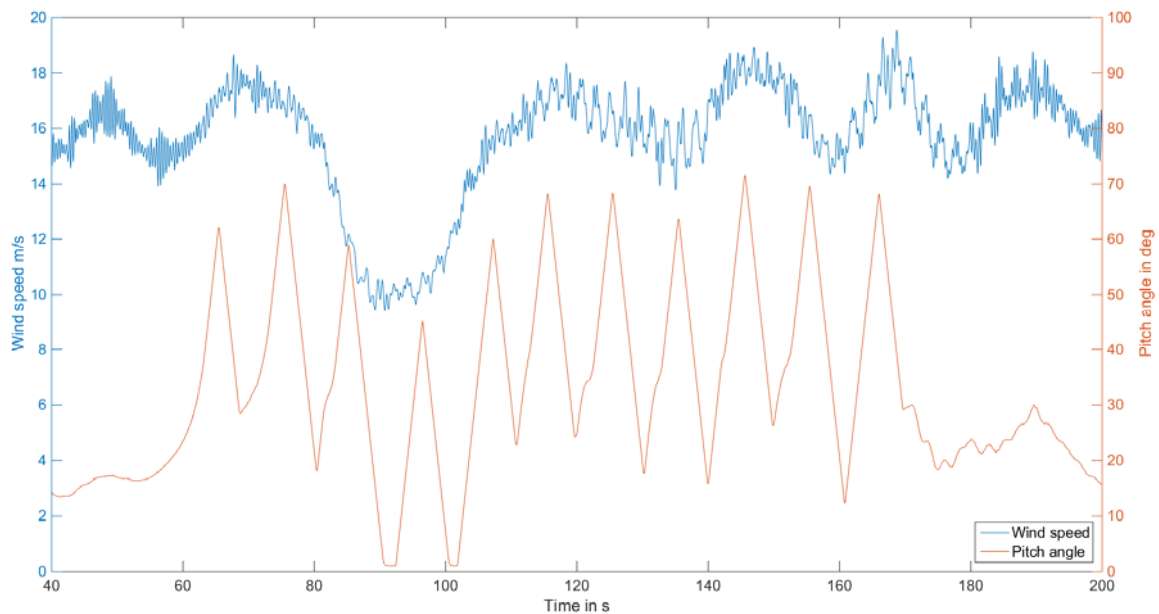


Figure 108: Wind speed and pitch angle during simulation with disabled Eisman controller.

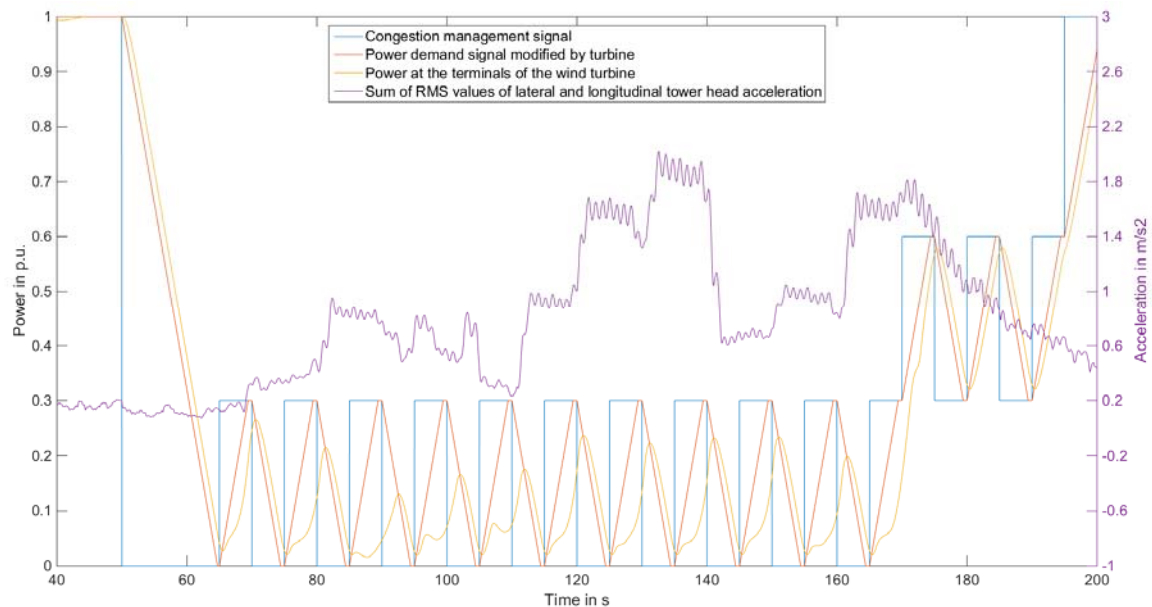


Figure 109: Power signals and tower head acceleration during simulation with disabled Eisman controller.

As expected the critical oscillation can be avoided by changing the k_a parameter of the Eisman controller. Different values for k_a are tested for different wind signals with the Eisman signal shown in Figure 107. The optimum k_a of 0.87 limits the oscillations of the tower head to 1.45 m/s^2 (see Figure 110).

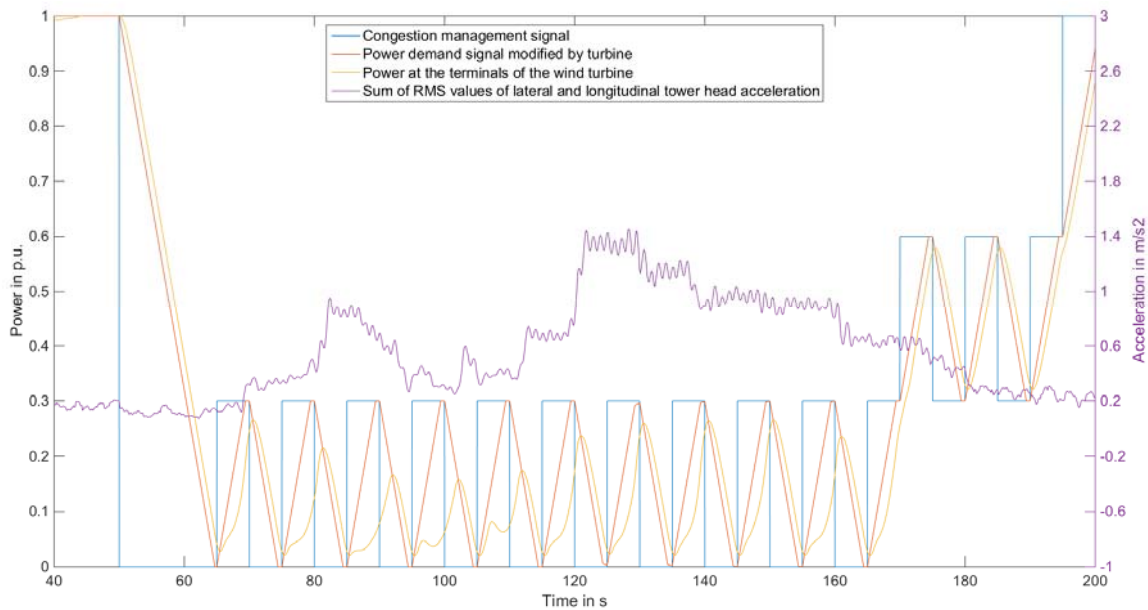


Figure 110: Power signals and tower head acceleration during simulation with enabled Eisman controller.

Figure 111 shows that the power demand signal is only slightly modified at the turning points between positive and negative slopes between 124 s and 140 s. These alternations are sufficient to dampen the oscillations (mainly of the longitudinal acceleration) while causing only small power losses. However, the proposed controller design is only a first draft and has to be tested in additional simulations with changing parameters and additional wind speed and congestion management signals. Although it seems to perform well, it might cause e.g. lateral oscillations under certain circumstances.

Furthermore, it has to be noted that the effect of the enhanced congestion management on the loads of the turbine has not been part of this research project. However, fast changes in the power output and of the pitch angle are very likely to have a negative effect. These must be considered when the change in congestion management is evaluated. These must be researched in a future project.

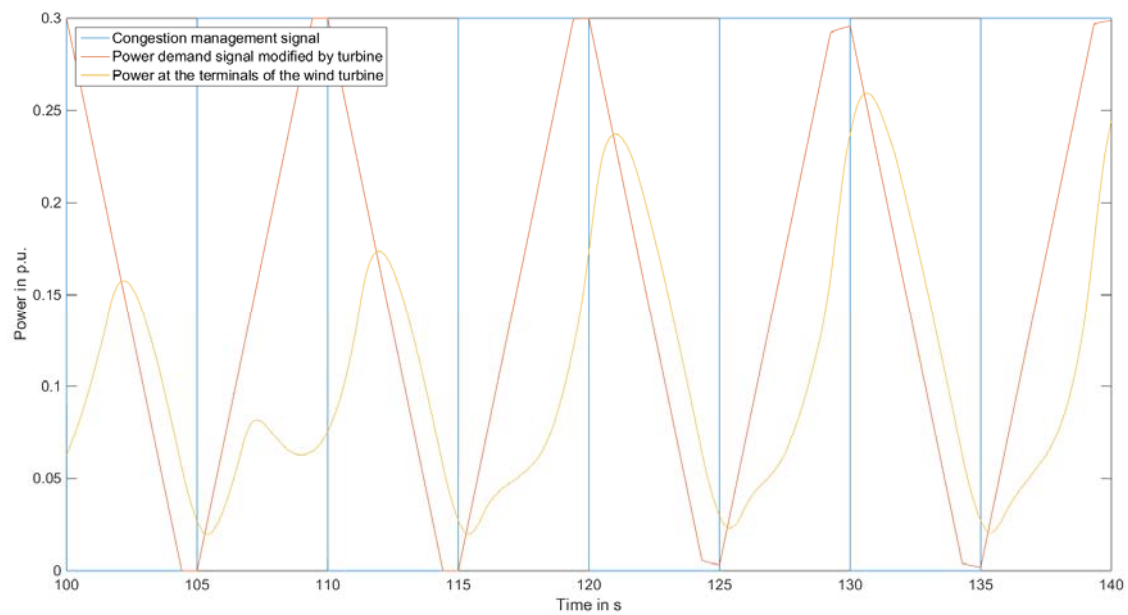


Figure 111: Extract of Figure 110 Detailed view of power signals during simulation with enabled Eisman controller.

References

- [1] J. Bömer, M. Doering, and K. Burges, “Einspeisemanagement in Schleswig-Holstein,” Ministerium für Energiewende, Landwirtschaft, Umwelt und ländliche Räume des Landes Schleswig-Holstein, Kiel, POWDE12992, 2012.
- [2] M. Döring, K. Burges, and R. Kuwahata, “Wind Curtailment - Assessment of Storage Options for Reduction of Yield Losses,” in *Proceedings of the 13th wind integration workshop*, Berlin, 2014, pp. 703 – 714.
- [3] W. Lawrenz, Ed., *CAN system engineering: from theory to practical applications*, 2. ed. London: Springer, 2013.
- [4] E. Schrüfer, *Elektrische Messtechnik: Messung elektrischer und nichtelektrischer Größen ; mit 41 Tabellen*. München: Hanser, 2007.
- [5] A. Kraproth, J. Stamp, E. Reimers, M. Riem, and H. Wiegers, “Abschlussbericht Condition Monitoring am Blatt einer WKA,” Fachhochschule Flensburg, Flensburg, Jan. 2012.
- [6] A. Rivola and M. Troncossi, “Zebra tape identification for the instantaneous angular speed computation and angular resampling of motorbike valve train measurements,” *Mech. Syst. Signal Process.*, vol. 44, no. 1–2, pp. 5–13, Feb. 2014.
- [7] C. Jauch and N. Nussel, “Development of a Contactless Pitch Angle Measurement System,” *Wind Eng.*, vol. 38, no. 6, pp. 621–632, Dec. 2014.
- [8] C. Jauch, “A Simple Wind Model for Fast Wind Farm Simulations,” *Wind Eng.*, vol. 38, no. 5, pp. 523–534, Oct. 2014.
- [9] E. Hau, *Wind turbines: fundamentals, technologies, application, economics*, 3., transl. ed. Berlin: Springer, 2013.
- [10] J. F. Manwell, J. G. McGowan, and A. L. Rogers, *Wind energy explained: theory, design and application*, 2. ed., repr. with cor. Chichester: Wiley, 2011.
- [11] R. Chaaban, “NREL 5-MW reference turbine - CP, CQ, CT Coefficients,” *NREL’s National Wind Technology Center*, 13-Oct-2015. .
- [12] G. Ramtharan, N. Jenkins, O. Anaya-Lara, and E. Bossanyi, “Influence of rotor structural dynamics representations on the electrical transient performance of FSIG and DFIG wind turbines,” *Wind Energy*, vol. 10, no. 4, pp. 293–301, Jul. 2007.
- [13] H. Jäger, R. Mastel, and M. Knaebel, *Technische Schwingungslehre: Grundlagen - Modellbildung - Anwendungen ; mit 74 Aufgaben und 40 Beispielen*, 8., überarb. Aufl. Wiesbaden: Springer Vieweg, 2013.
- [14] P. Sorensen, B. Andresen, J. Fortmann, and P. Pourbeik, “Modular structure of wind turbine models in IEC 61400-27-1,” 2013, pp. 1–5.
- [15] H. Lutz and W. Wendt, *Taschenbuch der Regelungstechnik: mit MATLAB und Simulink*, 10., ergänzte Aufl. Haan-Gruiten: Verl. Europa-Lehrmittel, Nourney, Vollmer, 2014.
- [16] Nexans Schweiz AG, “Niederspannungskabel und Mittelspannungskabel.” 2015.
- [17] Schleswig-Holstein Netz AG, “Einsätze des Einspeisemanagement - Mittelspannung, Hoch- und Höchstspannung, TenneT - Oktober 2015.” Nov-2015.

Appendix

Appendix A

Data sheets of used measurement equipment

Data Logger: Dewetron 2010 + A-D-cards

Main System

DEWE-2010 series PC instrument

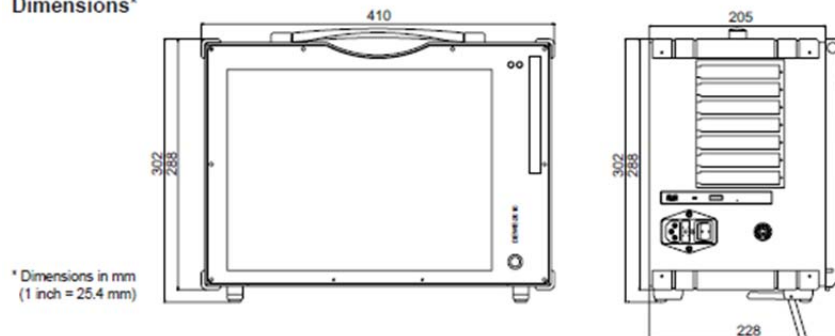
- Portable data acquisition system
- Up to 16 channels with isolation (in conjunction with DEWE-DAQ modules)
- Up to 256 channels with external expansion racks
- A/D converter specs see appendix A



System specifications

	DEWE-2010
Power supply:	<input type="checkbox"/> 300 W AC power supply 'FSP300-601U' <input checked="" type="checkbox"/> AC/DC multi power supply 'NET-202 + Accu' for details see next pages
Operating temperature:	-5 °C to 50 °C (standard)
Storage temperature:	-20 °C to +70 °C
Humidity (operating):	10 % to 80 %, non condensing
	5 % to 95 %, rel. humidity
Vibration:	MIL-STD 810F 514.5 procedure I operating test procedure frequency range: 5 to 200 to 5 Hz; 5 x 12 min each direction displacement amplitude ± 3.5 mm (5 to 8.45 Hz) acceleration amplitude 1 g (8.45 to 92 Hz) displacement amplitude 92 to 113 Hz: ± 0.029 mm acceleration amplitude 1.5 g (113 to 200 Hz)
Shock:	MIL-STD 810F 516.5 procedure I non operating test procedure $\frac{1}{2}$ sinus 11 ms 10 g, 3 shocks positive, 3 shocks negative
Dimensions (W x H x D):	approx. 410 x 288 x 205 mm (16.1 x 11.3 x 8.1 in.)
Weight:	typ. 9.5 kg (19 lbs), depending on configuration

Dimensions*



* Dimensions in mm
(1 inch = 25.4 mm)

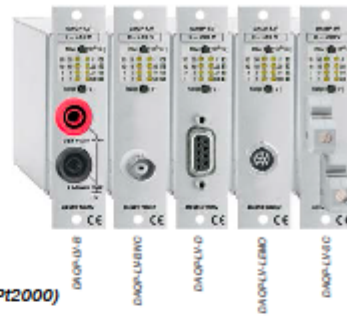
Isolation Amplifiers

DAQP-LV

- Voltage input:
- Current input:
- Bandwidth:
- Isolation:
- IEP®
- RTD
- CHARGE

Isolated low voltage module

12 ranges (10 mV to 50 V)
 ± 20 mA using DAQ-SHUNT-1
 ± 5 A using DAQ-SHUNT-4 or DAQ-SHUNT-5
 300 kHz
 $350 V_{DC}$ (1 kV_{RMS} with banana socket)
 Additional signal input using MSI
 Constant current powered sensors
 (accelerometers, microphones); 12 ranges
 (10 mV to 5 V); requires MSI-V-ACC
 Resistance Temperature Detector (Pt100 to Pt2000)
 9 resistance ranges (8 to 4000 Ω);
 requires MSI-V-RTD
 Charge up to 50000 pC requires MSI-V-CH-50



Module specifications

DAQP-LV	
Input ranges unipolar and bipolar	10 mV, 20 mV, 50 mV, 100 mV, 200 mV, 500 mV, 1 V, 2.5 V, 5 V, 10 V, 25 V, 50 V
Push button selectable ranges	10 mV, 50 mV, 200 mV, 1 V, 5 V, 10 V, 50 V
DC accuracy	Range Accuracy
Bipolar	10 mV to 50 mV ± 0.02 % of reading ± 40 μ V
Unipolar	100 mV to 50 V ± 0.02 % of reading ± 0.05 % of range
	10 mV to 50 mV ± 0.04 % of reading ± 40 μ V
	100 mV to 50 V ± 0.04 % of reading ± 0.05 % of range
Input coupling	DC or AC software selectable (1.5 Hz standard, custom on request down to 0.01 Hz)
Gain linearity	0.01 % of full scale
Gain drift range	Typically 10 ppm/ $^{\circ}$ K (max. 20 ppm/ $^{\circ}$ K)
Offset drift	Uni- and bipolar
10 mV to 200 mV	3 μ V/ $^{\circ}$ K
500 mV to 50 V	10 ppm of Range/ $^{\circ}$ K
Long term stability	100 ppm/sqrt (1000 hrs)
Input resistance	1 MOhm
Bandwidth (-3 dB)	300 kHz
Filter selection	Push button or software
Filters (low pass)	10 Hz, 30 Hz, 100 Hz, 300 Hz, 1 kHz, 3 kHz, 10 kHz, 30 kHz, 100 kHz
Filter characteristics	10 Hz to 100 kHz: Butterworth or Bessel 40 dB/dec (2nd order; ± 1.5 dB @ 10) 300 kHz: Bessel 60 dB/dec (3rd order; 0 to -3 dB @ 300kHz)
Typical SFDR and SNR:	300 kHz bandwidth 100 kHz bandwidth 10 kHz bandwidth
20 mV	SFDR SNR SFDR SNR SFDR SNR
1 V	100 dB 72 dB 98 dB 76 dB 97 dB 84 dB
50 V	102 dB 82 dB 99 dB 93 dB 97 dB 96 dB
	102 dB 82 dB 99 dB 93 dB 97 dB 96 dB
Typical CMRR	10 mV to 1 V range: 2.5 V to 50 V range:
	>100 dB @ 50 Hz 90 dB @ 50 Hz
	>100 dB @ 1 kHz 65 dB @ 1 kHz
	83 dB @ 10 kHz 55 dB @ 10 kHz
Input overvoltage protection	$350 V_{DC}$
Isolation voltage	$350 V_{DC}$ (1 kV _{RMS} with banana connector)
Sensor supply	± 9 V (± 1 %), 12 V (± 5 %), 200 mA resettable fuse protected ⁽¹⁾
Output voltage	± 5 V
Output resistance	<10 Ohm
Maximum output current	5 mA
Output protection	Short to ground for 10 sec.
Power On default settings	Software programmable
Power supply	$\pm 9 V_{DC} \pm 1$ %
Power consumption	0.8 W without sensor supply
RS-485 interface	Yes
TEDS	Hardware support for TEDS (Transducer Electronic Data Sheet)
Supported TEDS chips	DS2406, DS2430A, DS2432, DS2433, DS2431
Supported MSI	MSI-V-ACC; MSI-V-RTD; MSI-V-CH-50

⁽¹⁾ Overall current should not exceed DEWE-30-xx maximum power.

Test & Measurement Solutions

17

Isolation Amplifiers

DAQP-HV

- Input ranges:
- Bandwidth:
- Isolation:
- Signal connection:

Isolated high voltage module

- 7 ranges (± 20 V to ± 1400 V)
- 300 kHz (700 kHz for DAQP-HV-S3)
- 1.8 kV_{RMS} line to line
- 1.4 kV_{RMS} line to ground
- Banana sockets
- Screw terminals



Module specifications



	DAQP-HV
Input ranges unipolar and bipolar	20 V, 50 V, 100 V, 200 V, 400 V, 800 V, 1400 V
DC accuracy	± 0.05 % of reading ± 40 mV
20 V and 50 V	± 0.05 % of reading ± 0.05 % of range
100 V to 1400 V	
Gain linearity	0.03 %
Gain drift range	Typically 20 ppm/*K (max. 50 ppm/*K)
Offset drift	
20 V to 100 V	typical 0.5 mV/*K max. 4 mV/*K
200 V to 1400 V	typical 5 ppm/*K max. 20 ppm of Range/*K
Long term stability	100 ppm/sqrt (1000 hrs)
Input resistance	10 MOhm
-3 dB Bandwidth (DAQP-HV)	300 kHz ⁽¹⁾
-3 dB Bandwidth (DAQP-HV-S3)	700 kHz ⁽²⁾
Filter selection	Push button or software
Filter (lowpass)	10 Hz, 30 Hz, 100 Hz, 300 Hz, 1 kHz, 3 kHz, 10 kHz, 30 kHz, 100 kHz
Filter characteristics	10 Hz to 100 kHz: Butterworth or Bessel 40 dB/dec (2nd order; ± 1.5 dB @ 10) 300 kHz: Bessel 60 dB/dec (3rd order; 0 to -3 dB @ 300kHz)
Typical SFDR and SNR	
	300 kHz 100 kHz 10 kHz
	SFDR SNR SFDR SNR SFDR SNR
50 V	98 76 101 81 dB 108 90 dB
200 V	98 84 101 89 dB 108 91 dB
1400 V	98 86 102 91 dB 107 92 dB
Typical CMRR	>80 dB @ 50 Hz 70 dB @ 400 Hz 60 dB @ 1 kHz 48 dB @ 10 kHz
Isolation voltage	Line to Ground 1.4 kVrms Line to Line 1.8 kVrms
Protection	CAT III 600 CAT IV 300
Surge (1.2/50)	± 4000 V
Burst (5 kHz)	± 4000 V
Output voltage	± 5 V
Output resistance	<10 Ohm
Output current	5 mA
Output protection	Short to ground for 10 sec.
Power supply	± 9 V _{DC} ± 1 %
Power consumption	0.7 W
Power On default settings	Software programmable
Interface	RS-485

⁽¹⁾ 300 kHz exclusively for Bessel filter characteristic

⁽²⁾ 700 kHz exclusively for Bessel filter characteristic

Data Logger: Wilmers ndl research 485

Technical Data

Model	wilog303	wilog306	NDL485 basic	NDL485 research
PartNo.	0123	0131	0102	0103
				
Measuring Inputs				
Digital inputs	3	3	6	6
Analogue inputs	3	6	6	6
Additional inputs	-	-	via INPUT Modules (8 x AIN/DIN per module)	
Serial inputs	-	-	RS485, half-duplex, optional RS232	
Digital Measuring Inputs				
Measuring range	frequency 2 .. 1,500 Hz counter 0 .. 1 Hz		frequency 0 .. 2,000 Hz counter 0 .. 2,000 Hz status HI / LO	
Resolution	0.01 Hz		0.01 Hz	
Accuracy	frequency $\pm 0.1\%$ counter ± 1 pulse		frequency $\pm 0.1\%$ counter ± 1 pulse	
Signal level	HI = >3.0 V LO = <0.7 V or potential free switch closure		HI = >2.5 V LO = <0.7 V or potential free switch closure	
Input impedance	>10 k Ω		>20 k Ω	
Analogue Measuring Inputs				
Measuring range	0 .. 6 V		0 .. 10 V	
Resolution	12 Bit (1.5 mV)		16 Bit (0.2 mV)	
Accuracy	$\pm 0.1\%$ of reading ± 1.5 mV		$\pm 0.1\%$ of reading ± 1 mV	
Input impedance	300 k Ω		1 M Ω	

Measuring Functions	wilog303	wilog306	NDL485 basic	NDL485 research
Measuring interval	1 s .. 24 h		1 s .. 24 h	0.1 s .. 24 h
Statistic interval	1 s .. 24 h		1 s .. 24 h	0.1 s .. 24 h
Statistic functions	mean value (arithmetic + vectorial), standard deviation (arithmetic + vectorial), minimum, maximum		mean value (arithm. + vectorial), standard deviation (arithm. + vectorial), minimum, maximum, sum	mean value (arithm. + vectorial), standard deviation (arithm. + vectorial), minimum, maximum, sum, median
Data memory for statistic time series	510 kB (up to 240,000 values) non-volatile ring buffer		32 MB, expandable to up to 1 GB, non-volatile ring buffer	128 MB, expandable to up to 1 GB, non-volatile ring buffer
Data memory for samples	-		32 MB non-volatile ring buffer	
Communication				
Data interface	RS232 serial interface, 9,600 baud		RS232 serial interface, 1,200 .. 115,200 baud, RS485 serial interface, half-duplex, 1,200 .. 115,200 baud, Ethernet interface (LAN), 10 MBit/s, optional MODBUS TCP protocol	
Remote data transmission	GSM, fixed network modem, satellite modem		GSM, GPRS, DSL, ISDN router	
Automatical data transmission	-		via eMail	via eMail and FTP
Internet integration	-		via GPRS or DSL	
User interface	PC software witerm		web interface, Internet browser	
Graphical data display	-		-	realtime diagrams of measured values, optional custom speci- fic graphical display
Display	LCD displays measured values, measurement parameters and power supply voltage		-	
Power Supply				
External power supply	9 .. 24 VAC/DC		5 .. 24 VDC	
Internal power supply	3 alkaline batteries LR20 Mono 1.5 V		-	
Current consumption	internal 1 .. 5 mA, external 5 mA		typ. 600 mW (50 mA @ 12 V)	
Sensor excitation	5 VDC switched, max. 20 mA		5 .. 24 VDC switched, max. 500 mA	
Switching outputs	1 output for time-scheduled operation of a GSM modem (TC35i)		4 switching outputs, max. 300 mA, HI = supply voltage, LO = 0 V, time or event triggered	
Mechanics and Operating Conditions				
Casing	200 x 120 x 90 mm, IP65 polycarbonate		65 x 105 x 127 mm, IP20 top-hat rail housing, anodized aluminium	
Connections	circular connectors IP67		terminal strips, connectors	
Temperature range	-40 .. +70 °C		-40 .. +70 °C	

© 2006-08-21 • All rights reserved. Technical data may subject to change without notice.

Ultra-sonic anemometer: Thies Clima Ultrasonic Anemometer 2D

0255



Ultraschallanemometer 2D



Beschreibung

Sensor zur trägheitsfreien Messung der horizontalen Komponenten der Windgeschwindigkeit und Windrichtung, sowie der virtuellen Temperatur. Der Sensor enthält keine beweglichen Teile und ist daher wartungsfrei.

Zwei gegenüberstehende Paare von Ultraschallwandlern erfassen die horizontalen Komponenten des Windvektors. Ein Prozessor wandelt die Rohsignale in analoge Signale um. Eine serielle RS422-Schnittstelle ermöglicht den direkten Anschluß an einen PC oder eine Steuerung.

Eine eingebaute elektronisch geregelte Heizung verhindert eine Vereisung des Sensors im Winterbetrieb.

Technische Daten

Sensor

Meßelement..... Ultraschallwandler
Datenaufbereitung..... Mikroprozessor

Ausgänge

Analog 0..65 m/s = 0/2..10 V oder 0/4..20 mA
0..360° = 0/2..10 V oder 0/4..20 mA
Digital RS422, 1200..19200 baud

Auflösung

Windgeschwindigkeit..... 0,1 m/s
Windrichtung 1°
Virtuelle Temperatur 0,1 °C

Genauigkeit

Windgeschwindigkeit..... 0..5 m/s \pm 0,1 m/s
> 5 m/s \pm (2% vom Meßwert \pm 0,1 m/s)
Windrichtung \pm 1°
Virtuelle Temperatur \pm 0,5 °C
Ansprechwindgeschwindigkeit 0,1 m/s

Wilmer's Meßtechnik • Hirschgraben 24 • D-22089 Hamburg • Germany • www.wilmer's.com

Interne Abtastrate..... 400 Hz bei 25 °C

Ausgaberate

Analog 100 ms

Digital 100 ms..25 s, vom Anwender einstellbar

Stromversorgung

Versorgungsspannung 12..24 VAC/DC \pm 10%

Leistungsbedarf 3 W

Heizung

Heizungsleistung..... Max. 70 W, elektronisch geregelt

Versorgungsspannung 24 VAC/DC \pm 15%

Stromverbrauch..... Max. 3 A

Gehäuse

Material..... Eloxiertes Aluminium / rostfreier Edelstahl

Schutzart..... IP 65

Abmessungen 300 x 300 x 500 mm

Gewicht..... 2,5 kg

Befestigung..... Montage auf einem 1 1/2" DIN-Rohr mit
ø49 mm Außendurchmesser und > ø35 mm
Innendurchmesser

Elektrischer Anschluß

Stecker (am Sensor)..... 16-poliger Rundsteckverbinder

Umgebungsbedingungen

Umgebungstemperatur..... -40..+70 °C

Relative Luftfeuchte 0..100%

Maximale Windgeschwindigkeit..... 65 m/s



**Wilmers
Meßtechnik**

Hirschgraben 24
D-22089 Hamburg • Germany

Tel.: +49(0)40-75 66 08 98
Fax: +49(0)40-75 66 08 99
eMail: info@wilmers.com
www.wilmers.com

Thermo Hygro Sensor: Wilmers

0538



Thermo Hygro Sensor



Description

Precise low power sensor for the measurement of temperature and relative humidity of the ambient air.

A radiation shield protects the sensor against rain and solar radiation.

Technical Data

Sensor

Temperature

Sensing element	Pt 100, according to IEC 751
Transducer	Electronical transducer with voltage output
Output signal.....	-40..+60 °C = 0..5 V
Accuracy.....	± 0.2 °C at 20 °C, ± 0.5 °C at -40..+60 °C
Output load.....	> 10 kΩ

Relative Humidity

Sensing element	Capacitive sensor
Transducer	Electronical transducer with voltage output
Output signal.....	0..100% RH = 0..5 V
Accuracy.....	0..90% RH ± 2% RH 90..100% RH ± 3% RH
Output load.....	> 10 kΩ

Power Supply

Supply voltage	7..30 VDC
Current consumption	typ. 1.3 mA max.

Wilmers Messtechnik GmbH • Hammer Steindamm 35 • D-22089 Hamburg • Germany • www.wilmers.com

Barometric sensor (no English version available)

0619



Luftdrucksensor economy



Beschreibung

Einfacher und robuster Sensor zur Messung der barometrischen Luftdrucks.

Eine piezoelektrisches MeBelement wird durch Druckeinwirkung verformt. Das Signal wird von einem Meßumformer in eine linear vom Luftdruck abhängige Spannung umgewandelt.

Technische Daten

Sensor

MeBelement.....	Piezokristall
Meßumformer.....	Vorverstärker mit Spannungsausgang
Ausgangssignal.....	800..1100 mbar = 0..5 V
Lastwiderstand am Ausgang.....	> 10 kOhm

Genauigkeit

Typische Genauigkeit.....	± 1,1 mbar bei 25 °C
	± 2,3 mbar bei -10..+60 °C
Maximale Ungenauigkeit.....	± 1,5 mbar bei 25 °C
	± 12 mbar bei -10..+60 °C

Stromversorgung

Betriebsspannung.....	8..24 VDC
Stromverbrauch.....	10 mA
Einstellzeit.....	100 ms

Gehäuse

Material.....	Kunststoff
Schutzart.....	IP 54
Abmessungen.....	65 x 70 x 37 mm
Gewicht.....	0,1 kg

Wilmer's Meßtechnik • Hirschgraben 24 • D-22089 Hamburg • Germany • www.wilmer's.com

Elektrischer Anschluß

Kabel..... 3 x 0,5 mm²
Anschlüsse Aderendhülsen

Adernbelegung

weiß..... (+) Versorgungsspannung
braun Masse
grün Ausgangssignal

Umgebungsbedingungen

Umgebungstemperatur..... -40..+85 °C
Relative Feuchte 0..100%

Kennlinie für wilog303/306

Bei Verwendung des Sensors mit den Datenloggern wilog303 und wilog306 ist die folgende Kennlinie einzugeben.

Beispiel: Anschluß an den Analogeingang f

pBaro : mean = 800 + 60 * f



**Wilmers
Meßtechnik**

Hirschgraben 24
D-22089 Hamburg • Germany

Tel.: +49(0)40-75 66 08 98
Fax: +49(0)40-75 66 08 99
eMail: info@wilmers.com
www.wilmers.com

Irrtümer und technische Änderungen vorbehalten.

2003-07-30

Wilmers Meßtechnik • Hirschgraben 24 • D-22089 Hamburg • Germany • www.wilmers.com

Incremental counter /CAN bus: imc Messtechnik Cansas – INC4

INC4

Datasheet Version 1.4 (4 incremental counter inputs)

Parameter	Value (typ. / max.)	Remarks
Inputs	4 + 1 (9 tracks)	4 channels with 2 tracks (X, Y) each 1 index channel all fully conditioned inputs isolated from CAN-Bus and supply, but not mutually.
Measurement modes:	displacement, angle, events, time, frequency, velocity, RPMs	
Sampling rate (CAN output)	1 kHz / channel (max.)	
Time resolution of measurement	33 ns	counter frequency 32 MHz (primary sampling rate)
frequency stability	<100 ppm	
deterioration	<±5 ppm / year	
Resolution of data	16 bits	
Input configuration	differential	
Input impedance	100 kΩ	
Switching threshold	-8 V to +10 V	globally selectable in 0.1 V steps
Hysteresis	0,3 V to 4 V	globally selectable in 0.1 V steps
Input voltage range (differential)	±10 V ±30 V	linear range maximum, outside of linear range: max. non-linearity uncertainty: 300 ns
Common mode input voltage	max. ±30 V	
Analog bandwidth	500 kHz	-3 dB (full power)
Analog filter	bypass (without filter), 20 kHz, 2 kHz, 200 Hz	adjustable (globally for all channels) Butterworth, 2nd order
CMRR	70 dB (typ.), 50 dB (min.) 60 dB (typ.), 50 dB (min.)	DC, 50 Hz 10 kHz
Gain uncertainty	< 1 %	23°C
Offset	< 1 %	23°C
frequency stability	< 100 ppm	deterioration <±5 ppm / year
CAN-Bus	defined by ISO 11898	
CANopen® mode	"CiA® DS 301 V4.0.2" and "CiA® DS 404V1.2" supports 4 PDOs in INT16, INT32, and FLOAT	
isolation:		to CHASSIS
CAN-Bus	±80 V	nominal; testing: 300 V (10 s)
power supply input	±80 V	nominal; testing: 300 V (10 s)
analog input	no isolation	analog reference ground: CHASSIS
Overvoltage protection	±80 V	long-term
Sensor supply	+5 V ±200 mA, 20 mA	Reference: GND
Supply voltages	10 V to 50 V DC	
Sensor supply voltage at CANSAS-L-INC4-V-SUPPLY	+2.5 V to +24 V	
Power consumption:	4 W (typ.)	12 V supply, 23°C
Operating temperature	-30°C to 85°C	
Dimensions (W x H x D)	35 x 111 x 90 mm 35 x 111 x 145 mm 41 x 128 x 145 mm 38 x 112.5 x 152 mm	CANSAS-INC4 CANSAS-L-INC4, -L-INC4-V CANSAS-C-INC4 (8TE) CANSAS-SL-INC4-L

Analog measurements / CAN bus: imc Messtechnik Cansas – C12

CANSAS-C12 technical specifications (12 analog inputs)

Parameter	Value (typ. / max)		Test conditions
Inputs	12		6 channels on each DSUB-15 socket
Measurement modes:	voltage voltage with divider current thermocouples PT100		configurable in blocks of 6 Standard-plug (CAN/DSUB-U6) Divider-plug (CAN/DSUB-U6D) Shunt-plug (CAN/DSUB-46) Thermo-plug (CAN/DSUB-T6) PT100-plug (CAN/DSUB-PT): 4 channels with contacts for 4-wire connection or voltage plug (CAN/DSUB-U) 6 channels without contacts for 4-wire connection.
Sampling rate	500 Hz		
Resolution	16 Bit		
Voltage input ranges:	$\pm 2V$, $\pm 500mV$, $\pm 100mV$ $\pm 50V$, $\pm 10V$		with standard plug with divider plug (asymmetric, referenced to ground)
Current input ranges:	$\pm 40mA$, $\pm 10mA$, $\pm 2mA$		with shunt plug (50 Ohm)
Thermocouple input ranges	$-200 \dots +1200^{\circ}C$		with thermo-plug, all common types
PT100 input ranges	$-250 \dots +900^{\circ}C$		with PT100-plug, $I = 0.3mA$
Isolation:	analog inputs CAN-bus power supply input		to enclosure (CHASSIS)
Channel isolation mutually:	$\pm 150V$ $\pm 150V$ $\pm 150V$		max. <i>difference</i> between two input pins of any channels, (for C12 with divider: between [-]inputs) ensuring specified precision ensuring no damage
Surge protection	$\pm 40V$ (high-Ohms during surge)		differential input voltage of a channel (long-term)
Input configuration	DC, differential		isolated from: enclosure, supply and CAN-bus
Input impedance (static)	10 M Ω 500 k Ω 50 Ω		voltage, thermo voltage with divider current
Input current static dynamic	4 nA (Type.)	40 nA (max.) 100 nA (max.)	after transients average dynamic input current
Gain error:	< 0.05 % < 0.15 % < 0.15 %		23 $^{\circ}C$ with voltage plug with divider plug shunt plug

CANSAS-C12

Gain drift	< 75 ppm / K		
Offset error	< 0.02 %		throughout entire temperature range
Temperature error	< 1 K		sensor: Type K at 20 °C throughout entire temperature range
Noise	50 μ V pk-pk 25 mV pk-pk	7 μ V rms 7 mV rms	range ± 100 mV, $R_q = 50\Omega$, sampling rate 2 ms range ± 10 V (divider)
CMRR / IMR	> 100 dB (50 Hz)		Common-Mode reference: enclosure (CHASSIS) All other channels: CHASSIS
Supply voltage	9 .. 36 V (DC)		
Power consumption::	< 2.5W (typ.)	< 3.0W (max.)	12V, throughout entire temperature range
Ambient temperature range	-30 °C ... +65 °C		
Module-internal temperature	-40 °C ... +85 °C		
Dimensions	111 x 90 x 35 mm (W x H x D)		
Weight	300 g		
Contacts	2 x DSUB-15 2 x DSUB-9 PHOENIX (MC 1,5/4STF -3,81)		inputs CAN (in / out) supply

RS 232 / CAN bus: condalo STC


condalo
 ELEKTRONIK & MECHATRONIK

STC (Serial To CAN)



Eigenschaften:

- **RS232 To CAN / RS232 Gateway (Datenlogger / Automobil / PC)**
- **Pegel und Polaritätsanpassung für Systeme ohne RS232 Treiber**
- **Messwertaufnehmer mit CAN oder RS232 Schnittstelle**
- **Analogwert- Eingabe in CAN-Systeme**
- **CAN-RS232-Dongle**
- **zyklisches senden von CAN-Nachrichten**

Technische Daten:


Versorgung:	7V - 30V DC, max. 46mA
Größe:	63mm x 17mm x 33mm
Temperaturbereich:	-40°C ... +85°C
Gewicht:	22g
Schnittstellen:	1 RS232 (1.x und 2.x), 1 CAN (2.0A und 2.0B), 2 Analog (10Bit, max. 25V) 1 Digital (Schwelle 4V, max 50V) 1 RS232 (Konfiguration)

Lieferumfang:

- **STC**
- **Manual**
- **Software für die Konfiguration**


condalo GmbH
 Kohlstatt 3
 86706 Lichtenau
 08450 / 9264 - 0
info@condalo.de
www.condalo.de

Distance laser sensor of pitch angle measurement system: Leuze ODSL 9





ODSL 9

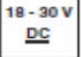


Optical laser distance sensors






en 03-2012/11 50112185







50 ... 450mm

- Large measurement range
- Reflection-independent distance information
- Configuration via PG/LC display and control buttons
- Measurement value is indicated in mm on LC display
- Configurable measure mode and measurement range
- M12 turning connector input (pin 2) for deactivating the laser, triggering, offset correction, reference measurement or teach-in
- M12 turning connector
- Fieldbus connection (e.g. PROFINET, PROFIBUS, ...) with a MA2xxi modular interfacing unit for ODSL 9/D26...

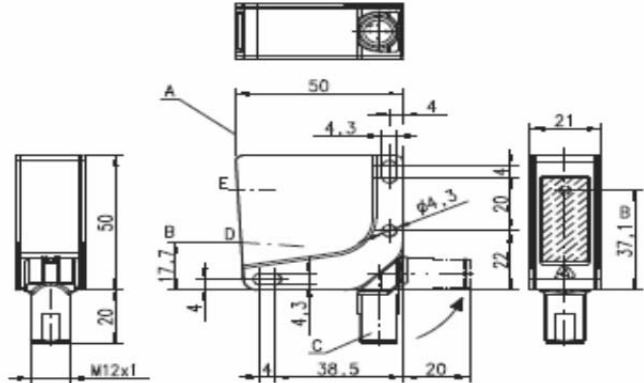




Accessories:
(available separately)

- Mounting systems
- Configuration software
- Cable with M12 connector (K-D ...)
- Connection cable for MA2xxi (K-DS M12A-MA-5P-3m-S-PUR, Part no. 50115049)

We reserve the right to make changes • DS-ODSL9450_en_50112185.fm

Dimensioned drawing



A Reference edge for the measurement
B Optical axis
C Device plug M12
D Receiver
E Transmitter
F LCD display
G Indicator diode yellow
H Indicator diode green
J Control buttons

Electrical connection

<p>ODSL 9/56...</p> <table border="0"> <tr><td>10-30V DC +</td><td>1</td><td>br/BN</td></tr> <tr><td>In</td><td>2</td><td>ws/WH</td></tr> <tr><td>GND</td><td>3</td><td>bl/BU</td></tr> <tr><td>Q1</td><td>4</td><td>sw/BK</td></tr> <tr><td>Q2</td><td>5</td><td>gr/GY</td></tr> </table>	10-30V DC +	1	br/BN	In	2	ws/WH	GND	3	bl/BU	Q1	4	sw/BK	Q2	5	gr/GY	<p>ODSL 9/D6...</p> <table border="0"> <tr><td>18-30V DC +</td><td>1</td><td>br/BN</td></tr> <tr><td>In</td><td>2</td><td>ws/WH</td></tr> <tr><td>GND</td><td>3</td><td>bl/BU</td></tr> <tr><td>4-20mA</td><td>4</td><td>sw/BK</td></tr> <tr><td></td><td>5</td><td>gr/GY</td></tr> </table>	18-30V DC +	1	br/BN	In	2	ws/WH	GND	3	bl/BU	4-20mA	4	sw/BK		5	gr/GY	<p>ODSL 9/D26...</p> <table border="0"> <tr><td>10-30V DC +</td><td>1</td><td>br/BN</td></tr> <tr><td>RXD</td><td>2</td><td>ws/WH</td></tr> <tr><td>GND</td><td>3</td><td>bl/BU</td></tr> <tr><td>TXD</td><td>4</td><td>sw/BK</td></tr> <tr><td></td><td>5</td><td>gr/GY</td></tr> </table>	10-30V DC +	1	br/BN	RXD	2	ws/WH	GND	3	bl/BU	TXD	4	sw/BK		5	gr/GY	<p>ODSL 9/D36...</p> <table border="0"> <tr><td>10-30V DC +</td><td>1</td><td>br/BN</td></tr> <tr><td>TX-</td><td>2</td><td>ws/WH</td></tr> <tr><td>GND</td><td>3</td><td>bl/BU</td></tr> <tr><td>TX+</td><td>4</td><td>sw/BK</td></tr> <tr><td></td><td>5</td><td>gr/GY</td></tr> </table>	10-30V DC +	1	br/BN	TX-	2	ws/WH	GND	3	bl/BU	TX+	4	sw/BK		5	gr/GY
10-30V DC +	1	br/BN																																																													
In	2	ws/WH																																																													
GND	3	bl/BU																																																													
Q1	4	sw/BK																																																													
Q2	5	gr/GY																																																													
18-30V DC +	1	br/BN																																																													
In	2	ws/WH																																																													
GND	3	bl/BU																																																													
4-20mA	4	sw/BK																																																													
	5	gr/GY																																																													
10-30V DC +	1	br/BN																																																													
RXD	2	ws/WH																																																													
GND	3	bl/BU																																																													
TXD	4	sw/BK																																																													
	5	gr/GY																																																													
10-30V DC +	1	br/BN																																																													
TX-	2	ws/WH																																																													
GND	3	bl/BU																																																													
TX+	4	sw/BK																																																													
	5	gr/GY																																																													
<p>ODSL 9/V6...</p> <table border="0"> <tr><td>18-30V DC +</td><td>1</td><td>br/BN</td></tr> <tr><td>In</td><td>2</td><td>ws/WH</td></tr> <tr><td>GND</td><td>3</td><td>bl/BU</td></tr> <tr><td>1-10V</td><td>4</td><td>sw/BK</td></tr> <tr><td></td><td>5</td><td>gr/GY</td></tr> </table>	18-30V DC +	1	br/BN	In	2	ws/WH	GND	3	bl/BU	1-10V	4	sw/BK		5	gr/GY	<p>ODSL 9/V56...</p> <table border="0"> <tr><td>18-30V DC +</td><td>1</td><td>br/BN</td></tr> <tr><td>TX-</td><td>2</td><td>ws/WH</td></tr> <tr><td>GND</td><td>3</td><td>bl/BU</td></tr> <tr><td>TX+</td><td>4</td><td>sw/BK</td></tr> <tr><td>1-10V</td><td>5</td><td>gr/GY</td></tr> </table>	18-30V DC +	1	br/BN	TX-	2	ws/WH	GND	3	bl/BU	TX+	4	sw/BK	1-10V	5	gr/GY																																
18-30V DC +	1	br/BN																																																													
In	2	ws/WH																																																													
GND	3	bl/BU																																																													
1-10V	4	sw/BK																																																													
	5	gr/GY																																																													
18-30V DC +	1	br/BN																																																													
TX-	2	ws/WH																																																													
GND	3	bl/BU																																																													
TX+	4	sw/BK																																																													
1-10V	5	gr/GY																																																													

Leuze electronic GmbH + Co. KG
info@leuze.de • www.leuze.com

In der Braike 1 D-73277 Owen Tel. +49 (0) 7021 573-0

ODSL 9/...450...- 03

Leuze electronic

ODSL 9

Specifications

Optical data	
Measurement range ¹⁾	50 ... 450 mm
Resolution	0.1 mm
Light source	laser
Wavelength	655 nm
Light spot	divergent, 1x1 mm ² at 450 mm
Laser warning notice	see remarks
Error limits (relative to measurement distance)	
Absolute measurement accuracy ¹⁾	± 1%
Repeatability ²⁾	± 0.5%
B/W detection thresh. (6 ... 90% rem.)	≤ 0.5%
Temperature compensation	yes ³⁾
Timing	
Measurement time	2 ms ¹⁾
Response time	≤ 6 ms
Delay before start-up	≤ 300 ms
Electrical data	
Operating voltage U _B ...C6/C66/V6/V66	18 ... 30 VDC (incl. residual ripple)
...D26/D36/V66	10 ... 30 VDC (incl. residual ripple)
Residual ripple	≤ 15% of U _B
Open-circuit current	≤ 180 mA
Switching output	push-pull switching output ⁴⁾ , PNP light switching, NPN dark switching
Signal voltage high/low	≥ (U _B - 2 V) ≤ 2 V
Analogue output	...V6/V66 voltage 1 ... 10 V / 0 ... 10 V / 1 ... 5 V / 0 ... 5 V, R _L ≥ 2 kΩ
Serial interface	...C6/C66 current 4 ... 20 mA, R _L ≤ 500 Ω
Transmission protocol	...D26/D36 RS 232/RS 485, 9600 ... 57600 Bd, 1 start bit, 8 data bits, 1 stop bit, no parity 14 bit, 16 bit, ASCII, Remote Control
Indicators	
Green LED	continuous light flashing off
Yellow LED	continuous light flashing off
Mechanical data	
Housing	plastic
Optics cover	glass
Weight	approx. 50 g
Connection type	M12 connector, 5-pin
Environmental data	
Ambient temp. (operation/storage)	-20 °C ... +50 °C / -30 °C ... +70 °C
Protective circuit ⁵⁾	1, 2, 3
VDE safety class ⁶⁾	II, all-insulated
Protection class	IP 67
Laser class	2 (according to EN 60825-1 and 21 CFR 1040.10 with Laser Notice No. 50)
Standards applied	IEC 60947-5-2

- 1) Luminosity coefficient 6% ... 90%, complete measurement range, "Standard" operating mode, at 20 °C, medium range of U_B, measurement object ≥ 50x50 mm²
2) Same object, identical environmental conditions, measurement object ≥ 50x50 mm²
3) Typ. ± 0.02 %/K
4) The push-pull switching outputs must not be connected in parallel
5) 1=transient protection, 2=polarity reversal protection, 3=short circuit protection for all outputs
6) Rating voltage 50VAC

Tables

Diagrams

Remarks

- Measurement time depends on the reflectivity of the measurement object and on the measurement mode.
- Approved purpose:**
This product may only be used by qualified personnel and must only be used for the approved purpose. This sensor is not a safety sensor and is not to be used for the protection of persons.

Order guide

	Designation	Part No.
Analog current output		
1 teachable push/pull output	ODSL 9/C6-450-S12	50111157
2 push/pull outputs	ODSL 9/C66-450-S12	50111161
Analog voltage output		
1 teachable push/pull output	ODSL 9/V6-450-S12	50111158
2 push/pull outputs	ODSL 9/V66-450-S12	50111162
Serial digital output		
RS 232, 1 push/pull output	ODSL 9/D26-450-S12	50111159
RS 485, 1 push/pull output	ODSL 9/D36-450-S12	50111160
Only switching outputs		
2 teachable push/pull outputs	ODSL 9/66-450-S12	50111163

ODSL 9/...450...- 03

2012/11

Speed sensors: Leuze KRTM 20

Leuze electronic

KRTM 20

High Resolution Multicolor Contrast Scanner



12mm
20mm
50mm



- Static teach-in
- RGB transmitter
- Response time analog/digital (10µs/10µs or 10µs/20µs)
- Digital switching frequency 50kHz or 25kHz
- Resolution of 70 gray levels at the digital output
- Resolution of 400 gray levels at the analog output
- Analog output 1 ... 10mA
- Changeover to the switching threshold
- Changeover to the analysis depth
- L/D switching
- Pulse stretching

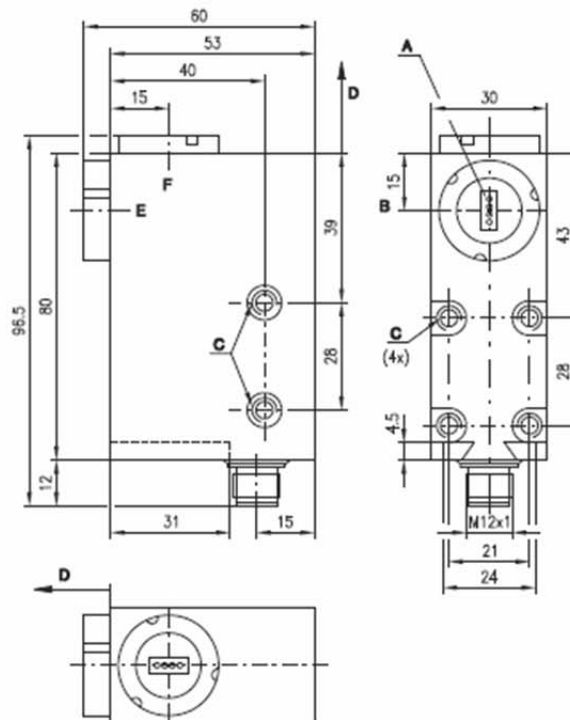


Accessories:

(available separately)

- M12 connectors, 5-pin (KD ...)
- Ready-made cables (K-D ...)
- Interchangeable objectives
- Tool for changing objectives

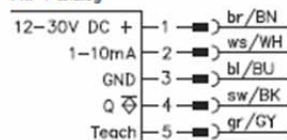
Dimensioned drawing



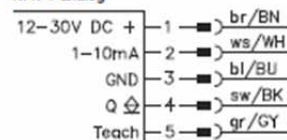
- A Light spot orientation vertical
- B Optical axis
- C M5/5.5mm deep
- D Scanning range
- E Front
- F Head

Electrical connection

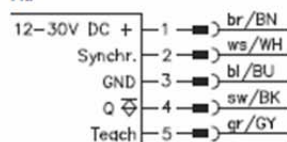
PNP + analog



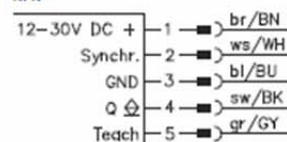
NPN + analog



PNP



NPN



Leuze electronic GmbH + Co. KG
info@leuze.com • www.leuze.com

In der Braike 1 D-73277 Owen Tel. +49 (0) 7021 573-0

KRTM 20... HR stat. Teach - 03

Leuze electronic

KRTM 20

Specifications

Optical data

Scanning range with objective 1 ¹⁾	12 mm ± 1 mm
Scanning range with objective 2 ²⁾	20 mm ± 2 mm
Scanning range with objective 3 ¹⁾	50 mm ± 5 mm
Light spot dimension with objective 1 ¹⁾	3.0 mm x 1.0 mm or round light spot D = 0.5 mm
Light spot dimension with objective 2 ²⁾	4.0 mm x 1.2 mm or round light spot D = 0.6 mm
Light spot dimension with objective 3 ¹⁾	10.0 mm x 2.0 mm or round light spot D = 1.0 mm
Light spot orientation	vertical or horizontal
Light source	LEDs (red, green, blue)

Timing

Switching frequency digital output	25 kHz/50 kHz reversible (see remarks)
Response time digital output	20 µs/10 µs reversible (see remarks)
Response jitter digital output	10 µs
Response time of analogue output	10 µs
Delay before start-up	≤ 250 ms

Electrical data

Operating voltage U_B ³⁾	12 ... 30 VDC (incl. residual ripple)
Residual ripple	≤ 15 % of U_B
Switching output	PNP, NPN
Function characteristics	light or dark switching, reversible via button
Analogue output	1 ... 10 mA
Signal voltage high/low	≥ ($U_B - 2V$) ≤ 2V
Output current	max. 100 mA
Open-circuit current	≤ 60 mA

Indicators

After power-on:	
ON LED on	device set to factory settings
ON LED flashing slowly	device not set to factory settings (display only for approx. 10 s after power-on)
After teach-in:	
ON LED on	switching threshold set to factory settings
ON LED flashing slowly	→ switching threshold in center
Q/T LED flashing quickly	switching threshold was reconfigured
In run mode:	
ON LED on	→ switching threshold close to the mark
Delay LED	switching error
L/D LED	
Q/T LED on	ready
Q/T LED flashing quickly	pulse stretching on/off
In configuration mode:	
ON LED flashing quickly	light/dark switching
Delay LED off	mark detected
Delay LED on	device error
L/D LED off	
L/D LED on	

Mechanical data

Housing	diecast zinc
Optics cover	glass
Weight	300 g
Connection type	M12 connector, stainless steel, 5-pin

Environmental data

Ambient temp. (operation/storage)	-25 °C ... +60 °C/-40 °C ... +70 °C
Protection class	IP 67
Light source	free group (in accordance with EN 62471)
VDE safety class	II
Protective circuit ⁴⁾	2, 3
Standards applied	IEC 60947-5-2
Certifications	UL 508, C22.2 No.14-13 ⁵⁾ 5)

Options

Synchronous input	
PNP: Stop/Start measurement	$U_B/0V$ or not connected
NPN: Stop/Start measurement	$0V/U_B$ or not connected
Synchronization delay	≤ 0.5 ms
Teach input	
PNP: active / not active	$U_B/0V$ or not connected
NPN: active/not active	$0V/U_B$ or not connected
Teach delay	≤ 10 ms
Pulse stretching	20 ms, can be activated via button
Device configuration	continue to press the teach button during power-on
Changeover switching threshold	see remarks
Changeover response time	see remarks

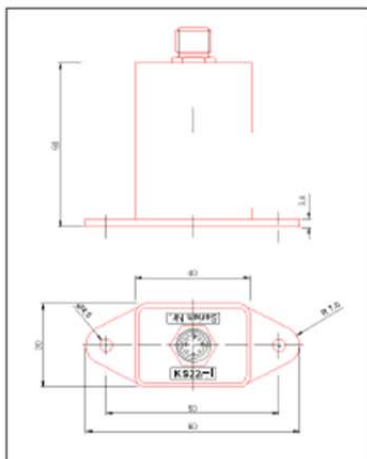
- 1) Interchangeable objective, available as accessory
 2) Standard objective, state on delivery
 3) For UL applications: for use in class 2 circuits according to NEC only
 4) 2-polarity reversal protection, 3-short-circuit protection for all outputs
 5) These proximity switches shall be used with UL Listed Cable assemblies rated 30V, 0.5A min, in the field installation, or equivalent (categories: CYN/CYV7 or PWA/PVA7)

Remarks

- **Approved purpose:**
This product may only be used by qualified personnel and must only be used for the approved purpose. This sensor is not a safety sensor and is not to be used for the protection of persons.
- With shiny objects, the sensor is to be mounted at an angle to the object surface.
- **Device configuration:**
 1. Configuration mode is activated by holding down the teach button during power-on (ON LED flashes).
 2. The analysis depth is changed over using the Delay button:
Delay LED off =
 2x analysis depth
 (response time 20 µs)
Delay LED on =
 1x analysis depth
 (response time 10 µs)
 3. The switching threshold is changed over using the L/D button:
L/D LED off =
 Switching threshold in center
L/D LED on =
 Switching threshold close to the mark
 4. Press the teach button to end device configuration.
 5. Back to factory settings: Simultaneously hold down the Delay button and the L/D button during power-on to reset the sensor to factory settings.

Acceleration sensor: DMT

Technische Daten		
Messachsen	2	y/z
Sensorkonstante	1,6	mA/(m/s ²)
Messbereich	± 5	m/s ²
Versorgungsspannung	20-30 (kurzz. 33)	Volt DC
Stromaufnahme	<80	mA
Frequenzbereich	0,01 ... 5	Hz
Dämpfung bei 10 Hz	>20	dB
Tschebyscheff Filter (4. Ordnung)	0,5	dB Welligk.
Analog Ausgang / Null-Lage	12 ± 0,05	mA
Ausgangsbereich	4 ... 20	mA
Einschwingzeit	30 ±	Sekunden
Gewicht (ohne Kabel)	282	Gramm
Anschluss Typ: Stecker SACC-E-M12MS-8CON-PG9/0,5	Axial 1554571	Phoenix
Temperaturbereich	-40° ... / +65°	Celsius
Schutzgrad	66	IP
Ausgangswiderstand	500	Ω
Maße	siehe Zeichnung	
Gehäusematerial	V2A Edelstahl	

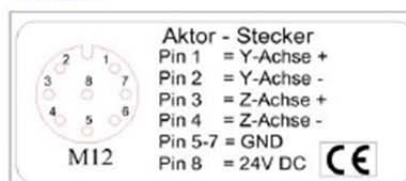


Maßbild: Änderungen, die dem Fortschritt und dem technischen Stand entsprechen, behalten wir uns vor.

Hinweise:

Eine mechanische Bearbeitung des Sensorgehäuses kann zu Fehlfunktionen führen und schließt die Gewährleistung aus.

Sensor nicht fallen lassen und vor groben Erschütterungen, statischen Aufladungen und Überspannung schützen.



DMT GmbH & Co. KG
Industrie Systeme

Am Technologiepark 1
45307 Essen

Telefon +49 201 172-1966
Telefax +49 201 172-1555

is@dmtd.de
www.dmt.de

TÜV NORD GROUP

DIN EN ISO 14001
zertifiziert

DIN EN ISO 9001
zertifiziert

© Copyright DMT | Alle Rechte vorbehalten | 05.2014

Current Grid: PEM Rogowski Coil

PERFORMANCE CHARACTERISTICS

Type	Sensitivity (mV/A)	Peak current (kA)	Peak di/dt (kA/μs)	Noise max ¹ (mV _{pk-pk})	Droop typ. (%/ms)	LF (3dB) bandwidth typ. (Hz) f_L	Phase lead at 50Hz typ. (deg)	HF (3dB) bandwidth typ. (MHz) f_H ²	
								Coil Length 300mm	Coil Length 700mm

High Sensitivity Ranges of CWT ... measuring currents from 300mA

CWT015	200.0	0.03	0.2	6.5	130	150	2.0 @ 6kHz	6	4
CWT03	100.0	0.06	0.4	4.5	90	105	2.0 @ 4kHz	10	6.5
CWT06	50.0	0.12	0.8	3.0	70	80	2.0 @ 3kHz	16	10
CWT1	20.0	0.3	2.0	2.5	40	50	1.9 @ 2kHz	16	10
CWT1N	20.0	0.3	2.0	2.0	20	25	1.9 @ 1kHz	10	5
CWT3	10.0	0.6	4.0	8.0	3.0	3.5	1.0 @ 300Hz	16	10

Standard Ranges of CWT ... measuring currents from 15A

CWT3N	10.0	0.6	4.0	14.0	0.9	1.0	1.7	10	5
CWT6	5.0	1.2	8.0	14.0	0.9	1.0	1.7	16	10
CWT15	2.0	3.0	20.0	7.0	0.7	0.8	1.3	16	10
CWT30	1.0	6.0	40.0	5.0	0.5	0.6	0.9	16	10
CWT60	0.5	12.0	40.0	3.5	0.35	0.4	0.6	16	10
CWT150	0.2	30.0	40.0	3.0	0.2	0.2	0.3	16	10
CWT300	0.1	60.0	40.0	3.0	0.1	0.1	0.2	16	10
CWT600	0.05	120.0	40.0	3.0	0.06	0.05	0.1	16	10
CWT1500	0.02	300.0	40.0	3.0	0.035	0.03	0.06	16	10

¹: Distributed around the f_L (-3dB) bandwidth.

²: For 2.5m cable length. Contact PEM for values of f_H for other coil and cable lengths

TYPICAL ACCURACY	Traceable calibration to $\pm 0.2\%$ with conductor central in the loop Variation with conductor position in the coil loop typically $\pm 1\%$	TYPICAL LINEARITY	$\pm 0.05\%$ (Full Scale)
-------------------------	---	--------------------------	---------------------------

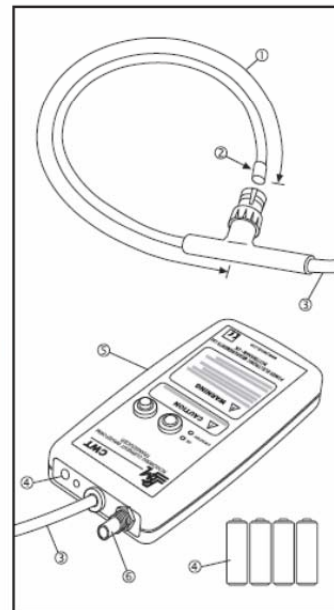
ABSOLUTE MAXIMUM VALUES OF di/dt (kA/μs) (value must not be exceeded)	CWT 03, 06 CWT 015, 1N, 3N all other CWT's	PEAK 40.0 PEAK 20.0 PEAK 40.0	RMS 1.2 @ 70°C RMS 1.0 @ 70°C RMS 1.5 @ 70°C	(Further information available on request)
--	--	--	---	--

COIL AND CABLE

① COIL CIRCUMFERENCE	300, 500, 700 or 1000mm
② COIL CROSS SECTION (max)	8.5mm - (14 mm with sleeve)
PEAK COIL VOLTAGE ISOLATION	10kV
Safe peak working voltage to earth. The coils are flash tested at 15kVrms for 60 seconds. The coil is supplied with a removable silicone sleeve which provides additional mechanical protection. Information about continuous use of the coils at high voltage can be obtained from PEM.	
TEMPERATURE RANGE	-20°C to 100°C
For de-rating due to temperature cycling please consult PEM	
③ CABLE LENGTH (from box to coil)	2.5m or 4m

INTEGRATOR

④ POWER SUPPLY	
B Battery 4 x AA (1.5V standard alkali batteries) -plus- 2.1/2.5mm socket for 12 to 24V ($\pm 10\%$) DC input	R Rechargeable battery 4 x AA (rechargeable NiMH batteries) -plus- 2.1/2.5mm socket for 12 to 24V ($\pm 10\%$) DC input
Typical life 70hrs Battery inoperative with DC supply present	Recharge time 40hrs, Typical life 30hrs Battery is charged whenever DC supply present
⑤ INTEGRATOR BOX DIMENSIONS	H = 183mm, W = 93mm, D = 32mm
⑥ OUTPUT SOCKET	BNC (output impedance 50Ω - unit supplied with 0.5m BNC - BNC coaxial cable)
MIN. OUTPUT LOADING	100kΩ (for rated accuracy)
TEMPERATURE RANGE	0°C to 40°C



ORDERING

Type + Power supply	/	Cable Length	/	Coil Circumference
CWT30 B	/	4	/	700

e.g. order code

If you have any queries regarding the CWT or require specifications outside our standard ranges please do not hesitate to contact us.

Current Generator: Chauvin – Arnoux Rogowski Coil

Flexible probe for AC current Model MA100 300-3000/3

MiniFLEX Series

■ Electrical specifications ⁽¹⁾

Operating voltage:
600 V_{RMS} (Cat. IV)
1,000 V_{RMS} (Cat. III)

Power supply:
9 V alkaline battery (NEDA 1604A, IEC 6LR61)

Battery life:
100 hours typical

Normal consumption:
3.6 mA typical

Battery level indication:
Green LED when > 7.0 V approx.

Influence of battery voltage:
≤ 0.1 % from 9 V to 7 V

Influence of temperature:
≤ 0.2 % / 10 K

Influence of humidity:
≤ 0.3 % from 10 % to 90 % Hr without condensation

Influence of conductor position in the sensor ⁽²⁾: ≤ 2.5 %

Influence of sensor deformation ⁽³⁾:
≤ 1.5 %

Influence of an adjacent conductor with circulating AC current ⁽⁴⁾:
≤ 1 % or 40 dB

Common mode rejection:
- between enclosure and secondary: ≤ 65 dB
- between sensor and secondary: ≤ 88 dB

Influence of the measurement instrument's impedance Z:
0.1% / Z (in MΩ)

■ Mechanical specifications

Clamping capacity:
Model de length 250: Ø max 70 mm
Model de length 350: Ø max 100 mm

Operating temperature:
-10 °C to +55 °C

Storage temperature:
-40 °C to +70 °C

Max. temperature of clamped conductor (measured):
≤ 90 °C

Relative humidity for operation:
0 to 85 % of RH with a linear decrease above 35 °C

Operating altitude:
0 to 2000 m

Storage altitude:
≤ 12,000 m

Leakproofing of enclosure:
- Casing: IP50
- Sensor: IP50
according to EN 60529/A1 Ed.06/2000

Protection against shocks:
IK04 according to NF EN 50102 Ed.1995

Self-extinguishing capability:
Casing: UL94-V2
Sensor: UL94 V0

Dimensions:
Casing: 140 x 64 x 28 mm
Connection cable length: 2 m
Ø of sensor: 5.5 mm approx.
Connection cable length: 3 mm approx.

Couleur:

Sensor: red
Sensor closing system: dark grey
Sensor locking tab: yellow
Casing: dark grey

Output:

Depending on model:
- 2 x Ø 4 mm safety plugs with 19 mm spacing or
- Coaxial cable 40 cm long, terminated by an insulated BNC plug

■ Safety specifications

Electrical safety:

Class II equipment with double or reinforced insulation between the primary and the secondary (winding connected to the connection cable) as per EN 61010-1 and 61010-2-032:
- 1,000 V Cat. III, pollution level 2
- 600 V Cat. IV, pollution level 2
- Type-B sensor
- 600 V Cat. III between the terminals or between the BNC output (depending on model) and the external enclosure of the casing

Electromagnetic compatibility (EMC):

Complies with the IEC 61326 (Ed.1997) + A1 (Ed.1998)
- Adequate immunity to disturbances for industrial environments
- Adequate immunity to disturbances for residential environments

(1) Reference conditions: 23 °C ± 5 °K, 20 to 75 % HR

Battery voltage : 9 V ± 0.5 V
Continuous external DC magnetic field (earth field) < 40 A/m
Absence of external AC magnetic field
External electrical field < 1 V/m
Position of conductor measured: centred in the measurement coil
Shape of measurement coil: quasi-circular
Measurement instrument input impedance (oscilloscope) ≥ 1 MΩ
Frequency and form of signal measured: 40 to 400 Hz sinusoidal.

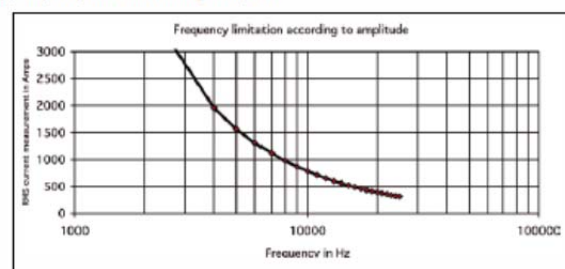
(2) Measurement range for the specifications indicated in this document.

(3) Any position, Ø of conductor measured ≥ 5 mm

(4) Adjacent conductor 1 cm from sensor, ≤ 2 % or 34 dB close to click-together system

(5) ≤ 6 % close to click-together system

(5) Frequency limitation according to amplitude



Current DC Link: LEM Hall Sensor



Current Transducer HTR 50 to 500-SB

For the electronic measurement of currents: DC, AC, pulsed..., with galvanic isolation between the primary circuit (high power) and the secondary circuit (electronic circuit).



$I_{PN} = 50 \dots 500 \text{ A}$



Electrical data

Type	Primary nominal current rms $I_{PN} \text{ (A)}$	Primary current, measuring range $I_{PM} \text{ (A)}$	
HTR 50-SB	50	± 100	
HTR 100-SB	100	± 200	
HTR 200-SB	200	± 400	
HTR 300-SB	300	± 600	
HTR 400-SB	400	± 800	
HTR 500-SB	500	± 1000	
V_{OUT} Output voltage (Analog)		± 4	V
R_L Load resistance		> 10	k Ω
V_C Supply voltage ($\pm 5\%$)		$\pm 12 \dots 15$	V
I_C Current consumption (max)		20	mA

Accuracy - Dynamic performance data

X	Accuracy ¹⁾ @ I_{PN} , $T_A = 25^\circ\text{C}$, @ $\pm 12 \dots 15 \text{ V}$ ($\pm 5\%$)	$\leq \pm 2$	%
ε_L	Linearity error ¹⁾	$\leq \pm 1$	%
V_{OE}	Electrical offset voltage @ $I_p = 0$, $T_A = 25^\circ\text{C}$	Typ ± 45 Max ± 65	mV
V_{OM}	Magnetic offset voltage @ $I_p = 0$ and specified R_M , after an overload of $3 \times I_{PN}$	± 10 ± 20	mV
V_{OT}	Temperature variation of V_O - $10^\circ\text{C} \dots +70^\circ\text{C}$	± 70 ± 240	mV
$TC\varepsilon_G$	Thermal drift of the gain, $T_A = -10 \dots +70^\circ\text{C}$	± 140 ± 450	mV
t_r	Response time to 90 % of I_{PN} step	< 10	μs
di/dt	di/dt accurately followed	> 50	A/ μs
BW	Frequency bandwidth (-1 dB)	DC ... 10	kHz

General data

T_A	Ambient operating temperature	$-10 \dots +70$	$^\circ\text{C}$
T_S	Ambient storage temperature	$-20 \dots +85$	$^\circ\text{C}$
m	Mass	80	g
	Standard	EN 50178	

Note: ¹⁾ Excludes the electrical offset.

Features

- Open loop Hall effect transducer
- Busbar mounting or panel mounting.
- Isolated plastic case recognized according to UL 94-V0.

Advantages

- Low power consumption
- Split core easy for mounting
- High isolation between the primary and the secondary circuit
- Through-hole, no insertion losses.

Applications

- Power supplies for TELECOM (monitoring & measuring)
- Uninterruptible Power Supplies (UPS)
- Switched Mode Power Supplies (SMPS)
- Electrical chemistry
- Chooper
- Battery supplied applications.

Application domain

- Industrial.

Laser distance sensor for blade dynamics: micro – epsilon optoNCDT 1191

Model		ILR1191-300
Measuring range ¹⁾	black 6%	1 ... 150m
	grey 10%	0.5 ... 200m
	white 90%	0.5 ... 300m
	reflector	300 ... 3000m
Speed		0ms ⁻¹ ... 100ms ⁻¹
Linearity ²⁾		±20mm (at measurement output 100Hz) ±60mm (at measurement output 2kHz)
Resolution		1mm
Repeatability		≤20mm
Response time	distance measurement	0.5ms
	speed measurement	12ms
Laser class	measuring laser	905nm, laser class 1
	sighting laser	635nm, laser class 2
Operation temperature		-40°C ... +60°C
Storage temperature		-40°C ... +70°C
Limit outputs		QA/QB (max. 200mA)
Switching points		free adjustable
Switching hysteresis		free adjustable
Trigger input		trigger edge and trigger delay programmable, trigger pulse max. 30V
Serial interface		RS232 and RS422 with 1.2kBaud ... 460.8kBaud SSI interface (RS422), 24Bit, Gray-encoded 50kHz ... 1MHz
Profibus		RS485, 9.6 kBaud ... 12MBaud
Operation mode		single/continuous measurement, external triggering (adjustable near field elimination), speed measurement
Analogue output		4 ... 20mA (16 Bit DA)
Temperature stability		≤50ppm/°C
Supply		10 ... 30 V DC
Max. consumption		<5W without heating, 11.5W with heating
Connection		1 x 12-pin M16, 2 x 5-pin M12 B-coded
Protection class		IP 67
Material (housing)		aluminium strangeness profile, powder-coated
Weight		800g (depends on equipment)
Vibration/Shock		500g, 0.5ms, 1 shock/axis (DIN ISO 9022-30-08-1)
		10g, 6ms, 1000 shocks/axis (DIN ISO 9022-3-31-01-1)
EMV		EN 61000-6-2, EN 55011

GoPro Hero 3 Black edition

HERO3 BLACK EDITION

PROFESSIONAL VIDEO

RESOLUTION	FPS	VIEW ANGLE
4Kp	12	Ultra Wide
2.7Kp	30, 25, 24	Ultra Wide
1440p	48, 30, 25, 24	Ultra Wide
1080p	60, 50, 48, 30, 25, 24	Ultra Wide, Med, Narrow
960p	100, 48	Ultra Wide
720p	120, 100, 60, 50	Ultra Wide, Med*, Narrow*
WVGA	240	Ultra Wide

*720p/240 does not support medium view angle. Medium and narrow may require a software update. Visit gopro.com/update

INCLUDES:

protune.

Protune is a video mode that enables cinema-quality video for professional productions.

PHOTOS

<p>PHOTO 12, 7, 5MP</p>	<p>CONTINUOUS PHOTO 3/sec, 5/sec, 10/sec</p>	<p>BURST 12MP @ 30 fps</p>	<p>TIME-LAPSE 0.5, 1, 2, 5, 10, 30, 60 second intervals</p>	<p>SIMULTANEOUS VIDEO + PHOTO 1080p24/1080p30/720p60/1440p24</p>
------------------------------------	---	---------------------------------------	--	---

WI-FI BUILT IN

WI-FI REMOTE (INCLUDED)
Control up to 50 cameras at a time.

GOPRO APP COMPATIBLE (FREE)
Use your smartphone or tablet as a live video remote control.

Wi-Fi remote sold separately. For a list of GoPro App compatible smartphones and tablets, visit gopro.com.

CAMERA SPECIFICATIONS

OPTICS

- Ultra sharp f/2.8 6-element aspherical glass lens
- Ultra wide angle / reduced distortion
- 2X Better low-light performance*

VIDEO (NTSC/PAL)

- See info above for resolutions and frame rates
- Video format: H.264 codec, .mp4 file format
- White Balance: auto and manual

PHOTO MODES

- 12, 7, 5MP resolutions
- Burst: 30 photos per second
- Time-lapse: 0.5, 1, 2, 5, 10, 30, 60 second intervals
- Continuous photo: 3, 5, 10 photos/sec

BATTERY & CHARGING

- 1050mAh rechargeable lithium-ion
- Charge via USB

AUDIO

- Mono, AAC compression w/ AGC
- Supports optional 3.5mm stereo mic adapter**

STORAGE

Memory:

- MicroSD (Class 10 or higher required)
- Up to 64 GB capacity required
- Record times will vary with resolution and frame rates

INCLUDED CABLES

- USB charging cable
- Remote charging cable

OPTIONAL CABLES + ADAPTERS**

- Micro HDMI cable
- Composite A/V cable
- 3.5mm stereo mic adapter

OPERATING SYSTEM

- Microsoft Windows® Vista, 7 and later
- Mac OS® X 10.5 and later

*Compared to HD Hero2 and HERO3 White and Silver Edition cameras.
**Optional accessories sold separately.

Appendix B

